



**PIEZOELECTRIC RESPONSE OF FERROELECTRIC CERAMICS  
UNDER MECHANICAL STRESS**

DISSERTATION

Sergey M. Kaplan, Major, USAF

AFIT-ENY-DS-15-S-064

**DEPARTMENT OF THE AIR FORCE  
AIR UNIVERSITY**

***AIR FORCE INSTITUTE OF TECHNOLOGY***

---

**Wright-Patterson Air Force Base, Ohio**

Distribution Statement A:  
Approved for Public Release; Distribution Unlimited

The views expressed in this dissertation are those of the author and do not reflect the official policy or position of the United States Air Force, the Department of Defense, or the United States Government.

This material is declared a work of the U.S. Government and is not subject to copyright protection in the United States.

AFIT-ENY-DS-15-S-064

PIEZOELECTRIC RESPONSE OF FERROELECTRIC CERAMICS  
UNDER MECHANICAL STRESS

DISSERTATION

Presented to the Faculty  
Graduate School of Engineering and Management  
Air Force Institute of Technology  
Air University  
Air Education and Training Command  
in Partial Fulfillment of the Requirements for the  
Degree of Doctor of Philosophy in Aeronautical Engineering

Sergey M. Kaplan, M.S.A.E.  
Major, USAF

September 2015

Distribution Statement A:  
Approved for Public Release; Distribution Unlimited

PIEZOELECTRIC RESPONSE OF FERROELECTRIC CERAMICS  
UNDER MECHANICAL STRESS

Sergey M. Kaplan, M.S.A.E.  
Major, USAF

Committee Membership:

Robert B. Greendyke, Ph.D.  
Chair

William F. Bailey, Ph.D.  
Member

Maj Darrell S. Crowe, Ph.D.  
Member

Lt Col Richard E. Huffman Jr., Ph.D.  
Member

Jason R. Foley, Ph.D.  
Member

ADEDEJI B. BADIRU, Ph.D.  
Dean, Graduate School of Engineering  
and Management

**Abstract**

Manufacturers are constantly developing increasingly miniature, ferroelectric multi-layer ceramic capacitors, survivable under progressively harsher mechanical stresses. However, the piezoelectric response of the bulk Barium Titanate-based dielectric in such capacitors has not yet been addressed for shocks above 3,000 g. Thus, the current research developed a finite element capacitor model and modified an established constitutive relationship to calculate the capacitive response under high-g drop impact. Scanning electron microscope and impedance analyzer data confirmed the flexural mode of mechanical failure, while the newly applied Resistor Capacitor (RC) capacitance measurement technique detected discreet partial and complete electrode separation from the terminal, corresponding to the board oscillation frequency. The experiments detected an up to 10% increase in capacitance during 24,000 g shocks, while the numerical model predicted the electromechanical response to within 2% of the nominal capacitance value, closely matching in waveform to the experimental data. When the flexural failures were completely prevented and the capacitance response was reduced by 81% with completely restricted board flexure, the electromechanical response was still detectable during drop impacts generating 3,000 g peak accelerations. While preventing board oscillations may reduce mechanical failure probability, unaddressed piezoelectric response of ferroelectric capacitors may still cause significant intermittent reliability issues above commercially relevant conditions.

## **Acknowledgments**

This work and research would not have been possible without the contributions and support of numerous people spanning three different government organizations. First, I would like to thank my committee members for their immense support, including Dr Robert B. Greendyke, for his whole-hearted dedication and guidance as my advisor, teacher and mentor, Dr William F. Bailey, Dr Darrell S. Crowe and Dr Richard E. Huffman Jr., for their invaluable advice and direction during my studies, and of course Dr Jason R. Foley, for his help in defining and financing this important research topic. Many thanks go out to Dr Brook I. Bentley for his role in shaping the problem statement after the Prospectus defense. I would also like to thank Dr Ryan D. Lowe, Dr Alain L. Beliveau, Chris “Roy” Kimbrough, Jonathan Hong and Curtis McKinion for their amazing assistance during the board manufacturing process and drop tower experiments, as well as Dr Michael K. Wong, Susan K. Carroll and Duane A. Labreche for their unwavering and awesome technical support with implementing the ALEGRA-EMMA models. I am also grateful for the tremendous time and support of James C. Hierholzer for building the custom test fixture, Michael D. Craft for his help with static capacitance measurements, Bryan J. Turner, Scott D. Apt and Scott J. Robertson for their help in operating the scanning electron microscope, as well as David R. Doak, Donald E. Bodle, Stephen W. Klein and Wilber R. Lacey for helping me set up all the necessary computational capabilities at school. Finally, I would also like to thank my mom, dad and sister for their continuous encouragement during my research, and of course, my wife for her incredible support at home during all the late nights when I was studying.

Sergey M. Kaplan

## Table of Contents

|   | Page |
|---|------|
| Abstract . . . . .  | iv   |
| Acknowledgments . . . . .   | v    |
| Table of Contents . . . . .   | vi   |
| List of Figures . . . . .   | viii |
| List of Tables . . . . .  | xii  |
| List of Symbols . . . . .   | xiii |
| List of Acronyms . . . . .  | xvi  |
| I. Introduction . . . . .   | 1    |
| II. Literature Review . . . . .   | 8    |
| 2.1 Capacitors . . . . .  | 8    |
| 2.1.1 Capacitor Structure and Performance Factors . . . . .                         | 9    |
| 2.1.2 Dielectric Materials . . . . .  | 14   |
| 2.2 Theoretical and Mathematical Backgrounds . . . . .                              | 22   |
| 2.3 Ferroelectric Material Theory and Polarization Characterization Tools . . . . . | 29   |
| 2.4 Recent Work On Component Reliability . . . . .                                  | 38   |
| 2.5 Early Development of Computational Capabilities . . . . .                       | 44   |
| 2.6 Piezoelectric Model in ALEGRA-EMMA . . . . .                                    | 48   |
| 2.7 Purpose of the Present Research . . . . .                                       | 54   |
| III. Methodology . . . . .  | 57   |
| 3.1 Experimental Set-Up for Measuring PCB Dynamic Response . . . . .                | 58   |
| 3.2 Experimental Set-Up for Measuring Capacitance Response to Drop Impact . . . . . | 60   |
| 3.2.1 High Voltage Capacitance Measurements . . . . .                               | 60   |
| 3.2.2 Low Voltage Capacitance Measurements . . . . .                                | 68   |
| 3.2.3 Static Capacitance Measurements of Shocked Devices . . . . .                  | 71   |
| 3.3 Material Characterization Using the Scanning Electron Microscope . . . . .      | 73   |
| 3.4 Computational Model of Printed Circuit Boards (PCB) Dynamic Response . . . . .  | 75   |
| 3.5 Computational Model of Capacitor Electromechanical Response . . . . .           | 79   |

|   | Page |
|---|------|
| 3.5.1 Capacitor Sub-model Development . . . . .   | 80   |
| 3.5.2 Computational RC Circuit Implementation . . . . .   | 84   |
| 3.5.3 Input Parameters and Data Processing . . . . .  | 85   |
| 3.6 Uncertainty Analysis . . . . .  | 90   |
| IV. Results and Analysis . . . . .  | 93   |
| 4.1 Phase I: PCB Dynamics Under High-g Drop Impact Stress . . . . .                                 | 95   |
| 4.1.1 Drop Tower Characterization and Data Processing Effects . . . . .                             | 95   |
| 4.1.2 Computational PCB Model Performance . . . . .   | 100  |
| 4.2 Phase II: Capacitance Response and Scanning Electron Microscope (SEM)<br>Measurements . . . . . | 112  |
| 4.2.1 Mechanical Mode of Failure . . . . .  | 112  |
| 4.2.2 Experimentally Measured Electromechanical Response . . . . .                                  | 120  |
| 4.3 Phase III: Computational Electromechanical Response Model . . . . .                             | 130  |
| 4.3.1 Non-flexing Board Capacitor Response . . . . .  | 132  |
| 4.3.2 Flexing Board Capacitor Response . . . . .  | 141  |
| V. Conclusions . . . . .  | 149  |
| Bibliography . . . . .  | 157  |



## List of Figures

| Figure  | Page |
|---|------|
| 2.1 Parallel-Plate Capacitor Electrode Structure . . . . .                | 12   |
| 2.2 Series/Floating Electrode Capacitor Structure . . . . .               | 12   |
| 2.3 Dielectric Polarization . . . . .                                     | 17   |
| 2.4 Paraelectric Polarization . . . . .                                   | 17   |
| 2.5 Ferroelectric Polarization . . . . .                                  | 17   |
| 2.6 Single Crystal Hysteresis . . . . .                                   | 19   |
| 2.7 Multiple Domain Hysteresis . . . . .                                  | 19   |
| 2.8 Continuous Body Trajectory Using Euler's Notation . . . . .           | 24   |
| 2.9 Paraelectric $\mathcal{F}$ w/o Hysteresis . . . . .                   | 32   |
| 2.10 Ferroelectric $\mathcal{F}$ w/ Hysteresis . . . . .                  | 32   |
| 2.11 Paraelectric $\mathcal{F}$ w/o Hysteresis . . . . .                  | 33   |
| 2.12 Ferroelectric $\mathcal{F}$ w/ Hysteresis . . . . .                  | 33   |
| 2.13 Dynamic Responses During 22 <sup>nd</sup> drop. ©2006 IEEE . . . . . | 40   |
| 2.14 Solder Joint Failure Process. ©2006 IEEE . . . . .                   | 41   |
| 3.1 10 ft MTS Drop Tower . . . . .  | 58   |
| 3.2 ISOLA 370HR Board Specimen Test Set-Up . . . . .                      | 59   |
| 3.3 Printed Circuit Board Electrical Layout . . . . .                     | 61   |
| 3.4 Exmore VS-5000 Vapor Soldering Re-flow Oven . . . . .                 | 62   |
| 3.5 SP5500 Dual Squeegee Stencil Pencil . . . . .                         | 63   |
| 3.6 Data Acquisition Schematic . . . . .                                  | 64   |
| 3.7 Flexing Board Configuration A1 w/ Caul Clamps . . . . .               | 66   |
| 3.8 Flexing Board Configuration A2 w/ Steel Clamps . . . . .              | 66   |
| 3.9 Non-flexing Board Configuration B . . . . .                           | 69   |

| Figure   | Page |
|--|------|
| 3.10 Static Capacitance and Dissipation Factor Measurement Set-up . . . . .  | 72   |
| 3.11 Test Articles Assembled in a Single Puck and Prepared for SEM Imaging . . . .   | 74   |
| 3.12 FEI Quanta 600F Scanning Electron Microscope . . . . .  | 74   |
| 3.13 1/4 Symmetry Computational Model for Dynamic PCB Response Validation . .  | 75   |
| 3.14 SEM Image of the 10 Volts Direct Current (VDC) XZ-Plane Cut Surface and<br>Electrode Layout Schematic (not to scale) . . . . .                                | 80   |
| 3.15 Low Voltage Capacitor Dielectric Volume Sections . . . . .  | 81   |
| 3.16 Electrodes, Terminals and Boundary Condition Surfaces . . . . .   | 82   |
| 3.17 Coarse Mesh . . . . .   | 83   |
| 3.18 Fine Mesh . . . . .   | 83   |
| 3.19 RC Circuit Model in Arbitrary Lagrangian-Eulerian Multi-Material, Multi-<br>Physics and Electromechanics (ALEGRA-EMMA) . . . . .                              | 85   |
| 3.20 Layout of Tracers in the Capacitor . . . . .  | 89   |
| 3.21 Methodology Flow Chart (solid boxes are experimentally obtained data,<br>dashed boxes are computational models and ovals are research goals) . . . . .        | 92   |
| 4.1 Filtering Effects on Accelerometer Data . . . . .  | 96   |
| 4.2 Filtering Effects on Strain Gage Data . . . . .  | 97   |
| 4.3 Impacted Programmer Effects During High Voltage Capacitor Tests . . . . .  | 98   |
| 4.4 Impacted Programmer Effects During Low Voltage Capacitor Tests . . . . .   | 99   |
| 4.5 Acceleration Profiles Used for Dynamic PCB Response Study . . . . .  | 101  |
| 4.6 Surface vs. Body Driven Acceleration FFT; $E = 21.9115 \text{ GPa}$ , $\rho = 1800 \text{ kg/m}^3$ ,<br>Frictionless Contact Type . . . . .                    | 102  |
| 4.7 Surface-Driven vs. Body-Driven Acceleration Strain Responses; $E = 21.9115 \text{ GPa}$ ,<br>$\rho = 1904 \text{ kg/m}^3$ , Contact Type $\mu = 0.5$ . . . . . | 103  |

| Figure  | Page |
|---|------|
| 4.8 Effect of Young's Modulus on Strain Response; $\rho = 1,800 \text{ kg/m}^3$ , Tied Contact Type, Body-Driven BC . . . . .   | 104  |
| 4.9 Effect of Density on Strain Response; $E = 17.0000 \text{ GPa}$ , Tied Contact Type, Body-Driven BC . . . . .   | 105  |
| 4.10 Linear Strain Dominant Frequency Sensitivity to Young's Modulus and Density  | 105  |
| 4.11 Linear Peak Strain Amplitude Sensitivity to Young's Modulus and Density . . .  | 106  |
| 4.12 Tied vs. Frictionless Contact; $E = 21.9115 \text{ GPa}$ , $\rho = 1,904 \text{ kg/m}^3$ , Body-Driven BC . . . . .  | 107  |
| 4.13 Strain Response to Half-Sine Acceleration Profile; $E = 17.0000 \text{ GPa}$ , $\rho = 2,090 \text{ kg/m}^3$ , Tied Contact, Body-Driven BC . . . . .  | 109  |
| 4.14 Close-up of Strain Response to Half-Sine Acceleration Profile; $E = 17.0000 \text{ GPa}$ , $\rho = 2,090 \text{ kg/m}^3$ , Tied Contact, Body-Driven BC . . . . .                                | 110  |
| 4.15 Half-sine Acceleration Profile Strain Response FFT; $E = 17.0000 \text{ GPa}$ , $\rho = 2090 \text{ kg/m}^3$ , Tied Contact, Body-Driven BC . . . . .  | 110  |
| 4.16 1210-size Capacitor Flexural Mode of Failure . . . . .   | 113  |
| 4.17 1812-size Capacitor Flexural Modes of Failure . . . . .  | 114  |
| 4.18 1812-size Capacitor Discrete Capacitance Oscillations due to Flexural Mode of Failure Correlating in Frequency to Board Strain Oscillations . . . . .  | 116  |
| 4.19 Fracture Propagation due to Flexural Stresses Resulting in Partial Separation of Electrodes From the Terminal . . . . .  | 117  |
| 4.20 Capacitance Increase due to Recontact with Electrodes, Intermittent Contact of Capacitor with the Pad and Final Separation from the Flexing Board of 1812 Capacitor after 36-inch Drop . . . . . | 118  |
| 4.21 Dielectric Fracture Propagation Due to Flexural Stresses Resulting in Complete Flexural Mechanical Failure . . . . .   | 119  |

| Figure   | Page |
|--|------|
| 4.22 Discrete Changes in Capacitance of Mechanically Failed Devices Measured<br>Using Impedance Analyzer at 100 KHz . . . . .  | 120  |
| 4.23 Capacitance Increase due to Electromechanical Response and Intermittent<br>Contact of Electrodes with the Terminal of Flexing Board 1210 Capacitor After<br>36-inch Drop . . . . .      | 121  |
| 4.24 SEM Analysis of the Dielectric Material . . . . .   | 123  |
| 4.25 Electromechanical Response of Capacitors Mounted on the Flexing Boards . .  | 125  |
| 4.26 Electromechanical Response of Capacitors Mounted on the Non-Flexing Boards  | 126  |
| 4.27 Electromechanical Response of 72-inch vs. 30-inch Height Drop Capacitors<br>Mounted on the Non-Flexing Board . . . . .  | 128  |
| 4.28 Effect of Processed Acceleration Profile as Boundary Condition on Compu-<br>tationally Obtained Permittivity and Capacitance Values for a 72-inch, Non-<br>flexing Board Drop . . . . . | 135  |
| 4.29 Capacitance Response Based on Direct Calculation of the Permittivity<br>Results in 3 Order of Magnitude Difference Between Experimental Data and<br>Computational Predictions . . . . . | 136  |
| 4.30 Experimental vs. Computational Capacitance Response for All 8 Non-flexing<br>Board Drops . . . . .  | 138  |
| 4.31 Experimental vs. Computational Capacitance Waveform Comparison . . . . .  | 139  |
| 4.32 Effect of Reducing Elastic Modulus Constants and Refining the Mesh;<br>60–inch, 18,487 g Impact . . . . .   | 140  |
| 4.33 Experimental vs. Computational Capacitance Response for All 3 Flexing<br>Board Drops . . . . .  | 143  |
| 4.34 Approximation of Mechanical Failure Probability and Electromechanical<br>Response of Flexing and Non-flexing Boards . . . . .   | 147  |

## List of Tables

| Table   | Page |
|---|------|
| 3.1 High Voltage Capacitance Test Matrix (X indicates data collected) . . . . .   | 66   |
| 3.2 Low Voltage Capacitance Test Matrix (X indicates data collected) . . . . .  | 70   |
| 3.3 Dynamic PCB Model Computational Parameter Matrix . . . . .  | 77   |
| 3.4 The Multilayer Ceramic Capacitors (MLCC) Mesh Parameters . . . . .  | 84   |
| 3.5 Elastic, Piezoelectric and Permittivity Moduli Constants [11] . . . . .   | 87   |
| 4.1 Effects of Impacted Programmer on Acceleration Profile Over 50 Runs . . . . .   | 100  |
| 4.2 Computational Run Matrix to Calculate Electromechanical Response of Low<br>Voltage Capacitors (“Drop #” Below Corresponds to Experimental “Test #” in<br>Table 3.2) . . . . . | 131  |

## List of Symbols

Symbol    Definition

$C$             Capacitance (Farad)

$d$             Distance (Meter)

$Q, q$         Charge (Coulomb)

$\mathbf{E}, E$         Electric field (Volt / Meter)

$A, S$         Area (Meter<sup>2</sup>)

$V, \phi$         Electric potential (Volt)

$\epsilon$             Permittivity (Farad / Meter)

$\kappa$             Dielectric constant or relative permittivity

$U, E$         Energy (Coulomb Volt), (Joule)

$u_e$         Energy per unit volume (Coulomb Volt / Meter<sup>3</sup>)

$\sigma$             Bound charge density (Coulomb / Meter<sup>3</sup>) or Stress (Pascal)

$T_c$         Curie temperature (Degrees Kelvin)

$\rho$             Density (Kilograms / Meter<sup>3</sup>)

$\dot{\mathbf{x}}$         Material trajectory velocity (Meters / Second)

$\mathbf{X}$         Material position (Meter)

$t$             Time (seconds) or Thickness (Meter)

$F_{ij}$         Deformation gradient tensor

$\mathbf{G}$         Momentum (Kilogram Meter / Second)

$\mathbf{F}$         Force (Newton)

$\mathbf{L}_O$         Angular momentum (Newton Meter Second)

$\mathbf{M}_O$         Torque (Newton Meter)

$\mathbf{t}$         Surface force per unit area (Newton / Meter<sup>2</sup>)

$\mathbf{b}$         Body force per unit mass (Newton / Kilogram)

| Symbol           | Definition  |
|------------------|---|
| $T_{ij}$         | Three dimensional stress tensor (Pascal)                                  |
| $\mathbf{n}$     | Vector normal to surface  |
| $\mathbf{g}$     | Momentum per unit mass (Kilogram Meter / Second)                          |
| $\varepsilon$    | Energy per unit mass (Joule / Kilogram)                                   |
| $Q$              | Heating (Joule)   |
| $\beta$          | Contact heating per unit area (Joule / Meter <sup>2</sup> )               |
| $h$              | Body heating per unit mass (Joule / Kilogram), Element size (Meter)       |
| $\Pi$            | Forces acting on the body (Newton)  |
| $\mathbf{q}$     | Heat flux (Joules / Second)   |
| $\mathcal{E}$    | Electromotive intensity (Coulomb Volt)                                    |
| $\mathbf{B}$     | Magnetic field (Tesla)  |
| $\mathbf{H}$     | Current potential (Ampere / Meter)  |
| $\mathbf{D}$     | Charge potential or electric displacement (Coulomb / Meter <sup>2</sup> ) |
| $T$              | Temperature (Kelvin)  |
| $\mathcal{H}$    | Magnetomotive intensity (Ampere / Meter <sup>2</sup> )                    |
| $\mu$            | Permeability (Newton / Meter <sup>2</sup> )                               |
| $I$              | Current (Ampere)  |
| $\mathbf{P}, P$  | Polarization (Coulomb / Meter <sup>2</sup> )                              |
| $\mathbf{M}$     | Magnetization (Ampere / Meter)  |
| $\mathcal{M}$    | Lorentz magnetization (Ampere / Meter)                                    |
| $\mathcal{F}, G$ | Free energy (Joules)  |
| $\eta, S$        | Strain  |
| $K, E$           | Young's Modulus (Pascal)  |
| $k_B$            | Boltzmann constant (Joule / Kelvin)                                       |
| $\xi$            | Correlation length (Meter)  |

| Symbol          | Definition  |
|-----------------|---|
| $g(\vec{r})$    | Polarization correlation function (Coulomb / Meter <sup>2</sup> ) |
| $R$             | resistance (Ohms)   |
| $u_i$           | spacial displacement (Meter)                                      |
| $C_{ijkl}$      | Elastic moduli constants (Pascal)                                 |
| $e_{ijk}$       | Piezoelectric constants (Coulomb / Meter <sup>2</sup> )           |
| $\epsilon_{ij}$ | Dielectric constants (Farad / Meter)                              |
| $\theta$        | Angle (Degree)  |
| $K_{bulk}$      | Bulk modulus (Pascal)   |
| $\nu$           | Poisson's ratio   |
| $C_s$           | Speed of sound (Meter / Second)                                   |
| $C_v$           | Constant volume heat capacity (Joule / Kelvin)                    |

### *Subscripts*

|     |                               |
|-----|-------------------------------|
| $b$ | Bound                         |
| $f$ | Free                          |
| $0$ | Nominal, Initial or in Vacuum |

### *Superscripts*

|      |                                   |
|------|-----------------------------------|
| $b$  | Body reference frame              |
| $n$  | Navigation reference frame        |
| $g$  | Material reference frame          |
| $G$  | Global reference frame            |
| $gG$ | Material to global transformation |
| $Gg$ | Global to material transformation |



## **List of Acronyms**

| Acronym     | Definition   |
|-------------|--|
| AFRL        | Air Force Research Laboratory  |
| AFIT        | Air Force Institute of Technology  |
| JEDEC       | Joint Electron Device Engineering Council  |
| FEA         | Finite Element Analysis  |
| COTS        | Commercial Off-The-Shelf   |
| PCB         | Printed Circuit Boards   |
| XFEM        | Extended Finite Element Method   |
| BGA         | Ball Grid Array  |
| CZM         | Cohesive Zone Model  |
| SEM         | Scan Electron Microscope   |
| PZT         | Lead Zirconate Titanate  |
| FEG         | Ferroelectric Generator  |
| QSE         | Quasi-Static Electric  |
| ALEGRA-EMMA | Arbitrary Lagrangian-Eulerian Multi-Material, Multi-Physics and Electromechanics |
| ALE         | Arbitrary Lagrangian-Eulerian  |
| SNL         | Sandia National Laboratories   |
| AC          | Alternating Current  |
| DC          | Direct Current   |
| MLCC        | Multilayer Ceramic Capacitors  |
| LD          | Landau - Devonshire  |
| LG          | Landau - Ginzburg  |
| SPM         | Scanning Probe Microscopy  |

| Acronym | Definition  |
|---------|---|
| SFM     | Scanning Force Microscope                         |
| TEM     | Transmission Electron Microscopy                  |
| FE-AFE  | Ferroelectric-Anti-Ferroelectric                  |
| PMMA    | Polymethyl Methacrylate                           |
| FFT     | Fast Fourier Transforms                           |
| HPC     | High Performance Computer                         |
| IEEE    | Institute of Electrical and Electronics Engineers |
| VDC     | Volts Direct Current                              |
| RC      | Resistor Capacitor                                |
| SEM     | Scanning Electron Microscope                      |
| EDS     | Energy Dispersive Spectroscopy                    |
| CPU     | Central Processing Unit                           |
| AFB     | Air Force Base                                    |
| MCF     | Materials Characterization Facility               |

# PIEZOELECTRIC RESPONSE OF FERROELECTRIC CERAMICS UNDER MECHANICAL STRESS

## I. Introduction

Aerospace technology designers and manufacturers have always had to maintain a perfect balance between safety, performance and efficiency. Money and effort that went into expensive testing of a limited number of articles and components dedicated to investigating their performance had to be weighed against the company profit margins and component reliability. Thus, commercial and military aircraft, and their associated aircraft support systems manufacturing industry had to focus on understanding the reliability of their products only in operationally representative environments. In particular, electronic packages integrated inside aerospace equipment were tested under only the expected vibration profiles, mechanical loadings and thermal operating conditions. Consequently, reliability testing of electronic packages was concentrated over a very specific range of operating conditions and the failure modes of the aerospace electronics were investigated only in these environments.

Due to the prohibitive cost of developing new technology intended for an extremely narrow range of applications, a significant amount of military hardware is derived from Commercial Off-The-Shelf (COTS) electronics. Unfortunately, while a vast majority of electronics used in military applications share similar operating conditions throughout their exploitation as electronic packages developed from the same COTS products and used for similar purposes in the civilian arena, some military technology is subjected to much harsher mechanical loadings. Therefore, this study will focus on developing relationships between mechanical stress and failure mechanisms of surface mounted

electronics, which can predict electronics material and component performance, and reliability under mechanical stresses representative of military applications.

Printed Circuit Boards (PCB) used in munitions for fuzing or detonation initiation are subjected to a much wider range of temperatures before employment, and are expected to reliably perform under much higher shock impact loadings than even those specified in the Joint Electron Device Engineering Council (JEDEC) standards, which are used by the industry and academia to test the reliability of electronics. For example, circuitry inside munitions must be able to withstand hours of cold soaking at temperatures on the order of  $-50^{\circ}\text{C}$ , and then within minutes, or even seconds, be able to perform under mechanical shocks and approximately 20,000 g acceleration profiles, which are an order of magnitude greater than those specified by the JEDEC standards [1–3]. Even though electronic components might have been developed and tested with a certain amount of an engineering safety factor, extrapolating equipment performance past the range of conditions under which the expensive testing has been performed in order to reduce cost of development is an extremely dangerous practice. Furthermore, failure mechanisms of electronics are still poorly understood, and must be sufficiently investigated before attempting to predict electrical component behavior under harsh environmental conditions. Thus, if the extreme mechanical stresses indicative of the environment in military applications can be correlated to certain failure mechanisms of electronics materials, it might be possible to establish elementary component design rules in order to increase reliability of aerospace systems.

While discussing reliability of any electronic package, which is sometimes anecdotally called a study of poor contacts, two overarching modes of failure must be addressed, mechanical and electromechanical. Mechanical breakdown of electrical circuits is essentially a study of material properties of components manufactured under varying conditions when subjected to a wide range of mechanical loadings, impact shocks or thermal stresses on different temporal scales. In order to better understand the

behavior of each class of materials such as polymers, solder alloys, ceramics and metals that make up the electrical circuitry, different constitutive relationship models such as the Zerilli-Armstrong, Mulliken-Boyce, Johnson-Cook, Anand, Steinberg-Guinan-Lund, MieGruneisen and more have been developed based on empirical observations [4–8]. Often, mechanical breakdown occurs near the material interface, and this phenomenon has recently also attracted much attention from both experimental and computational communities. Relatively new computational methods, such as Cohesive Zone Model (CZM) and Extended Finite Element Method (XFEM) have been further developed by academia, and implemented in many commercial Finite Element Analysis (FEA) codes in order to better predict mechanical breakdown of materials at their interface [9, 10]. Furthermore, in order to simulate mechanical shock effects, explore the dynamic response, and predict mechanical breakdown of electronic materials, numerous testing techniques such as very high-g machines, drop towers, Hopkinson bar, sled tests and cannons have been employed by industry.

While mechanical breakdown of PCB materials is being intensively studied by academia, manufacturing industry and even many government research agencies using broad computational methods, theoretical analysis and exploring vast number of constitutive model behaviors, relatively little attention has been given to investigate electromechanical behavior of circuitry subjected to harsh mechanical conditions. Electrical breakdown behavior of electronic components such as resistors, transducers and capacitors has been intensely investigated using empirical methods with concentration on the performance of raw materials. However, little attention has been given to the electromechanical performance of electronics under extreme conditions, which can explain some of the transient responses of electric components. In particular, capacitors, whether traditionally mounted or printed into the composite circuit board material, that undergo harsh mechanical stresses indicative of military applications have been slow to catch up with the rest of the technology, which

predominantly focuses on mechanical survivability of components. By developing computational models describing the piezoelectric behavior of the dielectric materials inside capacitors, transient electromechanical failure mechanisms of electronics, which are often disregarded as noise in the system, may be quantitatively predicted and reduced.

However, predicting electromechanical response of components subjected to harsh mechanical loadings on the order of 20,000 g is not trivial. Part of the problem in researching the behavior of the dielectric materials that are integrated inside the capacitors is due to the broad theory that requires intimate knowledge of both continuum mechanics, where a material's mechanical response is obtained using conservation of mass and momentum equations, and the classical electromagnetic (or at least electrostatic) theory coupled with thermodynamics. On the microscopic level, the overarching material models that require one to think of the ceramic dielectric materials inside capacitors in terms of their crystalline structure does not easily lend to picturing its relationships within the quantum mechanics physics framework or even atomic structure models. Also, from the manufacturing standpoint, dielectric crystalline materials, whether they possess piezoelectric, pyroelectric or ferroelectric properties have an inherent amount of variability that significantly affects their electromechanical response. For example, the same type of material, such as the Lead Zirconate Titanate (PZT)95/5 will have varying orthotropic elastic, piezoelectric and permittivity moduli as well as unique micro-structural defects due to slight differences in crystal growth and manufacturing techniques, which drastically change the electromechanical response of the material [11]. Making matters even more complicated are the difficulties in testing the electromechanical properties of the dielectric materials and inherent hazards associated with working with them based on the potentially large voltages that capacitors using such materials can generate.

Despite the difficulties of working with piezoelectric and ferroelectric materials, most of the research has been concentrated on experimentally observing the quality of voltage

and current output of the dielectric materials as they are subjected to various mechanical loads. Numerous tests have been performed to investigate the electromechanical response of the dielectric ceramic inside a Ferroelectric Generator (FEG) by sending a plane shock wave generated with explosives through the material [12–16]. Also, static and dynamic compressive experiments with the piezoelectric materials have been performed using three-point loading conditions and load drop tests to investigate dielectric properties such as electrical energy output [17, 18]. Finally, and only recently, more attention has been given to the effects of dielectric micro-structure, in particular characterization of polycrystalline domains using various scanning techniques and domain walls motion on the overall electromechanical properties of the ferroelectric materials [19].

While many experiments have been conducted to observe the behavior of dielectric materials, relatively little progress has been made in developing computational models and relationships between mechanical stress and the associated electrical outputs of different types of polarizable materials as used directly in electrical components such as capacitors. Most, if not all existing electromechanical response theory of dielectric materials has been based on the well established principles, starting with the conservation of mass and momentum, and ending with Gauss' law and Faraday's law [20]. Even though these principles provide a solid framework for developing computational models of electromechanical response of dielectrics, more information about the specific material properties such as polarizability, permittivity and elasticity, as well as the internal component structure is required to provide numerical solutions. Because these properties of dielectrics can vary wildly between different manufactured parcels of a particular material, and are often difficult to precisely measure, relationships for capacitance response under mechanical stress must be established in order to predict performance of capacitors that often employ ferroelectric materials as their insulators due to their high dielectric constant.

As previously discussed, multiple constitutive relationships of mechanical response of different classes of materials, such as polymers, ceramics and metals have been thoroughly developed based on phenomenological and empirical observations. Even relatively new material interface and crack propagation computational methods have been developed for various government and commercially available FEA codes. However, from a practical standpoint, especially in military applications, the reason for electrical component failure is irrelevant, as long the breakdown is significant enough to cause the product to malfunction. Therefore, this study is focused on modeling piezoelectric behavior of ferroelectric materials inside capacitors, which are critical to circuitry reliability of munitions that are exposed to extreme mechanical stress environments representative of military applications, by experimentally varying the mechanical stress magnitude and orientation of the mechanical shock and using computational models based on the well established classical theories mentioned above to predict stress induced capacitance behavior. Both mechanical breakdown of capacitors exposed to varying mechanical loads and transient electromechanical response of capacitors under shock are addressed to completely describe failure mechanisms of surface mounted components.

In order to accurately model and predict electromechanical response of piezoelectric and ferroelectric dielectric materials inside capacitors, a Quasi-Static Electric (QSE) field approximation is employed using the ALEGRA-EMMA code developed by Sandia National Laboratories (SNL) [21, 22]. However, before computationally predicting the electromechanical capacitance response, an accurate dynamic response model of the circuit board must be constructed. First, the mechanical stresses and an accurate dynamic response of a printed circuit board model is validated with the experimental results obtained using drop tower tests. Next, high-voltage and low-voltage Multilayer Ceramic Capacitors (MLCC), which use ferroelectric material for their dielectric are subjected to drop impacts with acceleration levels ranging between 500 - 24,000 g, and their capacitance



is measured using the RC time constant calculation method during the mechanical shock event. Finally, validated by the experiments, a FEA model of a series capacitor is created to simulate transient piezoelectric response of the ferroelectric dielectric inside a capacitor to predict capacitance variations during shock in order to help establish a set of design and exploitation criteria that better predict reliability and survivability of capacitors used in electronics exposed to high-g drop impacts. In summary, this work:

1. Establishes a computational dynamic response model for the printed circuit board undergoing impact shock tests in drop tower experiments.
2. Experimentally measures the capacitive response of capacitors exposed to high-g mechanical stress.
3. Based on the previously established dynamic model and experimentally gathered capacitance data, develops a computational model that predicts the electromechanical response of dielectric materials, and thus capacitance of MLCC, in order to fully describe failure mechanisms of components subjected to drop impacts.

Accomplishing the above three research objectives will, for the first time in literature, create an accurate computational model for board strain predictions validated with experimental data under high-g shock impact conditions an order of magnitude greater than standards specified by the JEDEC. Additionally, the uniquely applied RC monitoring technique will be tested under dynamic loading conditions and will provide experimental data for capacitance variations of components undergoing drop impacts. Finally, piezoelectrically induced capacitive changes of ferroelectric ceramics inside the MLCC will be quantified for the first time in literature using a modified constitutive relationship for calculating capacitance of devices, and an experimentally validated computational model of the components predicting their electromechanical response to mechanical stress.

## II. Literature Review

In this chapter the structure of capacitors and properties of their dielectric materials are discussed and the applicable portions of electromagnetic theory are reviewed. Next the body of knowledge that pertains to the science of piezoelectric dielectrics, as well as the failure mechanisms of capacitors, that was found in the literature, is assembled and analyzed, and the weak areas of information are identified. Finally, theoretical and mathematical background behind the Piezoelectric model of the finite element code ALEGRA-EMMA, that will be used to study the electromechanical response of dielectrics, is described.

### 2.1 Capacitors

In its simplest definition, a capacitor is an electronic device in an electrical circuit that stores energy. The property that differentiates capacitors from batteries is that the energy stored inside the capacitor can be accessed much more quickly than the energy stored in a battery, despite the fact that both capacitors and batteries contain insulating materials preventing the flow of electricity through them. Also, a battery provides a constant source of voltage over a relatively significant period of time while capacitors discharge almost instantaneously, over a short period defined by the RC time constant. While, the flow of Direct Current (DC) through the capacitor is blocked, Alternating Current (AC) can easily pass through the dielectric material of the capacitor. Thus, a capacitor in an electrical DC circuit can be thought of as a membrane inside a pipe of flowing water.

The water flowing in only one direction can not pass through the membrane, but the kinetic energy of the flowing water is stored as a potential energy in the membrane as it stretches due to its elastic nature. The higher the elasticity of the membrane, the greater amount of water that can be permitted to flow before the flow is stopped, the greater is the

potential energy that can be stored by the membrane. Just like in the above analogy, the greater the amount of electrical charge the capacitor can store, the greater its capacitance,  $C$ , as measured in Farads (F), where one Farad is the ratio between one Coulomb and one Volt ( $1F = C/V$ ). However, each membrane has a limit in the total amount of water that it can hold back, just like every capacitor has a breakdown voltage, or potential, beyond which the electrical breakdown of the insulating material begins.

Capacitors come in many shapes and sizes, and commercial models are often used in many applications, ranging from pulsed power devices [12], to signals processing and conditioning of electronics, to storing energy for starting machinery. The high energy release rate properties make capacitors very desirable to military applications. One of the applications of interest in this study is the use of capacitors, which store a significant amount of charge in order to provide a large amount of potential, (or voltage) on the order of more than 1 kV (kiloVolt), at a specified time to initiate a detonation of an explosive material. However, relatively low voltage capacitors, of approximately 10 VDC, are also used to run circuitry logic of electronic fuzes inside air munitions and must also survive under harsh mechanical loads. Therefore, while stability of high-voltage devices is important in terms of providing a constant amount of energy throughout the shock duration, the abundance of use of low-voltage capacitors in military, as well as civilian applications exposed to harsh conditions, is the main focus of this research.

### ***2.1.1 Capacitor Structure and Performance Factors.***

Capacitors can comprise several different structures, but they always consist of two or more conducting material electrodes separated by either vacuum or some type of electrically insulating material, called dielectric. In many instances, cylindrical capacitors, such as the ones employed in the coaxial cable are used by commercial industry to transmit signals, while capacitors requiring large single-use power sources often have multiple electrodes layered inside a dielectric, and are thus, labeled MLCC.

However, the simplest model of a capacitor, such as a two-plate capacitor, is a pair of metallic conducting electrodes with vacuum between them. If the two electrodes of overlapping area  $A$ , separated by distance  $d$ , contain an equal, but opposite charge  $Q$ , an electric field  $E$ , is produced between the plates. In the limit where  $d \ll A$ , as is the case for most capacitors, the potential between the two plates is given by Equation (2.1).

$$V = \frac{Qd}{\epsilon_0 A} \quad (2.1)$$

where  $\epsilon_0 = 8.85 \times 10^{-12}$  F/m is the permittivity in a vacuum. Since  $Q$  is proportional to  $V$ , the capacitance of a parallel-plate capacitor can be given by Equation (2.2).

$$C = \frac{\epsilon_0 A}{d} \quad (2.2)$$

If dielectric materials are substituted for the vacuum inside the device as the insulating agent, then the original electric field  $E_0$ , between the electrodes will be reduced due to various properties of the dielectric materials, by a factor  $\kappa$ , called the dielectric constant as seen in Equation (2.3), while at the same time modifying the capacitance  $C$ , potential  $V$ , and exposing the relative permittivity of the dielectric  $\epsilon$ .

$$\kappa = \frac{\epsilon}{\epsilon_0} = \frac{C}{C_0} = \frac{V_0}{V} \quad (2.3)$$

Permittivity of a dielectric material can be thought of as a property that describes how much the material “permits” the external electric field to affect it or how much the material affects the overall external field passing through it. Such effects as internal polarization of the material in response to an external electric field is one example of permittivity. The greater the permittivity, the greater the polarization of the material, the greater the internal electric field that counteracts the external applied field.

Since capacitance  $C$ , is arguably the most important property of a capacitor and varies greatly with the type of dielectric material that separates the electrodes according to Equation (2.4), it is of the utmost importance to understand the properties of the dielectric

materials in order to study the electromechanical behavior of capacitors and ultimately electromechanical failure mechanisms.

$$C = \frac{\epsilon A}{d} \quad (2.4)$$

Also, due to the fact that the energy  $U$ , stored in the parallel-plate capacitor is given by Equation (2.5),

$$U = \frac{1}{2} QV = \frac{1}{2} CV^2 \quad (2.5)$$

and realizing that the quantity  $Ad$  is the volume that is occupied by the dielectric insulator, the energy per unit volume  $u_e$ , of the dielectric is shown in Equation (2.6).

$$u_e = \frac{1}{2} \kappa \epsilon_0 E^2 = \frac{1}{2} \epsilon E^2 \quad (2.6)$$

The simple two-plate capacitors are limited by their design to a certain amount of charge and potential they can hold. However, capacitance can be increased by adding electrodes and the number of dielectric layers  $n$ , inside the device, which modifies the capacitance in Equation (2.4) to Equation (2.7), in the case of MLCC.

$$C = \frac{\epsilon A}{d} n \quad (2.7)$$

In Equation (2.7),  $A$  is again the overlapping area of plates and  $d$  is still the thickness of the dielectric between two individual electrodes. Two main types of MLCC structures exist: parallel-plate capacitors and series, or floating electrode capacitors [23]. Parallel-plate capacitors comprise of electrodes, which all connect to alternating terminals as seen in Figure 2.1. Electrodes and terminals always consist of electrically conductive materials, usually copper, nickel or some type of silver alloy [24]. The two terminals, as the word suggests, are oppositely and either positively or negatively charged when current is applied, and also sometimes contain mechanically flexible materials that can reduce mechanical stress during shock [25].

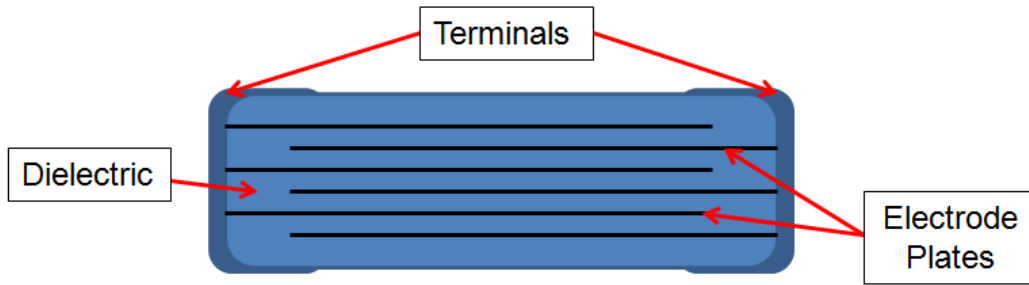


Figure 2.1: Parallel-Plate Capacitor Electrode Structure

Series electrode capacitors contain the same components as their parallel-plate counterparts, but also encompass “floating” electrodes which do not physically connect to terminals as seen in Figure 2.2. The main advantage of series capacitors is in a case of

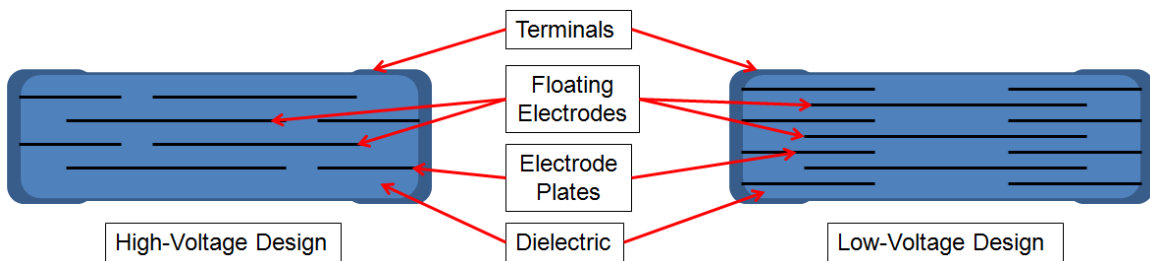


Figure 2.2: Series/Floating Electrode Capacitor Structure

mechanical failure when the oppositely charged electrodes are exposed during fracture of the dielectric material. If the dielectric material is cracked in the parallel-plate capacitor, the capacitor is shorted at potentially inappropriate time, possibly damaging other electrical components in the circuit. The series capacitor design fails to an open, and thus prevents the damaging discharge, which is a highly desired, and sometimes a necessary, safety feature of high-voltage devices rated to 500 VDC and above [25]. The only effect of loss of contact of electrodes with the terminal is the reduction in capacitance proportional to the number of failed connecting electrodes [25]. The disadvantage of series capacitors is that their

electrode overlapping area is reduced and their operation induces an asymmetric collection of charge on the floating electrodes, reducing the overall capacitance of the component, despite the high potentials that are allowed [23]. Hence, small high-voltage capacitors with high permittivity dielectrics are nearly all series capacitors [24].

Regardless of the type or application of the capacitor, its performance as an electrical component in a simple RC circuit under DC can also be linked to the function of voltage across the device over time [26]. By applying a constant voltage  $V_0$ , to a previously uncharged component of capacitance  $C$ , through a resistor of known and constant resistance  $R$ , the potential  $V$ , across the capacitor according to Kirchhoff's rule is given by  $V = V_0 - V_R$ . The flow of charge  $Q$ , over time  $t$ , is the definition of current  $I$ , in the circuit given by  $I = dQ/dt$ , and thus, from Equation (2.1) the voltage across the capacitor can be written as Equation (2.8).

$$\frac{Q}{C} = V_0 - R \frac{dQ}{dt} \quad (2.8)$$

If the capacitor is initially uncharged, solving for the current  $I = dQ/dt$  and substituting  $V_0/R$  for the initial current  $I_0$ , the voltage drop across a charging capacitor as a function of time is given by Equation (2.9).

$$V(t) = V_0(1 - e^{-t/RC}) = V_0(1 - e^{-t/\tau}) \quad (2.9)$$

Similarly, if the capacitor was previously charged with potential  $V_0$ , and allowed to discharge through a resistor of constant resistance  $R$ , the voltage  $V(t)$ , of the discharging capacitor is given by Equation (2.10).

$$V(t) = V_0 e^{-t/\tau} \quad (2.10)$$

The time constant  $\tau = RC$  is defined as the time it takes the capacitor to charge to 63% of its full capacity in the charging case, or for the charge to decrease to 37% of its original value in the discharging case, and is a function of only capacitance and resistance [26]. Thus, if resistance remains constant, by calculating the time constant, and thus extracting

capacitance, permittivity of the dielectric material can be easily obtained, assuming the mechanical structure of the component remains unchanged. The capacitor size and proportions are often dictated by the geometric limitations based on each application, and for a specified amount of potential, and in turn electric field between the electrodes, the amount of energy stored in the capacitor varies only with the properties of the dielectric material, directly relating to volumetric efficiency of the device. Since both the capacitance and energy are almost exclusively dependent on the properties of the dielectric material, such as the relative permittivity and dielectric strength, understanding them is critically important for predicting electrical and electromechanical behavior of capacitors subjected to mechanical stress.

### ***2.1.2 Dielectric Materials.***

There is an incredibly wide variety of dielectric materials, ranging from different types of ceramics, to composites such as woods and paper, to polymers and even air. But, essentially, all dielectrics share one property - they are insulators and do not permit the flow of electric charge through their medium. The extent of their dielectric strength varies greatly based on the material's atomic, molecular and microscopic structures, but given enough electric potential, charge will still pass through the material.

However, just because the material does not permit the flow of charge, it does not mean that dielectrics are not affected, or do not affect the electric field between the electrodes in the capacitor. In fact, regardless of the dielectric constant, all dielectrics are polarized to some extent by an electric field that is present between the electrodes. Polarization processes in a dielectric material can take place on an atomic scale, through shifting of the ionic sublattice crystalline structure, rotation of molecular or domain dipoles or through diffusion of charge until a potential barrier such as an inclusion or impurity stops the rearrangement of charge [19].



If an atom is viewed as having a positively charged nucleus and a negatively charged spherical shell of electrons, atomic polarization under an applied electric field occurs when a small displacement of electrons relative to the nucleus is aligned along the imposing electric field [27]. Atomic polarization occurs to some extent in all dielectric materials that consist of neutrally charged atoms. On the other hand, ionic polarization under applied electric field occurs when cation and anion sublattices shift in a crystalline structure, which is indicative of the ceramic dielectric materials [27]. In some molecules, such as water, the total negative charge center of the oxygen atom is offset from the total positive charge of the hydrogen atoms resulting in a slightly dipolar molecular structure. In the absence of an external electric field, water molecules are randomly arranged and do not produce a net dipole moment. However, in the presence of an electric field, dipolar water molecules align in the direction of the external electric field to produce net polarization, the strength of which is proportional to the strength of the electric field up to a certain limit [26]. Finally, on the microscopic level, if charge carriers are stopped at either the grain or phase boundaries, that can be thought of either as physical material porosity or electrostatic boundaries respectively, the resulting effect is the production of net diffusional polarization [19].

Regardless of the polarization process, its net result is the build up of bound charge density  $\sigma_b$ , on the surface of the dielectric due to the fact that insulating materials cannot conduct charge. Thus, inside the dielectric material and between the oppositely polarized dielectric material surfaces, an internal electric field  $E_b$ , due to bound charge accumulation, is created. In the case of a capacitor, electrodes that are adjacent to the dielectric material surfaces contain free charge density  $\sigma_f$ , that is free to move about the conductor and the free charge on the surface of the electrodes creates an initial external field,  $E_0$ . In the case where the dielectric material is thin and the distance between electrodes is small, the net electric field can be calculated using the difference between the initial applied electric field,

$E_0$ , and the internal electric field,  $E_b$ , as seen in Equation (2.11).

$$E = E_0 - E_b = \frac{\sigma_f}{\epsilon_0} - \frac{\sigma_b}{\epsilon_0} = \frac{E_0}{\kappa} \quad (2.11)$$

Solving for the bound charge density  $\sigma_b$ , a relationship emerges in Equation (2.12) based on the free charge density and dielectric constant.

$$\sigma_b = \left(1 - \frac{1}{\kappa}\right)\sigma_f \quad (2.12)$$

The bound charge electric field counteracts the applied electric field. In the vacuum, without any dielectric material, where  $\kappa = 1$ , the total bound charge density is zero. However, if the dielectric is replaced with a conductor, the dielectric constant would approach infinity and, as expected, the bound and free charge densities would be equal.

Under strong enough external electric fields, all insulating materials will undergo some combination of the above mentioned polarization processes [27]. However, the direct relationship between the applied electric field and the subsequent polarization classifies materials into separate categories. Dielectrically polarized materials create a proportional linear relationship between the applied electric field and the resultant polarization throughout a wide range of electric field strengths. On the other hand, paraelectric polarization is indicative of materials that have varying permittivity and exhibit different polarization versus electric field strength slopes. For example, as the external electric field is applied, polarization is increased proportionally as a linear function with one slope. However, as the electric field is increased past a certain limit, polarization increases with a different slope. Paraelectric polarization displays permittivity as a function of the applied electric field. However, in both dielectric and paraelectric polarization processes, once the external electric field is removed, polarization disappears and returns to its original null net polarization value without displaying any hysteresis effects [27].

Ferroelectric materials, which usually are a type of a ceramic, exhibit a hysteresis relationship between the applied electric field and polarization [11]. Starting with the

anti-ferroelectric polarization state of the material, where no net polarization is present without an applied electric field, as the external field is increased, the ferroelectric material first exhibits paraelectric properties, where permittivity varies as a function of the electric field strength. Once the electric field reaches a certain polarization saturation limit and is then brought back down to zero, a certain amount of remnant polarization remains [11]. Increasing the external electric field in the opposite direction to the so called coercive level, only switches the polarization of the ferroelectric material, but the remnant polarization magnitude remains unchanged [11]. The dielectric, paraelectric and ferroelectric polarization processes can be seen in Figure 2.3, Figure 2.4 and Figure 2.5 respectively. Care must be taken not to confuse the terms dielectric material, which is any

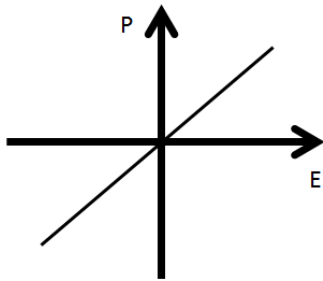


Figure 2.3: Dielectric Polarization

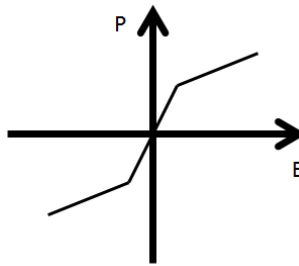


Figure 2.4: Paraelectric Polarization

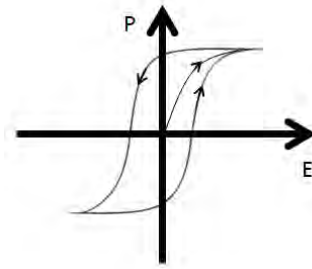


Figure 2.5: Ferroelectric Polarization

type of insulating material, and dielectric polarization, which is simply a type of linearly proportional polarization behavior of a material (including dielectric material). Thus, not all dielectric materials, or insulators, exhibit dielectric polarization behavior.

While classification of dielectric materials based on their response to an external electric field is important in order to predict the amount of energy that can be stored in a capacitor, a wide range of crystalline structured materials also exhibit an electrical response to both mechanical and thermal loads. Crystalline structured materials that exhibit

responses to mechanical loads, such as compressive or tensile strains, stresses and shocks are called piezoelectric. Piezoelectric materials occur naturally in the form of quartz and can also be man-made. Piezoelectric materials are further divided into pyroelectric materials, which exhibit a change in polarization in response to temperature, and non-pyroelectric, which do not display electrothermal response. For example, quartz is a non-pyroelectric crystal, which responds only to mechanical stresses, while crystals such as tourmaline also produce an electrical response due to the change in temperature. All pyroelectric materials exhibit some type of piezoelectric properties, due to the inevitable mechanical stresses imposed on the material with varying temperature gradients, but only certain piezoelectric crystals exhibit pyroelectric properties.

Pyroelectric materials are then further divided into non-ferroelectric materials, such as tourmaline, and ferroelectric materials, such as PZT and Barium Titanate ( $\text{BaTiO}_3$ ), which exhibit remnant polarization after applying a static electric field and then removing it in the process called poling. The behavior of the ferroelectric materials subjected to mechanical and thermal stresses, as well as to an external electric field, is extremely complex and relatively poorly understood. Ferroelectric material electromechanical response is dependent on the exact crystal structure based on the chemical and ionic composition, which sometimes uses doping agents in order to create more desirable qualities for specific applications [19]. The behavior is also highly dependent on the orientation of polarized crystalline structure, both on the molecular/sublattice level and on the macroscopic/crystalline level where domains and domain walls of regions have closely aligned polarization directions [11]. The effect of domains and domain walls is evident in the ferroelectric material's tendency to exhibit properties that are qualitatively closer to paraelectric processes in the presence of a static electric field, instead of well-defined hysteresis loops when considering the permittivity of the dielectric as shown in Figure 2.6 and Figure 2.7. While the coercive field required for phase transition of the ferroelectric

material is increased in magnitude between single crystal structure and the multi-domain polycrystalline structure, the net remnant polarization after the phase transition or poling is reduced [11].

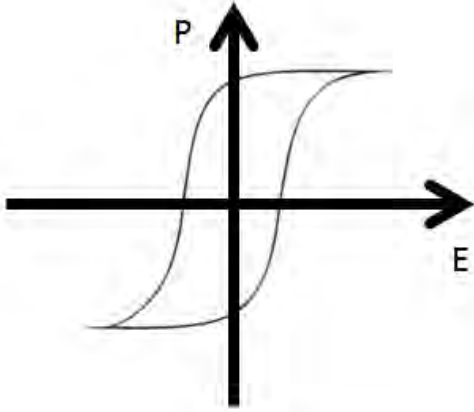


Figure 2.6: Single Crystal Hysteresis

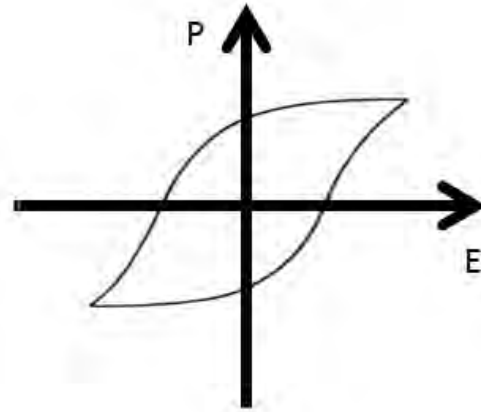


Figure 2.7: Multiple Domain Hysteresis

On top of complex ferroelectric hysteresis behavior based on the polycrystalline and sublattice structures, as well as chemical make up of the crystals, ferroelectric behavior is also limited to a certain range of temperatures. All ferroelectric materials have a Curie temperature limit  $T_c$ , above which the spontaneous polarization of the crystals is reduced to zero and again, the hysteresis behavior is reduced to paraelectric properties [27]. However, once the temperature is brought back to below the Curie temperature, as long as the ferroelectric material was previously poled, both hysteresis and net polarization properties return.

Since ferroelectric materials are also piezoelectric in nature, applying static mechanical stresses will invoke an electromechanical response through temporary changes in polarization, but will not affect the net remnant polarization once the mechanical load is removed. Also, switching of the electric field will cause a phase transition in ferroelectric

materials to occur, and while the direction of polarization will change, the magnitude of the remnant polarization will still be unaffected. Finally, increasing the temperature of the material past the Curie point and reducing it below the limit again will also leave the same remnant polarization as long as the static electric field is removed. However, in order to extract electrical energy stored in the polarized ferroelectric material through the poling process, the material must be brought to its original anti-ferroelectric state, where in the absence of an external electric field, net polarization on the macroscopic, domain level, is returned to its pre-poled value of zero [12].

The energy involved in the transition of the material from the ferroelectric to anti-ferroelectric state, is the basis of pulsed power devices like the FEG and high voltage capacitors used in detonations of munitions. The most common method of depolarizing the ferroelectric material and extracting the energy stored in the internal electrical field, is through the use of high mechanical stresses obtained from an explosive shock wave [12]. Thus, as will be evident later in this chapter, a significant amount of empirical studies and numerous experiments have been performed by academia, the manufacturing industry and even government agencies to study the electromechanical response of the ferroelectric materials under extreme mechanical shocks produced by explosive pressure waves. Also, numerous studies have been performed to characterize the behavior of ferroelectric ceramics undergoing compressive and tensile static loads, as well as compressive stresses in transducers generated by dropped objects. Since ferroelectric materials by definition also exhibit piezoelectric characteristics, a significant amount of experimental work has been devoted to strictly piezoelectric response to understand the underlying mechanical stress responses of such ceramics without the added complexities of hysteresis loops of ferroelectric material behavior.

Unfortunately, high-voltage capacitors, whether they include piezoelectric or ferroelectric dielectric materials as their insulators, are exposed to mechanical stresses that orig-

inate from dynamic circuit board, or any other type of platform response to high accelerations during impact. While compressive stresses, and thus generated pressures inside the material due to drop impact accelerations are usually much lower than pressures generated by an explosive shock wave, the pressures present in the insulating material from a drop impact still evoke an electromechanical response that at least temporarily changes the polarization and dielectric properties of the capacitors. However, the extent to which changes in dielectric properties affect capacitor performance in the circuit, and ultimately its capacitance, has not been described or explained anywhere in literature with enough detail to make predictions about component reliability.

On the other hand, while static compressive and tensile tests may create similar mechanical loads on the material as stresses generated by a drop impact, the dynamic electromechanical response is neglected. However, even the studies, which through experiments quantify the electromechanical response of piezoelectric or ferroelectric materials, apply only to a narrow range of materials that are used in such studies, where as mentioned earlier, each batch of material that is manufactured even by the same company may have large variations in electromechanical behavior [24]. Furthermore, mechanisms that describe the effects of different dielectric material properties on the capacitor behavior in high-stress environments, while taking into account dynamic responses of such devices, have been almost entirely neglected.

The poorly developed electromechanical response relationships of capacitors inside circuitry create a large gap in the overall understanding of how dielectric materials behave under the studied conditions of compressive and tensile mechanical stresses. However, extrapolating whatever empirical data that exists to different temporal scales or to different mechanical stress mechanisms without first attempting to quantify, or at least address the underlying mechanical and electromechanical behavior of the dielectric is unwise. Thus, the current work is focused on studying mechanical and electromechanical response of

MLCC exposed to high-g environments on the order of 20,000 g using both computational and experimental methods.

First, mechanical stresses generated during high-g drop impact must be obtained through controlled experiments measuring dynamic response of the PCB and then accurately modeled with solid dynamics software under the same conditions in order to accurately replicate acceleration profiles on the surface mounted capacitors. Then, devices that use ferroelectric materials for dielectric must be methodically exposed to the previously characterized stresses in the laboratory and their capacitance measured at high enough data rate in order to ensure rudimentary description of mechanical and electromechanical failure mechanisms, which relate to component performance and reliability. Finally, capacitance response to mechanical stress of ferroelectric ceramic devices must be calculated using computational methods and models available in FEA, that were developed from the overarching continuum mechanics and electromagnetic theories, in order to verify experimental capacitance measurements, and predict electromechanical response of MLCC in high-g drop impact environments. Before further describing the existing literature on the topic, and providing a detailed mathematical description of how such software computes the piezoelectric response of dielectric materials, it is important to provide a rudimentary review of the governing equations.

## **2.2 Theoretical and Mathematical Backgrounds**

When understanding the electromechanical response of dielectric materials, as the make-up of the word would suggest, one should address at least two different concepts, electrical response and mechanical response of continuum materials. First, the laws of the conservation of mass, momentum and energy, as well as some constitutive material behaviors, such as Hooke's law and other material responses to mechanical loads, be they compressive, tensile or shock stresses in nature, are mentioned. Second, the principles describing how materials respond electrically to a certain electromagnetic stimuli along



with relationships between electric displacement and polarization are addressed. The difficulty comes not necessarily in understanding each law or principle individually, but upon trying to understand their simultaneous and combined effects, and interactions in the presence of the physical medium. It is important to note, that the current study will not be concerned with atomic structures of materials or with relativistic concepts of electromagnetic theory, because the behavior of capacitors in applications of interest may be adequately explained without the use of such principles.

Due to the electromechanical nature of dielectric materials, it is not possible to separate mechanical response of the medium from the electromagnetic behavior of materials under mechanical shock. In fact, as mentioned earlier, in piezoelectric materials applied stress evokes an electrical response and the material is strained in the presence of an external electric field. Thus, due to the coupling between the laws of conservation of mass, momentum and energy in the continuum, and the classical electromagnetic theory, as it applies to various materials, the equations for electromechanical effect, Equation (2.13) - Equation (2.19), must be solved simultaneously [20].

$$\dot{\rho} + \rho \operatorname{div} \dot{\mathbf{x}} = 0 \quad (2.13)$$

$$\rho \dot{\mathbf{g}} = \operatorname{div} \mathbf{T} + \rho \mathbf{b} \quad (2.14)$$

$$\rho \dot{x}_{[igj]} + T_{[ij]} = 0 \quad (2.15)$$

$$\rho \dot{\mathcal{E}} = \operatorname{div} T^T \dot{\mathbf{x}} + \rho \dot{\mathbf{x}} \cdot \mathbf{b} + \rho h - \operatorname{div}(\mathbf{q} + \mathcal{E} \times \mathcal{H}) \quad (2.16)$$

$$\operatorname{div} \mathbf{D} = q \quad (2.17)$$

$$\operatorname{curl} \mathcal{E} = -\dot{\mathbf{B}}^* \quad (2.18)$$

$$\mathbf{D} = \epsilon_0 \mathbf{E} + \mathbf{P} \quad (2.19)$$

The first four equations, Equation (2.13) through Equation (2.16) are based on classical continuum mechanics and thermodynamic principles, and are written in their strong forms

of the material derivatives. The Gauss' law represented by Equation (2.17) is also written in vector calculus notation using a strong form, while Faraday's law converted into field equation using the Stokes' theorem is presented in Equation (2.18). The last relationship in Equation (2.19), simply describes theoretical behavior of polarizable materials. Because this system of governing equations is the foundational framework for numerical solutions to electromechanical response of piezoelectric materials, it is important to take a closer look at what each relationship represents, their origins and their possible limitations.

The conservation of mass principle of continuum mechanics is imposed using Equation (2.13) in the system of governing equations, where  $\rho$  is material density,  $\dot{\rho}$  is the rate of change of density and  $\dot{\mathbf{x}}$  is the material trajectory velocity function given by the partial time derivative  $\dot{\mathbf{x}} = \frac{\partial \mathbf{x}(\mathbf{X}, t)}{\partial t}$ , of material point  $\mathbf{X} = (X_1, X_2, X_3)$ . The material is at an initial state  $S_0$ , at  $t = 0$ , and after time  $t$ , is in the state  $S_t$ , as shown in Figure 2.8.

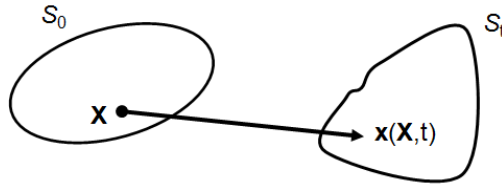


Figure 2.8: Continuous Body Trajectory Using Euler's Notation

In the Euclidean three dimensional space, the deformation tensor, which is used later in describing the implementation of the piezoelectric model in ALEGRA-EMMA can also be represented with nine partial derivatives in Equation (2.20), where time  $t$ , is fixed and only the position of the material  $\mathbf{X}$ , is varied.

$$F_{ij}(\mathbf{X}, t) = \frac{\partial x_i(\mathbf{X}, t)}{\partial X_j} \quad (2.20)$$

When working in an inertial frame of reference, laws of mechanics are bound by the concepts of momentum  $\mathbf{G}$ , force  $\mathbf{F}$ , angular momentum  $\mathbf{L}_O$ , and torque  $\mathbf{M}_O$ .

The integral form of these concepts is given respectively by Equation (2.21) through Equation (2.24) [20]

$$\mathbf{G} = \int \dot{\mathbf{x}} dm \quad (2.21)$$

$$\mathbf{F} = \oint \mathbf{t} dS + \int \mathbf{b} dm \quad (2.22)$$

$$\mathbf{L}_O = \int (\mathbf{x} - \mathbf{x}_O) \times \dot{\mathbf{x}} dm \quad (2.23)$$

$$\mathbf{M}_O = \oint (\mathbf{x} - \mathbf{x}_O) \times \mathbf{t} dS + \int (\mathbf{x} - \mathbf{x}_O) \times \mathbf{b} dm \quad (2.24)$$

where  $\mathbf{t}$  is the surface force per unit area (traction per unit area),  $\mathbf{b}$  is body force per unit mass, and angular momentum and torque are defined with respect to position  $\mathbf{x}_O$ . For the inertial frame, two Euler's laws of mechanics emerge, where the time derivative of momentum is equal to force,  $\dot{\mathbf{G}} = \mathbf{F}$ , and time derivative of angular momentum is equal to torque,  $\dot{\mathbf{L}}_O = \mathbf{M}_O$ . From Cauchy's theorem, substituting the Euler's first law into Equation (2.21) and Equation (2.22), there exist nine functions  $T_{ij}$ , in three dimensions with the stress tensor given by  $\mathbf{t} = T\mathbf{n}$ , where  $\mathbf{n}$  is a vector normal to the surface  $S$ . Combining the two integral laws, Cauchy's first equation emerges as Equation (2.25).

$$\rho \ddot{\mathbf{x}} = \mathbf{div} T + \rho \mathbf{b} \quad (2.25)$$

By denoting  $\mathbf{g}$  as the momentum per unit mass, the second equation, Equation (2.14), of the electromechanical response system of governing equations emerges. Following a similar procedure using the second Euler's law, leads to the three equations described by Equation (2.15) in index notation. It is important to note that in the absence of an electromagnetic field, the generalization for  $\mathbf{g}$  vanishes and reduces to  $\mathbf{g} = \dot{\mathbf{x}}$ . Thus, the Euler's two laws are derived and applied to the electromechanical behavior of materials using the concepts of conservation of momentum.

Now it is important to shift attention to principles of thermodynamics, from which the conservation of energy law, represented by Equation (2.16) is derived. By viewing energy

as a continuous function of mass, and denoting  $\varepsilon$  as the energy per unit mass, the total energy can be written as an integral of  $\varepsilon$  over the entire body of mass. Similarly, heating  $Q$ , can be given by the sum of the surface integral over the body surface of contact heating per unit area  $\beta$ , and the integral of the body heating per unit mass  $h$ . Both energy  $E$ , and heating  $Q$ , can be represented respectively in Equation (2.26) and Equation (2.27) [20].

$$E = \int \varepsilon dm = \int \rho \varepsilon dV \quad (2.26)$$

$$Q = \oint \beta dS + \int h dm \quad (2.27)$$

Modifying the force relationship in Equation (2.22), to describe the forces acting on the body  $\Pi$ , and applying the first law of thermodynamics, which states that energy cannot be created or destroyed, but can only be transferred from one form into another, an integral form of the conservation of energy law appears in Equation (2.28).

$$\dot{E} = \dot{\Pi} + \dot{Q} = \frac{d}{dt} \int \varepsilon dm = \oint \dot{\mathbf{x}} \cdot T \mathbf{n} dS + \int \dot{\mathbf{x}} \cdot \mathbf{b} dm + \oint \beta dS + \int h dm \quad (2.28)$$

Since the contact heating per unit area can also be written in the form  $\beta = -\mathbf{q} \cdot \mathbf{n} = -q_n$ , where  $\mathbf{q}$  is the heat flux, Equation (2.28) can be presented by Equation (2.29).

$$\rho \dot{\varepsilon} = \text{div } T^T \dot{\mathbf{x}} + \rho \dot{\mathbf{x}} \cdot \mathbf{b} + \rho h - \text{div } \mathbf{q} \quad (2.29)$$

However, the above equation does not take into account the energy flux of the electromagnetic field. With the introduction of concepts of electromotive intensity  $\mathcal{E} = \mathbf{E} + \dot{\mathbf{x}} \times \mathbf{B}$ , and magnetomotive intensity  $\mathcal{H} = \mathbf{H} - \dot{\mathbf{x}} \times \mathbf{D}$ , where  $\mathbf{E}$  is the electric field,  $\mathbf{B}$  is the magnetic field,  $\mathbf{H}$  is the current potential and  $\mathbf{D}$  is the charge potential, later defined as electric displacement for dielectric materials, Equation (2.29) can be rewritten in its strong form of Equation (2.16). Thus, the conservation of energy relationship in the system of governing equations describing the electromechanical response originates from the first law of thermodynamics and is modified using the energy flux vector  $\mathcal{E} \times \mathcal{H}$ , emanating from the electromagnetic fields.

The relationship in Equation (2.17),  $\text{div } \mathbf{D} = q$ , where  $\mathbf{D}$  is electric displacement and  $q$  is the total charge, is derived from observations of experiments, and simply relates to an integral form of the Gauss' law as shown in Equation (2.30).

$$\oint_S E_n dS = \frac{1}{\epsilon_0} Q_{net} \quad (2.30)$$

The above equation is one of Maxwell's equations for electricity and magnetism and states that the flux of the electric field  $E_n$ , normal to any closed surface  $S$ , is equal to the net charge  $Q_{net}$ , enclosed by the surface multiplied by  $1/\epsilon_0$ . The experimental basis for this law is Coulomb's law, which implies that the electric field due to a point charge reduces with the square of the distance from the center of charge. The relationship in Equation (2.30) also describes how the electric field lines flow from the positive to the negative charge [26].

Another one of Maxwell's relationships represented in Equation (2.18),  $\text{curl } \mathcal{E} = -\dot{\mathbf{B}}$ , where  $\mathcal{E}$ , as stated earlier is the electromotive intensity, can be related to Faraday's law presented in Equation (2.31).

$$\oint_C \mathbf{E} \cdot d\mathbf{l} = -\frac{d}{dt} \int_S B_n dS \quad (2.31)$$

According to the above equation, the curl of electromotive intensity, which is represented by the integral of the electric field through any closed curve  $C$ , and sometimes also called electromotive force, is equal to the negative time rate of change in magnetic flux through the surface  $S$ , bounded by the curve. However, the surface does not have to be closed, and thus magnetic flux is not necessarily equal to zero. Essentially, Equation (2.18) relates the electric field lines to the change in magnetic flux and describes how electric field relates to the time rate of change in magnetic field.

Up to this point, Gauss' law and Faraday's law have been describing the properties and interactions between the electric fields and magnetic fields in free space. While parallel plate capacitors with a vacuum between electrodes do exist, the primary interest in this study is to understand the electromechanical response of dielectric material under

mechanical stress. Therefore, the last equation in the system is the formulation that relates polarization of materials in the presence of electric fields, which was introduced along with the concepts of bound charges in Section 2.1.2, and is sometimes referred to as Maxwell's equation for polarization in media.

Since polarization can be viewed as redistribution of bound charge density  $q_b$ , in the material creating charge potential  $\mathbf{D}_b$ , due to the said bound charge, a relationship defining polarization  $\mathbf{P}$ , emerges as  $\mathbf{D}_b = -\mathbf{P}$ , where after applying Gauss' law, the relationship can be described by Equation (2.32).

$$q_b = -\text{div } \mathbf{P} \quad (2.32)$$

However, since bodies can be charged, and polarization alone can not account for it, there are free charge densities  $q_f$ , that together with bound distributions make up the total charge density  $q = q_f + q_b$ . By extension, partial free charge can be written in Equation (2.33).

$$\mathbf{D}_f = \mathbf{D} - \mathbf{D}_b = \mathbf{D} + \mathbf{P} \quad (2.33)$$

Applying Gauss' law,  $\text{div } \mathbf{D} = q$ , to Equation (2.33), the partial free charge potential relationship is formulated as  $\mathbf{D}_f = \epsilon_0 \mathbf{E} + \mathbf{P}$ . Since only the partial charge potential is represented in the formulation, the subscript  $f$  can be dropped and the relationship in Equation (2.19) results, where  $\mathbf{D}$  is called electric displacement. Maxwell's equation for polarization in media simply states that electric displacement is the sum of the effects of the external electric field in free space and the material net polarization, which itself can be a function of the electric field.

The electromechanical response governed by Equation (2.13) through Equation (2.19) provides a robust theoretical and mathematical framework when considering behavior of dielectric materials. However, this system of seven equations does not produce intuition when investigating the behavior of materials that are used to solve real engineering problems. To complicate the subject even further, as discussed in Section 2.1.2, mechanical properties of media such as molecular structure and granularity, and chemical composition

of solids that frame the crystalline structure and ionic behavior, have a profound effect on electromechanical properties of the materials, but are only indirectly accounted for in the governing equations. Thus, the link between theory and application is weak, and any further investigation into relationships between the measurable quantities such as elasticity, polarization, permittivity, and dynamic stress, is warranted in order to be able to properly predict electromechanical response of capacitors subjected to realistic mechanical loads.

While analytical solutions to the above governing equations even for simple and purely academic geometries are possible (even though they are not trivial), analytical solutions based on these theoretical concepts to the more complex and real world materials and applications are almost impossible. These difficulties are perhaps the greatest reasons for using the purely empirical, and only relatively recently, numerical approaches to studying the electromechanical response of materials. The current work attempts to combine the computational solution, validated by experiments, in order to advance the theory of piezoelectric response of ferroelectric dielectric inside ceramic capacitors. As can be seen in the next section, which attempts to address the depth and breadth of study and literature on the behavior of piezoelectric dielectric materials, the generalized theory of electromechanical behavior of these materials is rudimentary and warrants more attention.

### **2.3 Ferroelectric Material Theory and Polarization Characterization Tools**

Quartz is a common material on earth's surface and ever since the observation that striking it with a ferrous rock produces a spark, crystalline materials have been used by humans for centuries to start a fire [28]. Piezoelectric properties of quartz were discovered in the late 19th century by Jacques and Pierre Curie, and since then, crystalline materials, which are found in nature and exhibit electromechanical properties, have found a wide range of applications [29]. However, it was not until the mid 20th century that people have become almost completely dependent on materials that possess a definite electromechanical response. Now, uses of piezoelectric materials include spark generators

in common household appliances such as gas stoves, sensors in the form of transducers, including speakers and microphones, high voltage generators and even fuzes for military applications [30].

It was not until the late 1950s when materials with piezoelectric properties found their way into unconventional uses, such as the dielectric material between the electrodes in capacitors, which helped jump start the computer age. Also, the constant drive to miniaturize various electronic components, pushed an innovative use of piezoelectric materials as an insulator due to their high permittivity. Today, piezoelectric materials are used extensively in aerospace technology, as well as in air munitions fuze circuitry.

In particular, ferroelectric ceramic capacitors, which have a high relative dielectric constant, on the order of  $10^3$ , have become almost prolific in recent military and commercial applications, which require high power density materials [31]. Unfortunately, due to their electromechanical nature, piezoelectric materials, and especially ferroelectric ceramics, have strong undesirable instabilities in their dielectric properties based on some external physical parameters, such as temperature, different types of mechanical stress loads (tensile, compressive, dynamic acceleration) and external electric fields. Also, as mentioned earlier, both elastic and piezoelectric moduli of ferroelectric materials vary wildly with the exact chemical composition, different manufacturing processes, microstructural impurities, polarization domains and even degrade with age. Even with as wide of a use of these dielectric materials as is ongoing today, the critical and very complex relationships between the external electromechanical stimuli and the dielectric response of piezoelectrics are still poorly understood. In fact, the study of piezoelectric ceramics can be described as extremely compartmentalized at best.

The partitioning of the study of piezoelectric material behavior is in both the methods of studying these materials, such as computational and experimental investigations, as well as based on the particular application of dielectric materials. For example, the behavior of



a thin film application of ferroelectric PZT on a substrate that undergoes relatively benign mechanical loads when recording acoustic waves is much different from the investigation of bulk PZT material in the FEG subjected to shocked compressive mechanical stresses with pressures approximately eight orders of magnitude higher [12]. As a result, few constitutive relationships have been proposed, and even fewer have been validated, to describe the macroscopic behavior of piezoelectric materials, and thus, generalize their electromechanical response. Even smaller number of relationships have been developed to predict capacitance response of ferroelectric ceramic devices. Due to the small number of constitutive models that exist to predict the behavior of dielectric material properties in the capacitors subjected to environmental conditions for which they were intended, it is extremely dangerous to extrapolate the limited body of knowledge that does exist, to correctly predict the behavior of dielectric materials inside the capacitor undergoing untested dynamic mechanical loads such as drop impacts.

Interestingly enough, before thoroughly understanding the purely piezoelectric behavior, most of the focus was transferred to studying the more complex electromechanical properties of ferroelectric ceramic materials, which as stated earlier, also possess complex hysteresis properties, but also are more widely used as dielectric materials in the capacitors. Perhaps the most common and studied theories applied to the ferroelectric materials are based on the Landau concepts of free energy  $\mathcal{F}$ , developed in the 1950s, which are phenomenologically fitted to the sixth-degree polynomial and quantitatively attempt to describe the polarization as a function of applied electric field and mechanical stress. In Landau theories, free energy is a measure of symmetry constructed from polarization scalar order parameter and is a physical entity that is zero in the high-symmetry phase, changing continuously to a finite value as the symmetry is lowered [32].

The first of the Landau relationships is the Landau - Devonshire (LD) theory, which is most applicable to the bulk ferroelectric materials with uniform polarization near the

Curie temperature,  $T_C$  [32, 33]. The LD theory assumes that the polarization is uniform throughout the crystal and that it responds to both electric fields and strain fields in one dimension according to Equation (2.34) [32].

$$\mathcal{F}(P, \eta(P)) = \frac{1}{2}aP^2 + \frac{1}{4}(b - 2Q^2/K)P^4 + \frac{1}{6}cP^6 + \dots - EP \quad (2.34)$$

In the above equation,  $P$  is polarization,  $\eta$  is strain,  $E$  is electric field,  $K$  is elastic modulus based on Hooke's law,  $\sigma = K\eta$ , where  $\sigma$  is stress, and finally  $a$ ,  $b$ ,  $c$  and  $Q$  are empirically derived coefficients, describing the nature of the ferroelectric transition. The relationship of free energy as a function of polarization can take one of two forms: a paraelectric material relationship shown in Figure 2.9, and the idealized ferroelectric function shown in Figure 2.10. The response of the free energy function based on the polarization constitutes

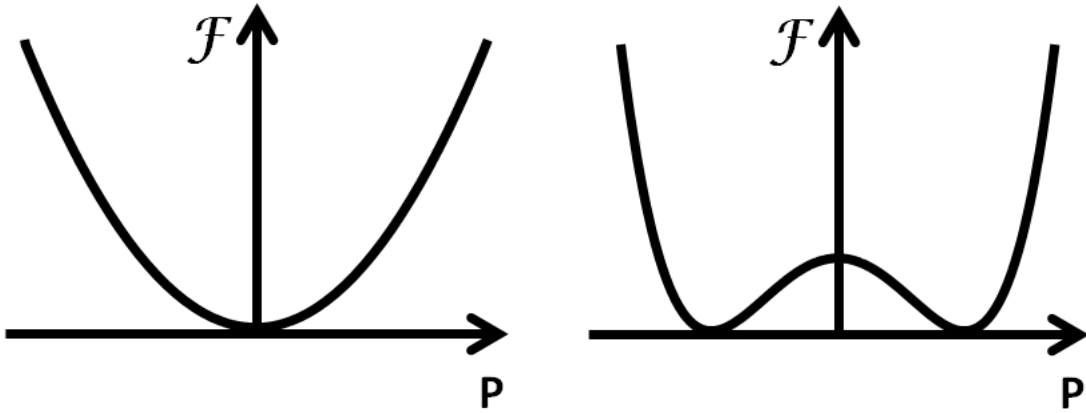


Figure 2.9: Paraelectric  $\mathcal{F}$  w/o Hysteresis      Figure 2.10: Ferroelectric  $\mathcal{F}$  w/ Hysteresis

the phenomenological behavior and describes the transition of the material based around a reference temperature,  $T_0$ . Since  $a = a_0(T - T_0)$ , the quadratic term sign is tied to the Curie temperature, where if  $a < 0$ ;  $T < T_C$ , the behavior is ferroelectric and if  $a \geq 0$ ;  $T \geq T_C$ , the behavior of the material is paraelectric as shown in Figure 2.11. Also, the contribution of the linear term, as can be seen in Figure 2.12, displays the polarization switching effects based on electric field orientation and strength. Similar effects of the coefficients  $b, c$

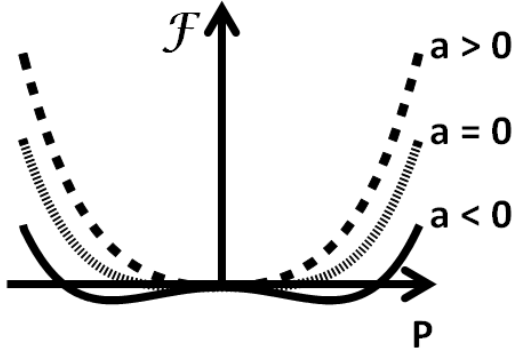


Figure 2.11: Paraelectric  $\mathcal{F}$  w/o Hysteresis

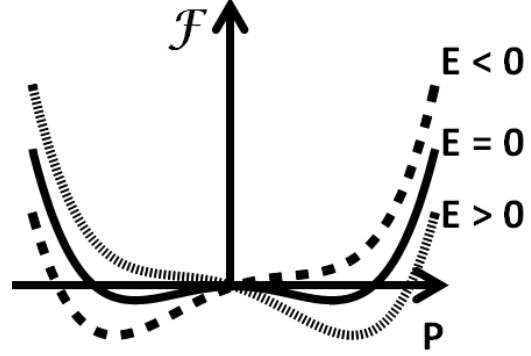


Figure 2.12: Ferroelectric  $\mathcal{F}$  w/ Hysteresis

and  $Q$  can be observed in the ferroelectric materials as the ones displayed in the previous two figures. While LD theory can accurately and mathematically describe the hysteresis relationship of the ferroelectric materials close to Curie temperature, all the coefficients, which vary greatly with different types of sublattice structures, must be derived empirically to match the magnitude of the ferroelectric response - a process which is seldom trivial. Also, while the mathematical description of the P-E hysteresis loops is accurate, the LD theory does not account for the polarization domain structure in the dielectrics, which has been attributed to the actual hysteresis behavior and will be addressed later in this section [19].

The next evolution of Landau theory, which does account for the domain structure of the ferroelectrics and allows non-uniform polarization, is the Landau - Ginzburg (LG) theory. The theory postulates that small spatial variations of polarization in the material are caused by an additional amount of free energy density,  $\Delta\mathcal{F}_{LG}$ , which is proportional to the square of the magnitude of the polarization gradient,  $|\nabla P|^2$  [32]. The lowest order of the LG free energy can be represented by the integral of the product of the polarization density  $P(r)$ ,  $\vec{r}$ , which is the  $d$ -dimensional spatial vector, and  $d^d$ , as seen in Equation (2.35).

$$F_{1st} = a_0(T - T_0) \int d^d \vec{r} [P(\vec{r})]^2 + \gamma \int d^d \vec{r} [\nabla P(\vec{r})]^2 \quad (2.35)$$

The second term in Equation (2.35) simply accounts for the variation of polarization in case the different domains are not exactly parallel. The standard Fourier transform of the LG free energy can be rewritten in Equation (2.36),

$$F = \int \frac{d^d \vec{k}}{(2\pi)^d} (a_0(T - T_0) + \gamma k^2) |P(\vec{k})|^2 \quad (2.36)$$

where  $|P(\vec{k})|^2$  is described by the polarization correlation function  $g(\vec{r})$ , as per Equation (2.37) and Equation (2.38) below [32].

$$g(\vec{r}) \sim \frac{k_B T}{\gamma} \frac{e^{-r/\xi}}{r^{d-2}}; \quad T \neq T_0 \quad (2.37)$$

$$g(\vec{r}) \sim \frac{k_B T}{\gamma} \frac{1}{r^{d-2}}; \quad T = T_0 \quad (2.38)$$

In the above three equations,  $k_B$  is the Boltzmann constant,  $\xi$  is the correlation length and the polarization correlation function can be experimentally obtained using diffuse X-ray scattering [34].

While the LG theory takes into account different polarization domains, the parameters to predict the specific ferroelectric material must also be determined experimentally. As would be expected, the LG theory begins to break down when the correlation length gets close to the smallest dimension of the domain or when the polarization correlation function becomes much smaller than the polarization strength,  $g(\vec{r}) \ll P^2$ . Finally, the LG theory can be applied to both epitaxial films and to bulk materials where polarization boundary conditions are applied in order to determine free energy in the bulk material and at the surface under different strains and external electrical field strengths. However, the most important implication of the LG theory, is that electromechanical response is likely tied to the magnitude of the polarization, suggesting that capacitance response may be bi-directional and that only the change in permittivity is important under mechanical stress, not necessarily its direction. The uniaxial response of capacitance based on bi-directional change in permittivity is a significant point, which will later help with capacitance computational predictions.

Landau theories reasonably predict the phenomenological behavior of the ferroelectric materials, but they require extensive experimental investigations for empirically derived parameters for a specific type of material to quantify its response. Most of the research that characterizes the ferroelectric hysteresis  $P - E$  loops is some derivative of the Landau theories. However, the remnant polarization and the coercive electric field responsible for the polarization switch, which are often tied to the grain structure of the material, are difficult to quantify using the Landau theory. One recent investigation by Wang et al. attempts to accurately predict the remnant polarization and coercive electric field of the PZT material using an extension of the Landau theory [35].

Just as in the Landau theory, the study by Wang assumes a sixth-degree polynomial to predict the free energy,  $G = G_0 + G_{up} + G_{down} + G_{wall}$ , but it also assumes volume fractions of the up and down polarizations of the polycrystalline structure,  $\alpha_{up}$  and  $\alpha_{down}$  respectively, where  $\alpha_{up} = 1 - \alpha_{down}$ . The free energy in the paraelectric state is  $G_0$ , and the free energy associated with the walls between the polarization domains is given by  $G_{wall}$ . However, this extension of the theory assumes that for a large polycrystalline structure the contribution of wall free energy can be omitted, and thus the resulting expression for the free energy is given by Equation (2.39) [35],

$$G = G_0 + \alpha_I P_{up}^2 + \alpha_{II} P_{up}^4 + \alpha_{III} P_{up}^6 + (1 - 2\alpha_{up})EP_{up} \quad (2.39)$$

where  $\alpha_I$ ,  $\alpha_{II}$ ,  $\alpha_{III}$  are dielectric stiffness coefficients. The average polarization  $P$ , in the hysteresis loop can be represented by  $P = (2\alpha_{up} - 1)P_{up}$ , where the volume fraction of the upward polarization is given by a relatively simple expression in Equation (2.40) [35].

$$\alpha_{up} = \frac{\arctan[\beta_1(E - E_c) + \beta_2(E - E_c)^3] + \pi/2}{\pi} \quad (2.40)$$

In Equation (2.40),  $E_c$  is the coercive field and the constants  $\beta_1$  and  $\beta_2$  are dependent on particular material grain orientation, grain size and grain boundary mechanical conditions. Again, these constants must be determined empirically, but once they are obtained, the

behavior of the  $P - E$  hysteresis of the specific type of ferroelectric material can be quantified. The resulting expression in Equation (2.40) for the ferroelectric hysteresis accurately predicts the coercive electric field and the remnant polarization using a relatively simple algebraic equation, which is a significant improvement over the original phenomenological Landau theories, but is it still applicable to only specific ferroelectric behavior. However, work by Wang suggests that the relationship between polarization, and by extension piezoelectric response to mechanical stress should be mathematically simple, which is the foreshadowing of simple nature of the capacitance response of ferroelectric ceramic components subjected to high-g drop impacts.

While discussion about the phenomenological and mathematical models can be described by some variation of the Landau theories, which can incorporate the polarization domain structure, the techniques for measuring and observing the domains and domain walls also require some attention. The techniques for observing and measuring polarization, and thus identifying the domains can be summarized in three different approaches.

The first technique, which was proven fairly recently, in the 1990s, is Scanning Probe Microscopy (SPM). SPM uses a Scanning Force Microscope (SFM) to image the domains in ferroelectric materials by swiping a sharp probe with a cantilever-type device over the surface of the material and measuring small deflections of the beam with a piezoelectric transducer [19]. The resolution that this device is capable of measuring is on the order of  $10^{-4}$  N/m. While SPM can accurately measure single crystal domains, which correlate well based on their spontaneous polarization throughout the depth of the grain, investigating polycrystalline structures is still difficult.

Another tool for measuring the polarization domains, is the grazing incidence X-ray scattering technique. The X-ray scattering technique uses spatial modulation of the polarization vector across a film surface, which creates an image with Bragg diffraction

peaks [19]. Thus, X-ray scattering is particularly useful for identifying the domains with  $180^\circ$  periodicity, and because it is possible to monitor the polarization dependence based on temperature, it is commonly used in ferroelectric materials to determine the Curie temperature,  $T_c$  [19]. As mentioned earlier in this section, X-ray scattering is also useful for determining the domain volume fraction of the polarization orientation and has been used to describe polarization switching and observe fatigue of the dielectric materials in the capacitors [36]. Finally, X-ray scattering is also useful in observing the domain wall motion in thin ferroelectric materials. While the X-ray scattering technique is well suited for describing domain and domain wall motion that can be useful in determining the ferroelectric hysteresis of thin films, a different tool is more effective at determining the domain polarization with a higher degree of accuracy.

The third, and last tool described here is Transmission Electron Microscopy (TEM), which is capable of measuring domain polarization on the order of nanometers. TEM is particularly useful in materials, which use chemical Molybdenum doping in order to accentuate the ferroelectric properties by increasing remnant polarization and coercive electric field [19]. In doped dielectric materials, polarization structure, and thus domain and domain wall structure is complex due to the presence of the added atoms in the sublattice. Hence, examining polarization orientations requires much greater resolution, which is available in TEM.

The above domain investigative techniques are useful in obtaining empirical coefficients that can be applied in quantifying the behavior of the ferroelectric materials using the Landau theories mentioned earlier. However, because domain measuring tools determine the polarization orientation only on the surface, and are thus mainly applicable to thin films, bulk material behavior is more difficult to describe using established mathematical models and therefore, a computational model approach is preferred in determining ferroelectric response through investigation of interactions of field variables affecting capaci-

tance of components. Before describing computational models, which attempt to predict ferroelectric, but more generally piezoelectric response, it is important to summarize some of the recent studies that have been performed by various government agencies and other scientific communities in order to gain an understanding of where the research is currently focused.

## **2.4 Recent Work On Component Reliability**

The dielectric materials have been studied somewhat extensively, as evidenced by the material behavior theories described earlier and by the number of methods developed to study the surface of ferroelectric ceramics. However, the electromechanical response of actual engineering components used to run circuitry, has been neglected. Unlike the surface characterizing tools, understanding electromechanical response of capacitors not only directly helps investigate the intermittent reliability problems of circuitry components, but also helps to grasp the bulk ferroelectric material behavior. Predicting changes in the bulk ferroelectric ceramics under mechanical stress would allow electronic package designers to account for variations in capacitor performance based on response of materials and help create more reliable circuitry. However, in order to apply realistic, high-g mechanical loads to capacitor models, one must first be able to understand and model stresses and strains on the printed circuit board, on which devices are mounted. From the next subsection, it is clear that printed circuit board dynamic response studies are extremely sparse for drop impacts above 3,000 g, and thus, must be first accurately modeled in order to be able to computationally expose high-g electronic components to realistic mechanical loads.

As mentioned earlier, JEDEC standards that specify bending test parameters of the printed circuit boards are available for the industry to test board-level interconnects [37]. Also, parameters such as peak acceleration and pulse duration to determine the ability of electronics subassemblies to withstand moderately severe mechanical shocks specified along with board level drop test procedures [1] have been used by scientific community



and commercial industry to standardize testing and quantify the performance of electronics packages. The conditions outlined in the JEDEC standards for board level drop tests are partly categorized based on peak acceleration applied to the component and subassemblies, and the pulse duration as measured above 10% of the peak acceleration. Unfortunately, the maximum peak acceleration characterized in these standards is capped at 2,900 g with the shortest pulse duration of 0.3 ms, which results in the total change in velocity of 5.43 m/s [38]. For most commercial applications where it is widely expected that nominal peak accelerations are on the order of 1,500 g with a pulse duration of 0.5 ms and total velocity change of 4.68 m/s, these standards provide a solid framework to test the performance of electronic circuitry. Thus, a large amount of work has been performed to characterize the behavior of surface mounted component circuit boards under the commercially relevant operating environments [39, 40]. However, the mechanical stress that is of interest in this study is at least twice the change in velocity, with peak accelerations on the order of 20,000 g, rendering most board dynamics studies inapplicable to the current work.

Perhaps the closest studies that would be relevant to the present work are experimental, as well as computational investigations of material behavior under stress, which have a chance of correlating to mechanical modes of failures of capacitors. Ball Grid Array (BGA) are among the most studied cases due to the wide use of such solder layouts in commercial electronics technology, even though the soldering technique used as part of current studies are re-flow oven soldering, which is entirely different in both structural layout and material compositions from BGA interconnects. Despite this lack of similarity, correlations between high and low loading rates to the failure modes of BGA based on various mode ratios and critical strain energy release rates showed that the pad cratering failure mode is dependent on the direction of the applied load and the stiffness of the circuit board and components [39]. Also, investigations into incorporating prognostic health monitoring and correlations between electrical resistance changes and circuit failure under tests outlined

by the JEDEC standards have also been met with some success [41]. However, most of the studies use resistors to monitor structural integrity of the interconnects and to predict intermittent loss of contact under critical strains and strain rates [40, 42]. Once again, even these studies are limited to no more than 3,700 g peak accelerations, but the progression failure of surface mounted resistors is still applicable.

The failure of resistors mounted on the board correlates very well in the laboratory with the strain of the surface on which the device is soldered as can be seen in Figure 2.13. Not only does the component fail progressively, but in terms of circuitry and current monitoring, the failure mechanisms can be classified into three stages, crack initiation, intermittent failure life and permanent failure life, as can be seen in Figure 2.14 [40]. Therefore, it should not be surprising if capacitance measurements in the current study exhibit similar failure progression, with intermittent connectivity in correlation to board strain, despite the shock being an order of magnitude higher than explored in the work by Luan.

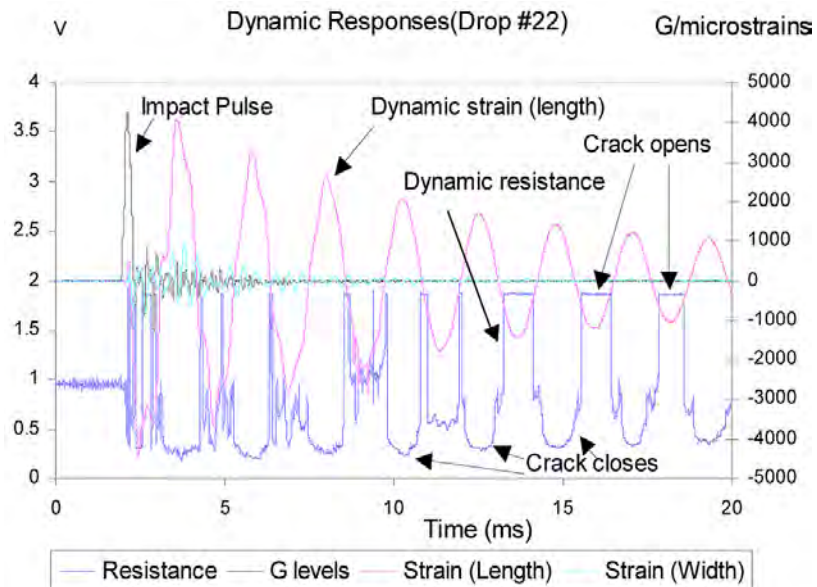


Figure 2.13: Dynamic Responses During 22<sup>nd</sup> drop. ©2006 IEEE

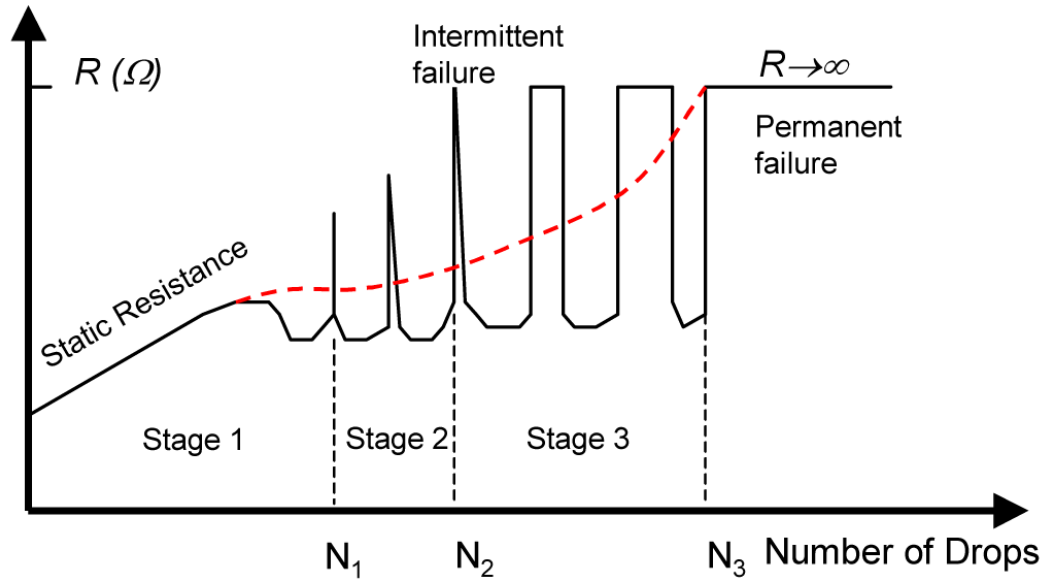


Figure 2.14: Solder Joint Failure Process. ©2006 IEEE

Performance of the PCB has also been studied under relatively low loading vibration conditions [43] as well as using monotonic bend testing methods [44] and have shown that greater component failure rate is closely related to the board geometry and the amount of board bending that exists at the pad cratering failure site. Computational work comparing the effects of elasticity modulus of solder material, board thickness and trace width show a good correlation to the component impact life under drop tests that once again cap out at the JEDEC maximum peak acceleration for subassemblies of 2,900 g [45].

From previous work, it is clear that board geometry, materials and testing conditions of drop-tests such as drop orientation, peak loads, acceleration profiles and pulse durations have a significant effect on board dynamics. These effects include strain amplitude at the surface of the board on which the components are assembled and strain response frequency, which correlates directly to strain rate. Since strain and strain rate have both been shown to correlate with and predict mechanical failure mechanisms, understanding and being able to predict, and accurately model, board dynamics under shock is of the utmost importance

before attempting to learn electromechanical response of components mounted on the PCB. Computational work validated by experimental results has been done to predict board strain using explicit finite element models with the input acceleration measured during the drop tests, and to investigate the stresses present in the BGA solder joints during the impact [40, 42]. However, the maximum peak input acceleration in this computational work was on the order of 3,700 g, which is below the scope of the current study.

It is clear that in order to investigate the modes of failure of a wide range of solder joint geometries and materials, under more extreme mechanical shocks and acceleration environments, it is critical to first have a clear understanding of the board dynamic response and to be able to predict board strain in at least a pseudo 1D case. Therefore any computational model that has a hope of exposing capacitors to realistic high-g dynamic loads must first be validated with experimental data. Thus, effects of model parameters such as the isotropic Young's Modulus, board density and contact types between the board and the drop tower fixture on the peak strain amplitude and dominant frequency of the strain must be investigated based on the measured acceleration profile and half-sine wave acceleration input matching the energy of the total velocity change. Once the computational model is validated to accurately simulate the loads to which devices are exposed under high-g drop impacts, it can be used to obtain the interconnect acceleration profiles in order to apply appropriate boundary conditions to the surface mounted components in a capacitor sub-model.

After accurately modeling mechanical stress at the precise location on the printed circuit board where the component is soldered, the acceleration profiles can be applied as boundary conditions to the capacitor sub-model itself in order to predict its electromechanical response of the dielectric materials inside capacitors. As stated earlier, dielectrics based on ceramic materials such as  $\text{BaTiO}_3$  that are now frequently used in MLCC, are also piezoelectric. However, their performance, specifically stability of permittivity in the direction

normal to the electrode plates, which directly affects capacitance under high mechanical stress and more extreme acceleration profiles than have been traditionally explored, has not been thoroughly investigated.

Recent studies conducted by the capacitor manufacturing industry suggest that capacitance primarily changes due to flex cracking of the dielectric material [25, 46, 47], called flexural mode of failure. Also, under certain static loading conditions such as ones generated by bending tests, capacitance reverts back to within 1% of its original value immediately after the stress is removed. Such behavior of components motivates the need for in-situ monitoring during highly dynamic tests in addition to pre/post-test capacitance measurements [47]. Intermittent nature of electronic components is not a new phenomenon and has recently been closely studied as it affects the reliability of BGA packages through the monitoring of resistive loads [40, 42]. However, changes in capacitance during the shock event have not yet been quantified, particularly with acceleration profiles with peak values greater than those encountered in most commercial applications. Therefore, property changes of bulk dielectric materials used inside capacitors exposed to high-g drop impact must also be investigated.

Few studies have been performed to investigate the piezoelectric behavior of raw dielectric materials such as PZT under quasi-static conditions and dynamic mass drop experiments. The voltages and currents that are generated by the piezoelectric materials have been closely related to magnitude and type of mechanical load [17]. Also, it has been discovered that stress applied to the block of PZT, where during the dynamic stress event the charge built up on the surface does not allow enough time to dissipate, leads to higher currents than during the quasi-static stress tests [18].

However, quasi-static bending tests, and especially hydrostatic compression experiments, fail to produce mechanical stress profiles similar to those experienced by components during impact. Also, exploring response of raw PZT material under carefully con-

trolled conditions, while a good starting point in understanding electronics behavior under large mechanical stresses, does not address the gap in understanding of reliability issues of capacitors employing ferroelectric dielectric materials inside real engineering components, particularly when it comes to predicting electromechanical response of capacitors before mechanical failure occurs.

While flex cracking of the capacitors, which is predominantly driven by the mechanical stress/strain response of the materials has been thoroughly studied, and the electromechanical response of some of the raw ferroelectric materials used as a dielectric inside capacitors has been sparsely characterized, the relationship between the mechanical dynamic stress conditions, indicative of high-g acceleration profiles, and capacitance of realistic engineering devices has not been even considered anywhere in the literature. Therefore, the current work investigates the electromechanical response of capacitors undergoing drop impacts on the order of 20,000 g through the use of experimentally validated computational piezoelectric FEA models, to better understand failure modes and mechanisms of electronics exposed to large dynamic mechanical stresses. However, before employing finite element codes that have been developed using theory described in Section 2.2 and verified by constitutive material models in the laboratory, software evolution should be at least addressed and the final iteration of the piezoelectric model code must be thoroughly described, which is accomplished in the following two sections.

## **2.5 Early Development of Computational Capabilities**

A fair amount of study of ferroelectric materials has been performed by government agencies interested in dielectric properties of capacitor materials as well as by agencies interested in pulsed power applications of ferroelectrics. Arguably, the greatest amount of experimental investigation of the ferroelectric materials and their response has been performed at the SNL under various mechanical, thermal and electrical loads. Specifically, the body of work performed by SNL, which measured dielectric response of the PZT 95/5

based on variations in porosity, temperature, mechanical shock and applied electric fields is the most notable. As a result of the experiments performed by SNL in the 2000s, a library of parameters and material sensitivity of ferroelectric PZT to these parameters was built in order to aid development of the computational Ferroelectric-Anti-Ferroelectric (FE-AFE) model in the ALEGRA-EMMA code.

One of the studies conducted at SNL investigated the effect of microstructural porosity of the material on the rise times in current and voltage of the mechanically shocked bulk PZT 95/5 material. This study generated shocks in the range of 2.5 GPa to 4.5 GPa and introduced spherical Polymethyl Methacrylate (PMMA) impurities ranging from 15  $\mu\text{m}$  to 140  $\mu\text{m}$  in diameter while holding the same nominal density of the bulk material at 7.30 g/cm<sup>3</sup> [13]. The results of this study showed that as long as the nominally poled bulk material remained at a constant density, the size of the spherical porous impurities had little effect on the overall current and voltage rise times of shocked materials. However, the most pronounced effect was when the impurities were on the order of 15  $\mu\text{m}$ , which was close to the average grain size of the bulk material, eluding to the fact that grain structure and size are important in predicting ferroelectric response of the dielectrics [13].

A series of different studies conducted at SNL investigated the constitutive mechanical properties of the PZT undergoing shock compression [14–16]. The studies used a gas gun to launch sapphire plates at poled and unpoled circular disks of PZT with dimensions of 4 mm in thickness and 25.4 mm in diameter, and measured the Hugoniot states as well as current rise times generated by the material while varying the initial density, external electric field and microstructure. The shock wave generated in the experiments ranged from 0.9 GPa to almost 5 GPa, while density was varied by as much as 4% by weight from the nominal density of 7.30 g/cm<sup>3</sup>. Also, by varying the resistance load on the PZT sample, the generated electrical fields ranged from 0.3 to 36.8 kV/cm. The results of the studies indicate that as long as the initial density of the material is fixed, the external electric

field and the poling state of the sample had little effect on the Hugoniot states or shock propagation through the material. However, as expected, a complex relationship emerged between the FE-AFE phase transition of the material from the unshocked to the shocked state and the strength of the initial impact. Under a lower range of pressures, the material exhibited an incomplete phase transition as characterized by higher current rise times, and lower peak currents, while under higher shocks, a slow yielding process was observed due to the brittle nature of the material [15].

The studies conducted at SNL in the 2000s quantified the electromechanical behavior of the bulk PZT 95/5 material. Measured current rise times of the shocked ferroelectric material and strength of the generated electric field under various resistive loads, the material's sensitivity to different sizes of microstructural porosity and density, as well as the mechanical response of the material based on the strength of the shock and aforementioned parameters laid the groundwork for describing the ferroelectric phenomenon. The most important outcome of these studies was an excellent empirical framework for the development and refinement of the FE-AFE model in the ALEGRA-EMMA code. It is important to note that while this groundwork provided a comprehensive set of parameters to describe the electromechanical response and generate a list of important factors to correctly describe both phenomenological and quantitative response of the PZT 95/5 to mechanical shock, these parameters will vary greatly with different ferroelectric materials. Thus, no constitutive relationships for the electromechanical response based on the shock strength or the orientation of the mechanical shock compared to the poling direction of the ferroelectric materials were developed, meaning that each ferroelectric material requiring numerical solutions in ALEGRA-EMMA would need to undergo a similar set of experimental studies in order to generate the correct material parameters. In contrast, the present work will attempt to quantify piezoelectric behavior of a ferroelectric class of materials subjected to drop impact mechanical loads representative of military application



environments, by computationally predicting the electric potential across the charging and discharging capacitors based only on a set of the already established elastic, piezoelectric and permittivity moduli, which will hopefully eliminate the need for laborious experimental investigations for every type of ferroelectric.

From the work with ferroelectric materials described above, it is clear that polarization domains, domain walls and microstructural impurities on the order of the size of the individual grains have a significant effect on the dielectric properties of such materials, and that the orientation between the poled axis of ferroelectric material and the applied mechanical stress regardless of the magnitude is extremely important to understanding the piezoelectric response of dielectrics. Furthermore, tools such as TEM, to measure the polarization domain structures at least on the surface, have recently been developed in order to aid in domain characterization and polarization orientation investigation. Finally, theoretical development of the Landau theories, as backed up by empirical studies, has shown that ferroelectric behavior transforms into a paraelectric relationship, which no longer exhibits hysteresis past the Curie temperature. Therefore, empirical investigations into the behavior of the ferroelectrics have been quite extensive, especially with the recent and increasing interest in using these materials as dielectrics inside capacitors. However, as mentioned earlier, investigations of electromechanical response of the purely piezoelectric effect, while easier to calculate using the previously developed theory in Section 2.2 due to the lack of hysteresis behavior, have been fairly sparse. Thus, it is the goal of this work to implement a computational model validated by experimental results in order to establish a constitutive relationship between piezoelectric response of ferroelectric ceramic capacitors based on applied mechanical load present during high-g drop impact.

Any phenomenological response of the purely piezoelectric behavior of ferroelectric ceramics, which are subjected to the dynamic mechanical stresses present in the circuit board containing electrical components, should produce an electromechanical response

evidenced by the change in capacitance, and thus, RC time constant for a particular capacitor. Consequently, while it is impossible to completely eliminate or significantly reduce the mechanical loading to which the circuit board is subjected inside a munition undergoing an impact, regardless of the amount of passive shock reduction techniques such as potting, it might be possible to develop the electromechanical response relationships of the electrical components, that are mounted on the PCB. Based on these relationships, minimizing the electromechanical response of capacitors inside circuitry, will reduce the negative effects of the mechanical stress and increase the overall reliability of the electrical components during impact. Hopefully, the newly developed constitutive relationships for electromechanical response to operationally representative mechanical loads based on the change in polarization and permittivity due to a purely piezoelectric response of dielectrics inside capacitors may later be extended to aid in the design of more reliable munitions electronics. Since the piezoelectric model will be used to predict capacitance changes under mechanical stress, the next section describes its theoretical basis and computational implementation to calculate the electromechanical response.

## **2.6 Piezoelectric Model in ALEGRA-EMMA**

The multi-physics and multi-material finite elements analysis software, ALEGRA-EMMA, which is currently being developed by Sandia National Laboratories solves for a quasi-static electric field approximation of the electromechanical response of various dielectric materials [22]. Because the fundamental responses of piezoelectric and ferroelectric materials are different below the Currie temperature, two separate, and perhaps the most mature models in the code are the FE-AFE Ceramic and Piezoelectric models. The FE-AFE Ceramic model provides solutions for ferroelectric materials such as PZT95/5 undergoing mechanical shocks, and uses the mathematical relationships provided in Section 2.2, as well as the parameters derived from experimental work described in Section 2.4. One particular study used the FE-AFE model to compare computationally

predicted and experimentally measured rise times in voltage and current generated by the depolarization of PZT with an explosive shock wave [48]. The Piezoelectric model, which calculates the electromechanical response of piezoelectric materials, regardless of whether or not they exhibit hysteresis behavior in the polarization versus applied electric field relationship, is a simplified derivation of the theory developed in Section 2.2 based on two, fairly accurate assumptions - every dielectric material is a perfect insulator and every conductor is a perfect conductor [21]. These two assumptions allow the implementation of a quasi-static solution to the otherwise very complex set of governing equations. Because in this work the primary concern is the response of piezoelectric materials to mechanical stress, the most applicable model for investigation of electromechanical response of capacitor dielectric materials subjected to mechanical loading inside an impacting munition is the Piezoelectric model. The fact that dielectric materials have large relative permittivities and electrodes in capacitors are made of highly conductive metals, allows the materials to reach electromechanical equilibrium on the order of picoseconds. However, because the timescales of interest of current rise times shock impact are on the order of microseconds, quasi-static electric field approximation will have minimal effect on the accuracy of the piezoelectric response calculations.

The origins of the ALEGRA-EMMA Piezoelectric model can be traced back to the 1970s, when computations using the WONDY IV code were used to model the piezoelectric response of the transversely isotropic ferroelectric ceramics [49]. Using linear constitutive relationships to relate mechanical stress  $T_{ij}$ , as well as the electric displacement  $D_i$ , in the material, to the spacial displacement  $u_i$ , and applied external electric field  $E_i$ , through the use of elastic moduli constants  $C_{ijkl}^E$ , piezoelectric constants  $e_{ijk}$ , and dielectric constants  $\epsilon_{ij}^s$ , voltage drop with various resistive loads across electrodes placed at  $x = 0$  and  $x = h_3$  was calculated for a rectangular slab of ferroelectric ceramics undergoing a time-dependent mechanical load normal to the  $x_2$  face [49]. The results of this early work

indicated that with a linear relationship between stress as well as electrical displacement, and strain and electric field, the electrical output of most normally shocked ferroelectric materials can be qualitatively described through various relationships between elastic, piezoelectric and dielectric constants. The study also noted that the boundary condition considerations are extremely important when designing experiments to investigate the piezoelectric response of ferroelectric ceramics [49], once again validating the requirement for accurate and experimentally verified board dynamics model for the PCB housing electrical components.

In the 1980s, the SUBWAY code developed by SNL further improved computational models for dielectric devices by implementing a quasi-static electric field approximation when solving the governing equations for electromechanical response [21]. The quasi-static approximation is based on neglecting the changing magnetic induction and by assuming that the electric field responds instantaneously to changes in charge distribution [21]. The two assumptions are a direct result of approximating conductors as perfect conductors, where the charge relaxation time is almost instantaneous and realizing that the electric field inside the conductor is zero, as well as by approximating all dielectric materials as insulators, where charge relaxation time is very long. With the magnetic induction neglected, Faraday's law implies that the electric field is approximated by the gradient scalar potential  $\phi$ , in Equation (2.41).

$$E_i = -\frac{\partial \phi}{\partial x_i} \quad (2.41)$$

Using the previously described Gauss' law and the relation for electric displacement in Equation (2.17) and Equation (2.19) respectively, the electric potential in a dielectric material can be expressed by Equation (2.42).

$$\frac{\partial}{\partial x_i} \left( \epsilon_{ij} \frac{\partial \phi}{\partial x_j} \right) = \frac{\partial \Pi_i}{\partial x_i} \quad (2.42)$$

Discretizing the  $I^{\text{th}}$  conductor material into a set of points  $C_I$ , in  $N$  conductors, also specifying  $V_I$  as the value of the electric potential on that conductor and applying boundary

conditions on the electric potential, where it is constant at any particular instant, as well as using Kirchhoff's laws from a simple resistive circuit, a closed form solution for the electric output could be determined in a dielectric device [21].

The current version of the Piezoelectric model, which will be used in this work is available as part of the ALEGRA suite of software developed by SNL. ALEGRA is an amalgamation of the previously developed packages such as Pronto, CTH and others, that solve the governing equations in the Lagrangian, Eulerian or Arbitrary Lagrangian-Eulerian (ALE) frames of reference using finite element discretization and referencing material libraries for closed form solutions [50]. ALEGRA-EMMA is a subset of the ALEGRA suite of software and contributes a unique electromechanics capability by also solving Maxwell's equations of electrodynamics along with constitutive relationships for the electromagnetic wave propagation in medium, in addition to the conservation of mass, momentum and energy equations. Thus, the governing equations can be summarized by Equation (2.13) through Equation (2.19). The Piezoelectric model, which is available in ALEGRA-EMMA solves the governing equations, but with the addition of two constitutive relationships of piezoelectricity [51].

In the Piezoelectric model, the two constitutive models linearly relate the strain tensor  $\{S^g\}$ , and electric field tensor  $\{\mathcal{E}^g\}$ , to the stress tensor  $\{T^g\}$ , and electric displacement tensor  $\{\mathcal{D}^g\}$ , in the material as can be seen in Equation (2.43) and Equation (2.44) respectively,

$$\{T^g\} = [C^g]\{S^g\} + [e^g]^t\{\mathcal{E}^g\} \quad (2.43)$$

$$\{\mathcal{D}^g\} = [e^g]\{S^g\} + [\mathcal{K}^g]\{\mathcal{E}^g\} \quad (2.44)$$

where the  $6 \times 6$  matrix of the elastic moduli is represented by  $[C^g]$ , piezoelectric moduli are denoted by the  $3 \times 6$  matrix  $[e^g]$ , and the  $3 \times 3$  permittivity moduli matrix is denoted by  $[\mathcal{K}^g]$  [51]. For the purposes of describing the Piezoelectric model, the symbols in cursive font such as  $\{\mathcal{E}^g\}$ , represent quantities with respect to un-deformed coordinates, while the typeset symbols such as  $E$ , represent quantities with respect to current coordinates, as

they relate according to the deformation gradient  $F$ , defined earlier in Equation (2.20). Also, superscripts ‘g’, denote values with respect to material coordinate axes, which is the coordinate system with respect to which the user inputs the properties of the material and with respect to which most of the textbook values for elastic, piezoelectric and permittivity material properties are defined. On the other hand, superscripts ‘G’, are properties defined with respect to the problem coordinate system where the calculations are performed.

In order to calculate the electromechanical response of piezoelectric materials, the process is broken down into two separate phases. In the first, the setup phase, the elastic  $[C^g]$  and piezoelectric  $[e^g]$  moduli that are provided by the user for the particular material are transformed into Voight-Mandel representations  $[\tilde{C}^g]$  and  $[\tilde{e}^g]$ , using the Equation (2.45) and Equation (2.46) below [51].

$$[\tilde{C}^g] = \begin{bmatrix} [C_{nn}^g] & \sqrt{2}[C_{ns}^g] \\ \sqrt{2}[C_{ns}^g] & 2[C_{ss}^g] \end{bmatrix} \quad (2.45)$$

$$[\tilde{e}^g] = \begin{bmatrix} e_{111}^g & e_{122}^g & e_{133}^g & \sqrt{2}e_{123}^g & \sqrt{2}e_{113}^g & \sqrt{2}e_{112}^g \\ e_{211}^g & e_{222}^g & e_{233}^g & \sqrt{2}e_{223}^g & \sqrt{2}e_{213}^g & \sqrt{2}e_{212}^g \\ e_{311}^g & e_{322}^g & e_{333}^g & \sqrt{2}e_{323}^g & \sqrt{2}e_{313}^g & \sqrt{2}e_{312}^g \end{bmatrix} \quad (2.46)$$

The elastic  $[\tilde{C}^g]$ , piezoelectric  $[\tilde{e}^g]$ , and permittivity  $[\mathcal{K}^g]$  moduli are then transformed into global problem coordinates elastic  $[\tilde{C}^G]$ , piezoelectric  $[\tilde{e}^G]$ , and permittivity  $[\mathcal{K}^G]$  moduli, using the Voight-Mandel orthogonal rotation matrices [51]. The final step of the setup phase is transforming the global Voight-Mandel representations of the elastic  $[\tilde{C}^G]$ , and piezoelectric  $[\tilde{e}^G]$  moduli into the global representations using Equation (2.47) and Equation (2.48) below [51].

$$[C^G] = \frac{1}{2} \begin{bmatrix} 2[\tilde{C}_{nn}^G] & \sqrt{2}[\tilde{C}_{ns}^G] \\ \sqrt{2}[\tilde{C}_{ns}^G] & [\tilde{C}_{ss}^G] \end{bmatrix} \quad (2.47)$$

$$[e^G] = \frac{1}{\sqrt{2}} \begin{bmatrix} \sqrt{2}\tilde{e}_{111}^G & \sqrt{2}\tilde{e}_{122}^G & \sqrt{2}\tilde{e}_{133}^G & \tilde{e}_{123}^G & \tilde{e}_{113}^G & \tilde{e}_{112}^G \\ \sqrt{2}\tilde{e}_{211}^G & \sqrt{2}\tilde{e}_{222}^G & \sqrt{2}\tilde{e}_{233}^G & \tilde{e}_{223}^G & \tilde{e}_{213}^G & \tilde{e}_{212}^G \\ \sqrt{2}\tilde{e}_{311}^G & \sqrt{2}\tilde{e}_{322}^G & \sqrt{2}\tilde{e}_{333}^G & \tilde{e}_{323}^G & \tilde{e}_{313}^G & \tilde{e}_{312}^G \end{bmatrix} \quad (2.48)$$

In order to specify the orientation of the polarization angle  $\theta$ , or in other words the polarization domain orientation discussed in Section 2.4, an input parameter  $[a^{sG}]$ , in Equation (2.49) is specified, which establishes the direction cosine matrix of the material moduli with respect to the problem coordinates [51].

$$[a^{sG}] = \begin{bmatrix} 1 & 0 & 0 \\ 0 & \cos(\theta) & -\sin(\theta) \\ 0 & \sin(\theta) & \cos(\theta) \end{bmatrix} \quad (2.49)$$

The second phase in predicting the piezoelectric response is a series of calculations, which update with every time step based on the elastic, piezoelectric and permittivity moduli, the rotation matrix, and the deformation gradient. In order to calculate the un-rotated Cauchy stress tensor,  $\sigma^u = R^t \sigma R$ , the spatial mechanical polarization  $\pi^G$ , and the spatial permittivity tensor  $K^G$ , the spatial electric field  $E^G$ , and the polar decompositions  $V$  and  $R$ , of the deformation gradient  $F = VR$ , are also required at each time step [51]. First, the electric field components  $E_{IJ}$ , are calculated using  $E_{IJ} = 1/2(F^t F - 1)$ , and then the strain  $\{S^G\}$ , is calculated using the expression in Equation (2.50) [51].

$$\{S^G\} = \begin{Bmatrix} S_1 \\ S_2 \\ S_3 \\ S_4 \\ S_5 \\ S_6 \end{Bmatrix} = \begin{Bmatrix} E_{11} \\ E_{22} \\ E_{33} \\ 2E_{23} \\ 2E_{13} \\ 2E_{12} \end{Bmatrix} \quad (2.50)$$

The electric field  $E^G$ , which is in terms of the current coordinates is then represented in the un-deformed coordinates using  $\{\mathcal{E}^G\} = [F^t]\{E^G\}$ , so that the 2<sup>nd</sup> Piola Kirchhoff stress

tensor  $\{T^G\}$ , in the global coordinates can be calculated according to Equation (2.43) [51]. The Cauchy stress tensor is calculated using the proper operators  $F$ , and  $T^G$ , of the deformation gradient  $[F]$ , and the 2<sup>nd</sup> Piola Kirchhoff stress tensor  $\{T^G\}$ , respectively through the expression  $\sigma = (1/J)FT^GF^t$ , where  $J$  is the determinant of  $[F]$  [51]. At this point all the quantities are known and the next iteration of the mechanical polarization, de-rotated Cauchy stress tensor and permittivity moduli are evaluated in Equation (2.51), Equation (2.52) and Equation (2.53) respectively.

$$\{\pi^G\} = \frac{1}{J}[F][e^G]\{S^G\} \quad (2.51)$$

$$\sigma'' = R^t \sigma R \quad (2.52)$$

$$[K^G] = \frac{1}{J}[F]\{\mathcal{K}^G\}[F^t] \quad (2.53)$$

It is clear that information on elastic, piezoelectric and permittivity moduli along with the rotation matrix specifications of the particular material is required in order to calculate the piezoelectric response. While these moduli for specific materials are extremely sensitive to the exact chemical composition of ferroelectric ceramics as well as to the accuracy of the specific measurement techniques, the nominal parameters for the elastic, piezoelectric and permittivity moduli have been previously published for materials such as polarized, transversely isotropic Barium Titanate [52] and certain compositions of PZT [11, 27, 53]. Thus, it is possible to computationally investigate the quantitative response of piezoelectric materials based on the correct structural layout of dielectric specimens inside capacitors and varying mechanical loads using the Piezoelectric model in ALEGRA-EMMA.

## 2.7 Purpose of the Present Research

As previously mentioned in this chapter, ferroelectric ceramics have recently been extensively used as dielectric insulating materials inside capacitors in aerospace circuitry technology. Particularly, capacitors have been implemented as detonators of explosives



inside hard target weapons and also as elements of DC circuitry inside a munition fuze. The mechanical loading that the weapons undergo when impacting a target create an environment which has been poorly understood and seldom researched, due to its uniqueness. Thus, to this date, little research has been done to investigate the purely piezoelectric response of ferroelectric materials to describe their electromechanical behavior when subjected to mechanical stresses present in impacting munitions.

Most of the current experimental research into the behavior of ferroelectric materials has been focused on the material response to explosive mechanical shocks, which produce high pressures and particle velocities at the material's speed of sound, in order to investigate the ferroelectric to anti-ferroelectric phase transition when generating pulsed power. Even material specific computational models to predict this ferroelectric to anti-ferroelectric transition have also been developed by SNL. Also, mathematical models and theories of the ferroelectric material response, such as the Landau theories, have been developed to help phenomenologically describe the material polarization in response to applied external field and quantify the hysteresis effect of ferroelectric ceramics. Finally, an extensive amount of research has been done to look at the behavior of thin films of piezoelectric materials specific for their transducer applications.

While almost no effort has been expended to study the response of the bulk material inside capacitors subjected to mechanical impact loading representative of the environment inside the impacting munitions, all the previous work described in this chapter points to the fact that purely piezoelectric response to applied mechanical load is of the utmost importance when examining the capacitance changes of components that use ferroelectric ceramics as their dielectric. With the development of the piezoelectric computational model, it is now possible to closely investigate piezoelectric capacitance response of the dielectric materials, and more specifically ferroelectric materials inside capacitors subjected to different types and magnitudes of mechanical stresses. In particular, using

the Piezoelectric model in ALEGRA-EMMA described in Section 2.6, it is possible to predict the purely piezoelectric, electromechanical, response of ferroelectric ceramics, such as Barium Titanate, as long as the nominal elastic, piezoelectric and permittivity moduli are specified. Thus, the research objectives of this present work comprise the following:

1. Using the drop tower, realistically recreate the mechanical loading environment to which circuitry inside an impacting munition is subjected, measure the impact acceleration and one-dimensional strain on the PCB surface to which electronic components are soldered, and create a solid dynamics model in ALEGRA-EMMA, which accurately simulates the measured stress environment at locations on the board where the capacitors are mounted.

2. After dynamic board response is quantified in the first objective, experimentally measure capacitance response of capacitors subjected to the same mechanical drop shocks to detect and describe possible mechanical and electromechanical modes of failure.

3. Create a computational finite element model of the capacitor subjected to the same stresses identified in objective 1 in order to determine if purely piezoelectric response can emulate and predict the same capacitance changes measured experimentally during completion of objective 2.

The overall goal of the present research is to contribute to the body of knowledge of electromechanical response of ferroelectric materials used as dielectric insulators inside capacitors subjected to a unique set of mechanical loads by computationally modeling the capacitance response of components shocked in the laboratory using the drop tower. It is hoped that as a result of the knowledge gained from this present work, more reliable aerospace circuitry technology can be developed in the future by ensuring that capacitors are designed to address the dominant mechanical and electromechanical modes of failure, and to withstand high-g dynamic stresses with greater reliability and predictability.

### III. Methodology

As mentioned in the previous chapter, the munitions impacting hard targets undergo high-g shocks where the circuit boards packaged inside fuzes and housing capacitors are exposed to acceleration profiles with peaks on the order of 20,000 g. However, prior to exploring the electromechanical response of the dielectric materials inside capacitors, a computational model of the PCB has to be validated against the experimentally obtained dynamic response of the board subjected to high-g drop tower tests. Therefore, board strain oscillation frequency and amplitude calculations by the PCB computational model must first closely match the same parameters measured in the laboratory under similar drop impact conditions. Once the computational board dynamics closely correlate to the experimental strain measurements, calculated acceleration boundary conditions at the locations where the capacitors are soldered are applied to the sub-model of the capacitor in order to compute the electromechanical response. Finally, the results from the capacitor sub-model must be validated by the experimentally measured capacitance changes under the same impacts.

Thus, in this chapter, the methodology for reaching the objectives outlined in Chapter 2 are described in detail. First, the experimental procedures used to obtain the dynamic response of the PCB material representative of the circuit board inside munitions are described. Then, experimental set-up and techniques for measuring capacitance of devices undergoing drop tests are explained. Later, procedures for sample preparation, SEM characterization of the dielectric material and mapping of electrode layout structure are outlined. Finally, the computational ALEGRA-EMMA models used to simulate shocked board dynamics and the electromechanical capacitance response of capacitors, as well as their solid dynamics and electromechanics input parameters are specified.

### 3.1 Experimental Set-Up for Measuring PCB Dynamic Response

In order to simulate high-g stress environments in the laboratory, a 10 ft MTS drop tower located at the Munitions Directorate of the Air Force Research Laboratory (AFRL) on Eglin Air Force Base (AFB) was used as part of the experiment to gather the acceleration and board strain data for validating the computational board dynamics model. A felt programmer of 1/8 inch thickness was inserted between the steel seismic mass resting on the shock absorber and the aluminum anvil, assisted by the bungee cord, as shown in Figure 3.1, in order to help shape the acceleration profile. The acceleration profile shaping felt programmer was progressively more compacted with every drop of the anvil, making it absolutely necessary to gather accelerometer data during every drop regardless of whether or not the drop height was changed. Therefore, a 4340 stainless steel fixture, which was bolted to the anvil, contained a single Endevco 7270A-60K accelerometer for measuring the acceleration in the single, z-direction, during every impact.

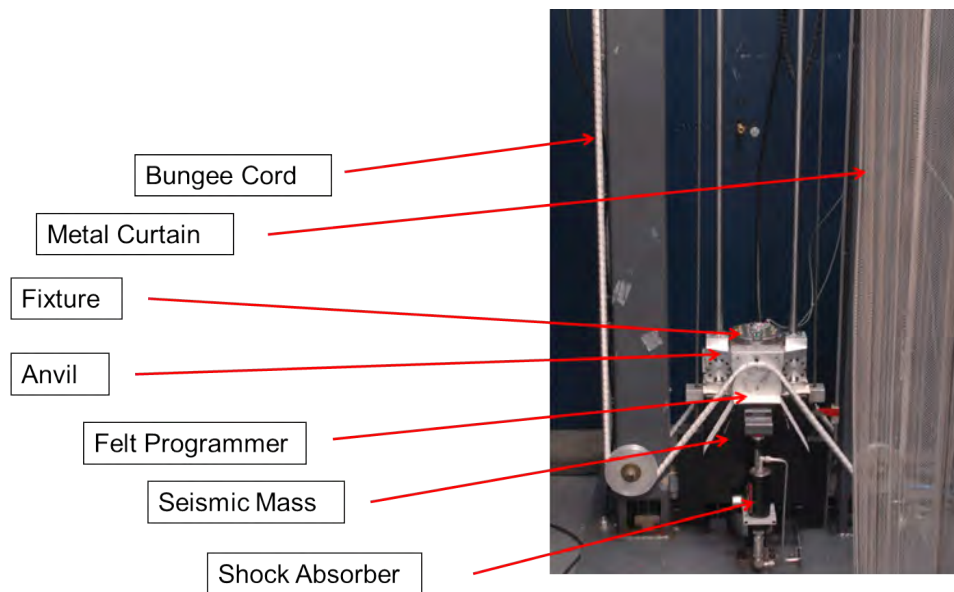


Figure 3.1: 10 ft MTS Drop Tower

The PCB chosen for this study was an ISOLA 370HR rectangular circuit board test specimen with dimensions  $60.325 \text{ mm} \times 19.05 \text{ mm} \times 1.524 \text{ mm}$  clamped to the fixture using stainless steel clamps and screws as shown in Figure 3.2. The rectangular shape of the printed circuit board in the clamped configuration exposes the surface of the PCB to an overwhelmingly uniaxial surface strain in the x-direction after the impact. The pseudo one-dimensional strain profile simplifies the boundary conditions needed to study the electromechanical response of the capacitors and allows for easier implementation of the capacitor sub-model input parameters. Finally, the circuit board itself was fitted with a Vishay C2A-06-062LW-120 strain gage on the top surface to measure the lengthwise, x-direction, uniaxial strain response of the board during impact.

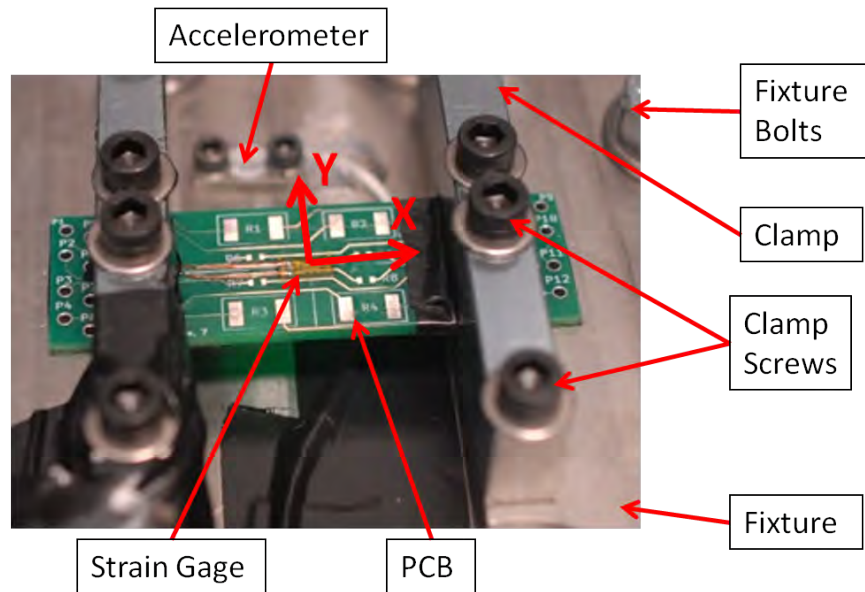


Figure 3.2: ISOLA 370HR Board Specimen Test Set-Up

During the experiment, the uniaxial surface strain profile of the board gathered by the strain gage and the acceleration profile gathered by the accelerometer mounted on the

fixture, were collected at a data rate of 1 MHz over a 0.1 second duration using the Precision Filter Inc. model 28000 signal conditioning system.

The mass of the fixture, clamps and unpopulated circuit board was measured and the density of the board specimen was obtained by dividing the average mass of five boards by the calculated volume from the above dimensions resulting in the lower approximation of the board's average density of  $\rho = 1904 \text{ kg/m}^3$ . Taking into account the four holes through which the screws clamped the board to the fixture, as well as the 16 holes for connecting the wires used to monitor resistor connectivity, the upper end approximation of the density of the board was calculated to be  $\rho = 2090 \text{ kg/m}^3$ . The different acceleration profiles and calculated density properties were used for the parametric study in the computational model to quantify the sensitivity of each parameter to the oscillation frequency and strain amplitude response of the board after impact.

### **3.2 Experimental Set-Up for Measuring Capacitance Response to Drop Impact**

As mentioned earlier in Chapter 2, capacitance can be determined by applying a square wave charge/discharge pulse to a capacitor through a constant resistance resistor and measuring the voltage across the capacitor. Therefore, the next two subsections illustrate the experimental set-up and procedures for measuring capacitance changes during and immediately after the drop shock event, which will later be used to validate the computational sub-model of electromechanical capacitance response of high and low voltage capacitors.

#### ***3.2.1 High Voltage Capacitance Measurements.***

The high voltage ferroelectric dielectric capacitors chosen for this study were AVX Corporation Class II MLCC based on Barium Titanate ceramic dielectric with X7R temperature profiles. The X7R characteristic implies relatively low variance of capacitance with temperature, even though external temperature was not varied during the experiment, and thus, was not a factor in the variations in capacitance. The high voltage floating

electrode capacitors, shown in Figure 2.2, were rated to 3,000 VDC and 470 pF  $\pm$ 10% in capacitance. The nominal size of devices was 4.5 mm  $\times$  3.2 mm  $\times$  1.54 mm (size 1812) with each component weighing 0.12 grams.

The board electrical layout supported up to four 1812 size high-voltage capacitors surface mounted symmetrically about the center of the PCB. The top surface of masked copper stations C5, C6, C7 and C8 allowed up to four connections per station, as seen in Figure 3.3. Capacitors were surface mounted on the PCB with the Exmore VS-500

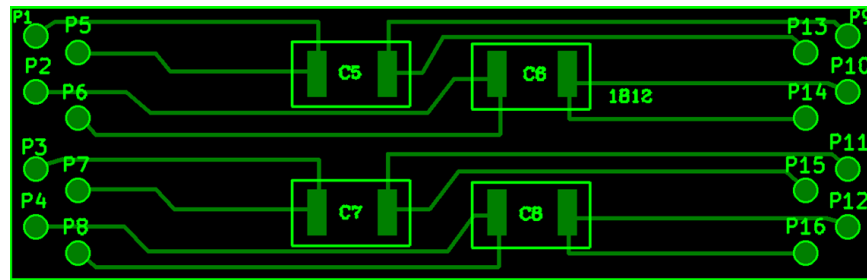


Figure 3.3: Printed Circuit Board Electrical Layout

Vapor Soldering re-flow oven, shown in Figure 3.4, according to AVX surface mounting guide temperature profile [54] using the Sn63Pb37 Kester Manufacturer solder paste. The solder paste was applied to the PCB copper pads by the Mann Corp SP5500 Dual Squeegee Stencil Pencil, shown in Figure 3.5.

Once the boards were populated with capacitors, drop impact tests commenced using the same drop tower employed during PCB dynamics investigations described in Section 3.1. Initial mechanical shock impulse duration during each run was on the order of 100 - 250  $\mu$ s with peak acceleration amplitudes ranging between 500 - 24,000 g depending on the drop height. The charge/discharge square pulse was generated by waveform generators at a frequency of 100 KHz during the drop resulting in approximately 10 - 25 capacitance measurements throughout the duration of the initial shock impulse.

Capacitance was later calculated using least squares fit of an exponential function to the voltage versus time curve using the relationships described in Equation (2.9) and Equation (2.10).



Figure 3.4: Exmore VS-5000 Vapor Soldering Re-flow Oven

The master square wave charge/discharge signal was provided by the Standard Research Systems DS345 Synthesized Function Generator using a 5 VDC peak to peak pulse with zero offset. The pulse was routed through the off-board, unstressed, capacitor via the shorted C8 station on the PCB and a  $464\ \Omega$  resistor in order to compare the changes in capacitance between stressed and unstressed components. The slave charge/discharge signal was supplied through a separate  $464\ \Omega$  resistor by the Agilent 33220A Arbitrary Waveform Generator using the 5 VDC peak to peak square wave through the stressed capacitor mounted on station C5. TDSK5104B Digital Phosphor Oscilloscope was used to monitor and record voltage across the stressed capacitor on Channel 3 and unstressed capacitor on Channel 4. The original slave and master square pulses were simultaneously



monitored on Channels 1 and 2 respectively. All channels were set to the high impedance value of  $1\text{ M}\Omega$  in order to accommodate the oscilloscope's maximum possible root mean square limits, while simultaneously stressing the capacitors with the highest possible potential during the drop impacts.

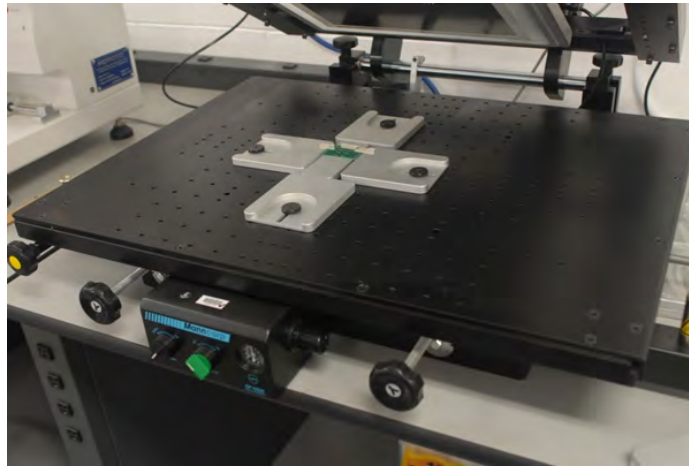


Figure 3.5: SP5500 Dual Squeegee Stencil Pencil

Voltage across the mechanically stressed capacitor was measured and recorded to observe the direct effects of the mechanical shock on the capacitance, while voltage across unstressed, off-board, capacitor was measured for comparison in order to detect any capacitance changes due to cable whip, and inherent capacitance in the cabling and the board. The slave and master pulse generators were synchronized, and the square wave pulses were routed through the same 20 feet of commercial grade general purpose 22 AWG 4 conductor plenum shielded cable. The stressed capacitor on C5 station was connected using +red, -black convention and the short on C8 PCB station with off-board capacitor used +green, -white coding. For certain drops, a Vishay foil strain gage was fixed to the bottom surface of the PCB to measure the lengthwise (x-direction) uniaxial strain response of the board during the impact in order to quantify the board dynamics.

However, all the experimental runs used an Endevco 7270A-60K accelerometer mounted directly on the fixture to measure impact acceleration in the vertical direction (z-direction). The accelerometer signal was routed through the Auxiliary channel on the oscilloscope to trigger recording of capacitance data on all four channels with a 15% delay, as soon as the accelerometer voltage reached a preset value of 140mV, equivalent to 280 g. National Instruments Chassis supplied constant current for the strain gage and constant voltage for the accelerometer with Precision Filters 28000 providing initial signal processing as part of the impact data acquisition system. The wiring schematic for the strain, acceleration and capacitance data acquisition system is shown in Figure 3.6.

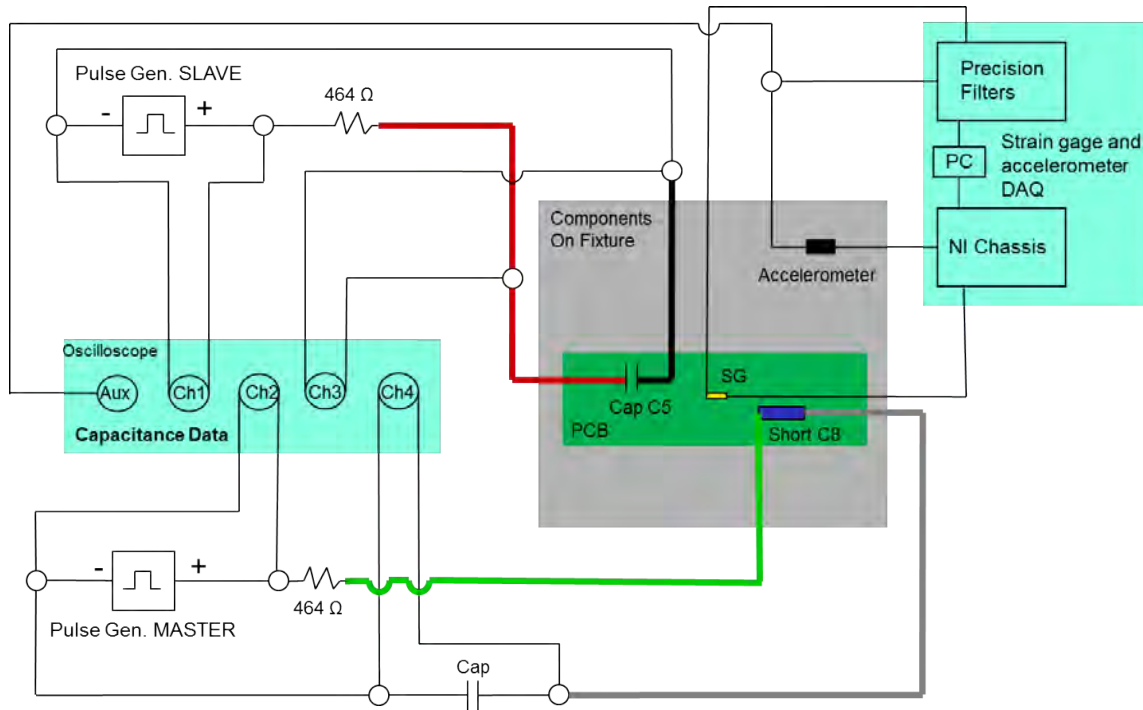


Figure 3.6: Data Acquisition Schematic

Acceleration and strain data were recorded at a sample rate of 25 MS/s (25 MHz) for a total duration of 100 ms, while the voltage across both stressed and unstressed capacitors, as well as the original slave and master signals was collected at a sample

rate of 50 MS/s (50 MHz) for a total duration of 10 ms. With the 100 KHz wave pulse frequency, approximately 250 voltage data points were available for the least squares fit to an exponential function in order to determine the RC time constant using Matlab. However, for more accurate least squares fit calculations, only voltages within 12% of peak values were used for curve fitting.

Drop tests were carried out from twelve distinct drop heights using three different PCB mounting configurations for a total of 60 impacts. The drop heights ranged from 6 inches to 72 inches, equivalent to 2.2 m/s and 12.8 m/s change in velocity, or peak acceleration amplitudes varying from 666 g to 23,961 g respectively. Printed circuit boards were assembled and affixed to the fixture using three different configurations. In Configuration A1, shown in Figure 3.7, PCB was caul clamped, allowing the board to flex after impact with capacitors mounted on stations C5, C6 and C7. Capacitance was monitored on station C5 and a short was soldered on C8 station for off-board capacitance measurements. Configuration A2, shown in Figure 3.8, utilized steel clamps, and thus dynamic capacitance was not monitored in real time, but featured capacitors on all four stations. Configuration B was an identical electrical setup as configuration A1, but the mechanical mounting scheme was modified with the board being affixed directly on the flat steel surface of the fixture preventing the board from flexing post impact, as seen in Figure 3.9. Unlike the acceleration profiles, strain data, capacitance measurements and high speed video were not all collected during each drop. Therefore, test matrix in Table 3.1 correlates the drop configuration, drop height and the corresponding change in velocity, as integrated using the trapezoidal rule, with the collected data. As discussed earlier, accelerometer data was required for every drop in order to quantify the acceleration profile, however, during drops 3 and 9, acceleration data was not recorded, and thus these tests are not included in the analysis, or the matrix.

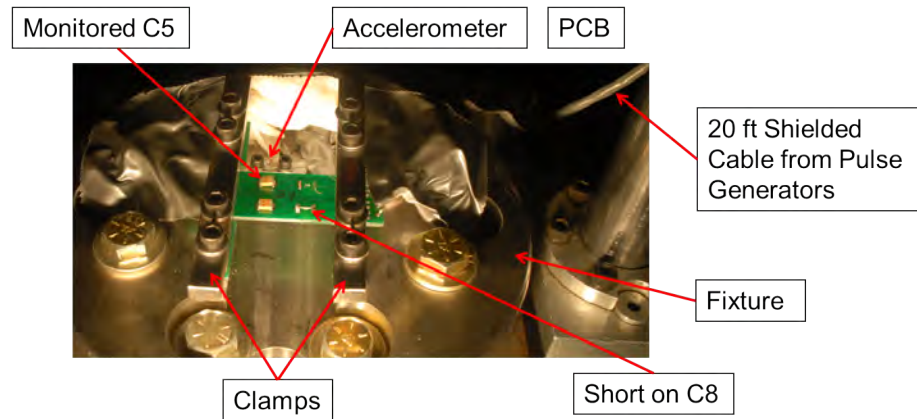


Figure 3.7: Flexing Board Configuration A1 w/ Caul Clamps

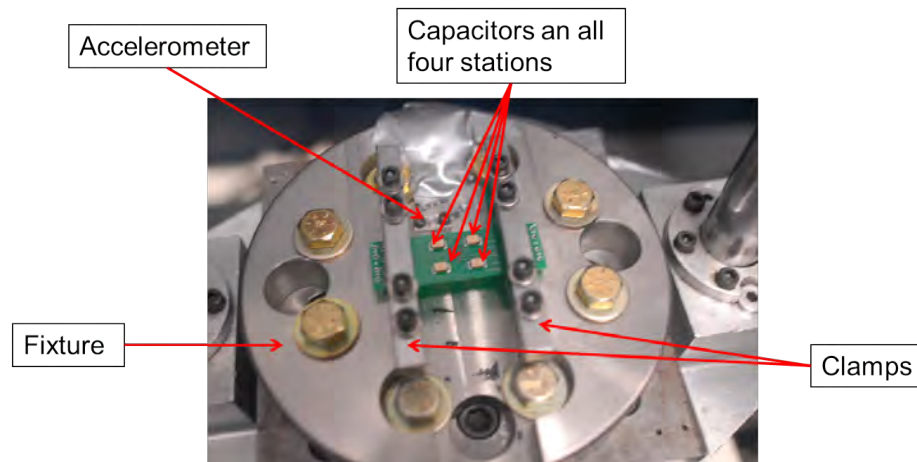


Figure 3.8: Flexing Board Configuration A2 w/ Steel Clamps

Table 3.1: High Voltage Capacitance Test Matrix (X indicates data collected)

| Test #                 | Configuration | Height (in) | dV (m/s) | Strain | Capacitance |
|------------------------|---------------|-------------|----------|--------|-------------|
| 1                      | —             | 12          | 3.934    | X      | —           |
| 2                      | —             | 18          | 4.517    | X      | —           |
| 4                      | —             | 24          | 2.886    | X      | —           |
| 5                      | —             | 30          | 5.587    | X      | —           |
| 6                      | —             | 36          | 6.202    | X      | —           |
| Continued on next page |               |             |          |        |             |

Table 3.1 – continued from previous page

| Test # | Configuration | Height (in) | dV (m/s) | Strain | Capacitance |
|--------|---------------|-------------|----------|--------|-------------|
| 7      | –             | 36          | 6.074    | X      | –           |
| 8      | –             | 36          | 4.857    | X      | –           |
| 10     | A2            | 17.25       | 4.762    | –      | –           |
| 11     | A2            | 23.25       | 5.877    | –      | –           |
| 12     | A2            | 29.25       | 4.731    | –      | –           |
| 13     | A2            | 35.25       | 6.177    | –      | –           |
| 14     | A2            | 42.25       | 7.636    | –      | –           |
| 15     | A1            | 18          | 3.336    | –      | X           |
| 16     | A1            | 36          | 6.082    | –      | X           |
| 17     | A1            | 36          | 6.141    | –      | X           |
| 18     | A1            | 36          | 6.271    | –      | X           |
| 19     | A1            | 36          | 6.803    | –      | X           |
| 20     | A1            | 36          | 5.966    | –      | X           |
| 21     | A1            | 36          | 6.307    | –      | X           |
| 22     | A1            | 36          | 6.382    | –      | X           |
| 23     | A1            | 36          | 6.942    | –      | X           |
| 24     | A1            | 36          | 6.382    | –      | X           |
| 25     | A1            | 36          | 7.758    | –      | –           |
| 26     | A1            | 36          | 7.955    | –      | –           |
| 27     | A1            | 12          | 2.307    | X      | X           |
| 28     | A1            | 36          | 6.782    | X      | X           |
| 29     | A1            | 36          | 5.847    | X      | X           |
| 30     | A1            | 36          | 5.912    | X      | X           |
| 31     | A1            | 36          | 7.404    | X      | X           |
| 32     | A1            | 36          | 6.134    | X      | X           |
| 33     | A1            | 36          | 7.505    | –      | X           |
| 34     | A1            | 36          | 7.234    | –      | X           |
| 35     | A1            | 36          | 7.676    | –      | X           |
| 36     | A1            | 36          | 5.878    | –      | X           |
| 37     | B             | 18          | 2.887    | –      | X           |
| 38     | B             | 24          | 3.493    | –      | X           |
| 39     | B             | 30          | 6.046    | –      | X           |
| 40     | B             | 36          | 5.651    | –      | X           |
| 41     | B             | 42          | 8.416    | –      | X           |
| 42     | B             | 48          | 8.536    | –      | X           |
| 43     | B             | 48          | 7.247    | –      | X           |
| 44     | A2            | 36          | 8.638    | –      | –           |
| 45     | A2            | 30          | 5.547    | –      | –           |
| 46     | A2            | 24          | 5.499    | –      | –           |
| 47     | A2            | 18          | 4.468    | –      | –           |
| 48     | A2            | 12          | 2.699    | –      | –           |

Continued on next page

Table 3.1 – continued from previous page

| Test # | Configuration | Height (in) | dV (m/s) | Strain | Capacitance |
|--------|---------------|-------------|----------|--------|-------------|
| 49     | A2            | 6           | 2.162    | –      | –           |
| 50     | A2            | 6           | 2.182    | –      | –           |
| 51     | A2            | 12          | 3.716    | –      | –           |
| 52     | A2            | 18          | 5.204    | –      | –           |
| 53     | A2            | 24          | 6.180    | –      | –           |
| 54     | A2            | 30          | 5.998    | –      | –           |
| 55     | A2            | 36          | 7.429    | –      | –           |
| 56     | B             | 54          | 10.027   | –      | X           |
| 57     | B             | 60          | 11.392   | –      | X           |
| 58     | B             | 66          | 11.283   | –      | X           |
| 59     | B             | 72          | 12.850   | –      | X           |
| 60     | B             | 72          | 12.797   | –      | X           |

### 3.2.2 Low Voltage Capacitance Measurements.

The low voltage component capacitance was measured using similar methodology employed to experimentally investigate capacitance response of the high voltage capacitors. However, due to differences in physical size of components and their electrical properties, especially the capacitance value, modifications to experimental parameters had to be made, in order to collect electromechanical response at the highest possible data rate, and ensure sufficiently high information resolution to fully observe the capacitance change effects during impact. This section describes the differences in techniques that were necessary as a result of changes in capacitor performance parameters.

The low voltage ferroelectric dielectric capacitors were also Class II MLCC based on Barium Titanate ceramic dielectric with X7R temperature profiles manufactured by the AVX Corporation. However, the low voltage floating electrode capacitors, shown in Figure 2.2, were rated to 10 VDC and 2,200 pF +/-20% in capacitance. The nominal size of devices reduced to 3.2 mm × 2.5 mm × 0.8 mm (size 1210) and due to the smaller dimensions of the surface mounted components, PCB layout also changed slightly by moving copper pads closer together to accommodate the new devices. However, the

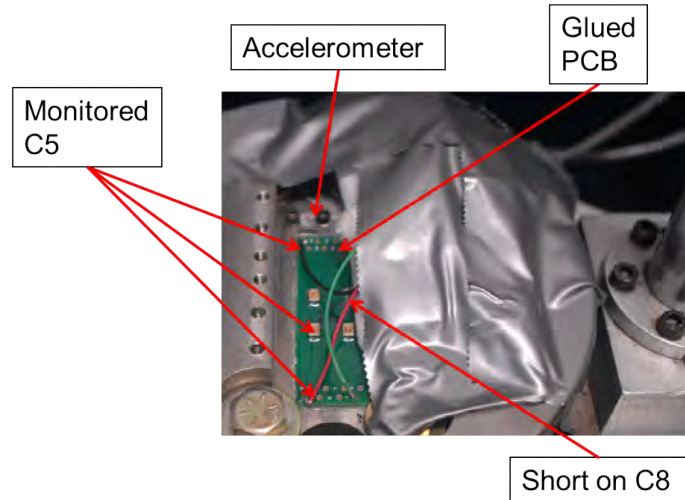


Figure 3.9: Non-flexing Board Configuration B

electrical layout of traces remained unchanged from the board housing the 3,000 VDC capacitors.

Due to the more than quadrupling of the capacitance value from 470 pF to 2,200 pF, which increased the RC time constant by over four times, reducing the resistance value by the same amount would have been ideal in order to maintain the same charge/discharge pulse frequency as for the high voltage capacitors. However, electrical feedback problems with the function generators required an even higher impedance in the RC circuit, and thus the resistor value was increased to 1 K $\Omega$ . The combined ten-fold increase in the RC time constant required a reduction in pulse frequency to 50 KHz, which ensured enough charging/discharging time to accurately estimate the capacitance using the least squares fit in Matlab and that the pulse occurred frequently enough to accurately capture capacitance response during the short period of the shock event.

Also, in order to avoid polarization switching, during the charge/discharge cycle, the 10 VDC capacitors were exposed to the +/- 4 VDC amplitude pulse, offset by +5 VDC. Thus, the voltage varied between +1 and +9 VDC for the low voltage

capacitor measurements, exercising the capacitor through 80% of its rated value. However, the fundamental data acquisition technique for the acceleration, strain and capacitance remained the same, as shown in Figure 3.6.

The board test configurations for the low voltage capacitors were identical to the high voltage device experiments, but only configurations A1 and B, shown respectively in Figure 3.7 and Figure 3.9, were used for the 10 VDC capacitors. Unfortunately, toward the end of the drop tower experiments the insulation around the accelerometer wire wore off, feeding partially erroneous data. Thus, the low voltage capacitance measurement test matrix in Table 3.2 includes the column indicating if the accelerometer data was collected. Only 43 drops of the 10 VDC devices were accomplished and the 12 inch height impacts did not always produce enough acceleration to trigger the data acquisition system, explaining the more sporadic acquisition of accelerometer and capacitance data in Table 3.2.

Table 3.2: Low Voltage Capacitance Test Matrix (X indicates data collected)

| Test #                 | Configuration | Height (in) | Acceleration | Strain | Capacitance |
|------------------------|---------------|-------------|--------------|--------|-------------|
| 1                      | —             | 36          | X            | X      | —           |
| 2                      | —             | 30          | X            | X      | —           |
| 3                      | —             | 24          | X            | X      | —           |
| 4                      | —             | 18          | X            | X      | —           |
| 5                      | —             | 12          | X            | X      | —           |
| 6                      | —             | 12          | X            | X      | —           |
| 7                      | —             | 18          | X            | X      | —           |
| 8                      | —             | 24          | X            | X      | —           |
| 9                      | —             | 30          | X            | X      | —           |
| 10                     | —             | 36          | X            | X      | —           |
| 11                     | —             | 42          | X            | X      | —           |
| 12                     | —             | 48          | X            | X      | —           |
| 13                     | —             | 54          | X            | X      | —           |
| 14                     | —             | 60          | X            | X      | —           |
| 15                     | A1            | 12          | —            | —      | —           |
| 16                     | A1            | 18          | X            | —      | X           |
| 17                     | A1            | 24          | X            | —      | X           |
| 18                     | A1            | 30          | X            | —      | X           |
| 19                     | A1            | 36          | X            | —      | X           |
| Continued on next page |               |             |              |        |             |



Table 3.2 – continued from previous page

| Test # | Configuration | Height (in) | Acceleration | Strain | Capacitance |
|--------|---------------|-------------|--------------|--------|-------------|
| 20     | B             | 72          | X            | –      | X           |
| 21     | B             | 66          | X            | –      | X           |
| 22     | B             | 60          | X            | –      | X           |
| 23     | B             | 54          | X            | –      | X           |
| 24     | B             | 48          | X            | –      | X           |
| 25     | B             | 42          | X            | –      | X           |
| 26     | B             | 36          | X            | –      | X           |
| 27     | B             | 30          | X            | –      | X           |
| 28     | B             | 24          | X            | –      | X           |
| 29     | B             | 18          | X            | –      | X           |
| 30     | B             | 12          | –            | –      | –           |
| 31     | B             | 72          | X            | –      | X           |
| 32     | B             | 36          | X            | –      | X           |
| 33     | B             | 12          | X            | –      | X           |
| 34     | A1            | 42          | –            | –      | –           |
| 35     | A1            | 48          | –            | –      | –           |
| 36     | A1            | 54          | –            | –      | –           |
| 37     | A1            | 12          | –            | –      | –           |
| 38     | A1            | 18          | –            | –      | –           |
| 39     | A1            | 24          | –            | –      | –           |
| 40     | A1            | 30          | –            | –      | –           |
| 41     | A1            | 36          | –            | –      | –           |
| 42     | A1            | 42          | X            | –      | X           |
| 43     | A1            | 48          | X            | –      | X           |

Least squares fit capacitance calculations in Matlab used identical functions as for the 3,000 VDC devices, but with changes in the values of the charge/discharge pulse frequency, amplitude, capacitance and resistance, in order to ensure accurate calculation of the new RC time constant.

### 3.2.3 Static Capacitance Measurements of Shocked Devices.

Once the capacitors were shocked with the drop tower in the laboratory, the high voltage devices were dismounted from the circuit board and their capacitance was measured using an impedance analyzer located at RXSA branch of the Materials and Manufacturing Directorate of AFRL on Wright-Patterson AFB. Static capacitance measurements were

performed in order to verify any permanent changes in capacitance as a result of the impact, and to investigate capacitance sensitivity to different frequencies.

Shocked components were dismounted according to AVX corporation mounting guide instructions [54] using the 33 watt MEISEI Corp HOT Tweezers with tip temperature of 210 degrees Celsius as measured by an HH611A thermometer. Capacitance and dissipation factor of the shocked, and control capacitors were measured at discrete frequencies of 100 Hz, 1 KHz, 10 KHz, 100 KHz and 1 MHz at +/-1 Volt oscillation level using an HP 4192 LF Impedance Analyzer with the HP 16048C test leads, and custom built, spring loaded test fixture, shown in Figure 3.10. Calibration of the impedance analyzer was performed after every change of frequency for shorted and open fixture configurations to ensure accuracy of the measurements.

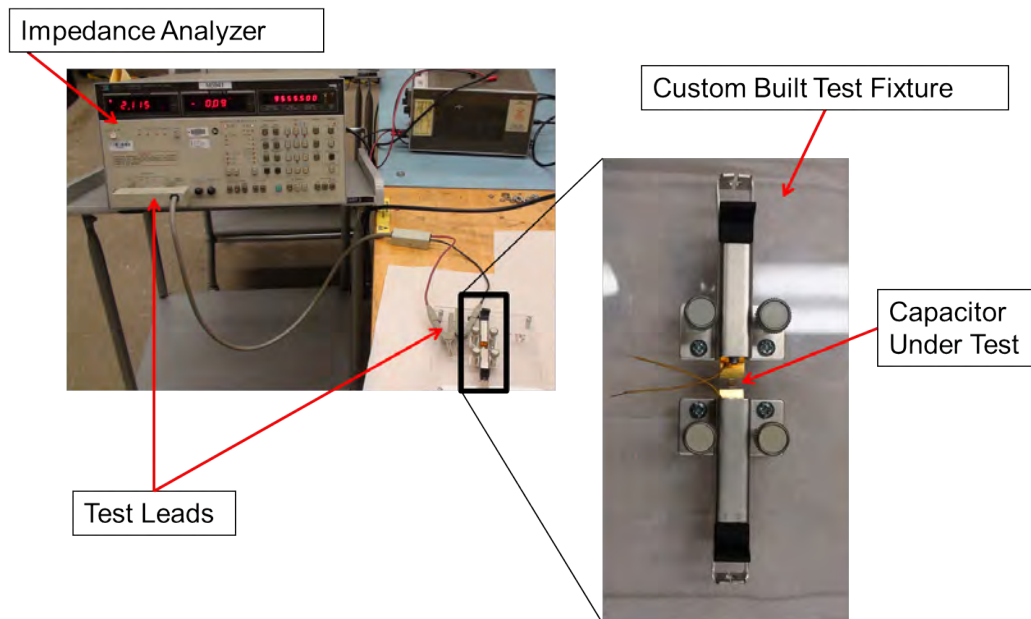


Figure 3.10: Static Capacitance and Dissipation Factor Measurement Set-up

### **3.3 Material Characterization Using the Scanning Electron Microscope**

Material composition of the dielectric material according to AVX, consisted up to 90% - 98% of Barium Titanate [24]. However, in order to verify the manufacturer's statement regarding the dielectric, to discover the chemical composition of the electrodes and terminals, as well as to measure the dimensions of the internal electrode structure for the sub-model, brand new high and low voltage capacitors were dissected and imaged using SEM with Energy Dispersive Spectroscopy (EDS) capabilities located at the Materials Characterization Facility (MCF) of Materials and Manufacturing Directorate of AFRL on Wright-Patterson AFB. Also, selected capacitors that failed during the drop impact, but, which were recovered after the experiments, were imaged in order to locate the exact material failure point to better understand the mechanical failure mechanisms of surface mounted devices.

Dropped components that were recovered post impact, as well as some surviving capacitors, were set along with the printed circuit board in CaldoFix 2 Hardener Resin using 25/7 resin/hardener ratio by weight, and baked for 17 hours in a 50 degree C oven. Once individual specimens were cured, diamond tipped circular saws were used to bisect and remount the test articles in the same epoxy with surfaces of interest orientated in a single planar layout inside a 2-inch diameter cup. The common surface was prepared using the 320, 600, 800 and 1200 grit round Silica Carbide circular disk sandpaper and coated with carbon for increased conductivity. The surface was also shorted using copper tape and silver paint to the aluminum mount in preparation for the SEM, as seen in Figure 3.11.

A total of 16 specimens set inside the 2-inch diameter puck, comprising 3,000 and 10 VDC capacitors along with dissected portions of the circuit board were imaged using FEI Quanta 600F Scanning Electron Microscope, shown in Figure 3.12. Devices were imaged using the 15 keV energy beam and a back-scatter tip at 57× to 2,500× magnification levels, depending on the specific region of interest, in order to measure dimensions of capacitors,

as well as to detect any mechanical abnormalities. Chemical composition was obtained via Energy Dispersive Spectroscopy using EDAX detectors for the dielectric, electrodes, terminals, solder, pads and the printed circuit board materials.

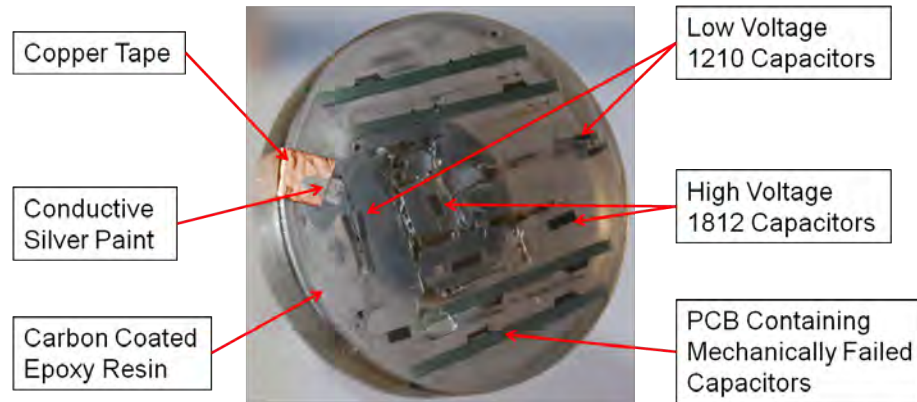


Figure 3.11: Test Articles Assembled in a Single Puck and Prepared for SEM Imaging

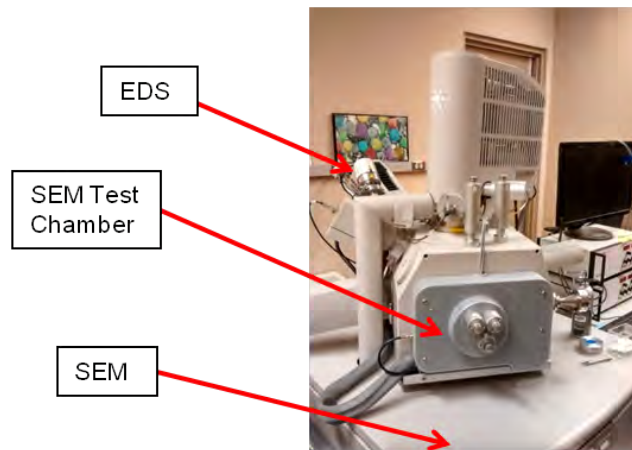


Figure 3.12: FEI Quanta 600F Scanning Electron Microscope

Once all the experimental data was gathered, including strain response of printed circuit board, dynamic and static capacitance measurements of high and low voltage

capacitors, and material composition of capacitors along with the structural layout of electrodes, the next step was to model board dynamics, and to conduct a computational parametric study to investigate sensitivity of the board strain response to various material properties in both frequency and amplitude. After the dynamic response of the board is computationally modeled, the final phase of the study was to create an accurate capacitor model in an RC circuit, apply realistic acceleration profile for both flexing and non-flexing board configurations and to determine if purely piezoelectric response can evoke the same electromechanical capacitance response of devices undergoing drop impacts, as observed in the laboratory.

### 3.4 Computational Model of PCB Dynamic Response

The computational model of the dynamic board response, was constructed using a 1/4 symmetry section of the fixture, clamps and the PCB in the Lagrangian frame of reference, as shown in Figure 3.13. The full test apparatus was drafted and meshed using the CUBIT version 13.2 geometry generating software available as part of the package in ALEGRA-EMMA version 5.0.

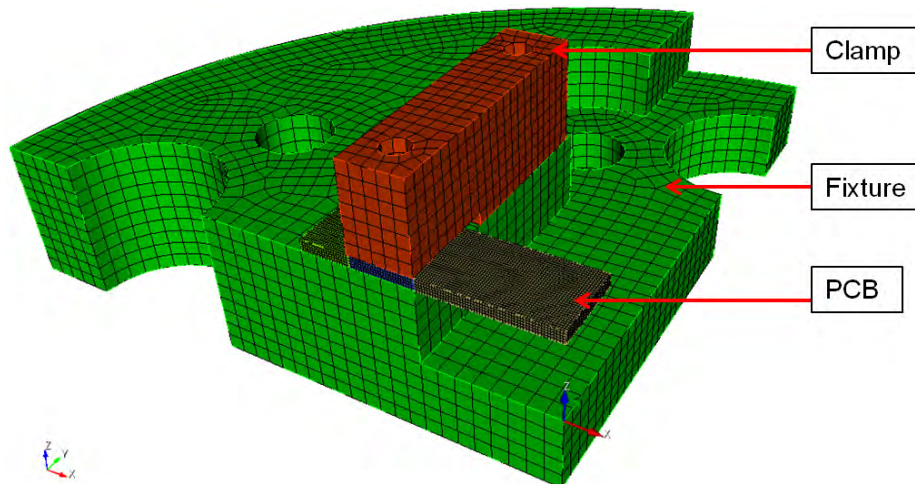


Figure 3.13: 1/4 Symmetry Computational Model for Dynamic PCB Response Validation

The entire model was implemented under Solid Dynamics physics section of ALEGRA and was meshed using a total of 23,832 hexagonal elements with the central, flexing, part of the circuit board being meshed with the smallest elements, comprising cubes with sides of 0.3048 mm. The material specifications for the clamps and fixture were based on SNL material library for 4340 Stainless Steel. The PCB was modeled using the generic equation of state with a linear elastic constitutive relationship, which required input parameters for Young's modulus, density, material speed of sound, temperature and constant volume heat capacity.

The Poisson's ratios of 0.177 and 0.171, as well as Young's moduli of 25.814 GPa and 21.9115 GPa were obtained from the manufacturer's specifications data sheet for direction along the fiber grain and in the fill direction respectively [55]. The constant volume heat capacity,  $C_v = 3.013$  kJ/K, was chosen based on the comparative PMMA material and the temperature input was the room temperature of the laboratory,  $T = 298$  K. The speed of sound  $C_s$ , was calculated using the relationship between density  $\rho$ , and bulk modulus  $K_{bulk}$ , in Equation (3.1), where the bulk modulus is given by the relationship between the Young's modulus  $E$ , and the Poisson's ratio  $\nu$ , in Equation (3.2).

$$C_s = \sqrt{\frac{K_{bulk}}{\rho}} \quad (3.1)$$

$$K_{bulk} = \frac{E}{3(1 - 2\nu)} \quad (3.2)$$

In the explicit finite element methods simulations are conditionally stable. Thus, the constant critical time step of  $t_{crit} = 38$  ns, was calculated according to the relationship in Equation (3.3), where  $h$  is the size of the smallest element.

$$t_{crit} \leq \frac{h}{C_s} \quad (3.3)$$

In the laboratory, black insulation tape was used to prevent surface traces in the PCB from shorting the connections, and thus the exact type of interfaces between the board and

the stainless steel components were difficult to recreate. Therefore, the clamp/board and board/fixture interfaces were modeled using frictionless and tied contacts, as well as by varying the coefficient of friction  $\mu = 0.5$  and  $0.3$ , to demonstrate that the effect of the type of contact surface on the dynamic board response was minimal. Also, the screws holding the clamps were not simulated because they would have minimal effect on the board dynamic response.

The accelerometer mounted on the top central portion of the fixture measured the acceleration only in the z-direction at this particular surface. However, the nodes, which were assigned the measured acceleration profile boundary conditions in the computational model were varied between the surface on which the accelerometer was mounted and the nodes in the entire fixture, in order to reduce undesired flexing of the stainless steel fixture. The unfiltered acceleration profile was used directly as the input boundary condition for the computational model and was also integrated to calculate the total change in velocity, which was later applied as a half-sine wave acceleration profile to investigate dynamic board strain response. Finally, another set of Young's modulus and the corresponding linearly extrapolated Poisson's ratio (17 GPa and 0.165 respectively) along with a lower board density of  $\rho = 1800 \text{ kg/m}^3$  was introduced in order to investigate the sensitivity of the dynamic board response to these parameters. The finite element model was parametrized using 36 runs according to the matrix in Table 3.3.

Table 3.3: Dynamic PCB Model Computational Parameter Matrix

| Run                    | Young's Modulus (GPa)<br>/ Poisson's Ratio |                    |                    | Density (kg/m <sub>3</sub> ) |      |      | Contact Type<br>(friction coefficient) |     |     |     | Acceleration<br>type |                 |
|------------------------|--|--------------------|--------------------|------------------------------|------|------|--|-----|-----|-----|----------------------|-----------------|
|                        | 25.8140<br>/ 0.177                         | 21.9115<br>/ 0.171 | 17.0000<br>/ 0.165 | 2090                         | 1904 | 1800 | Tied                                   | 0.5 | 0.3 | 0.0 | Fixture<br>Surface   | Fixture<br>Body |
| 1                      |  | X                  |                    |                              | X    |      | X                                      |     |     |     | X                    |                 |
| 2                      |  | X                  |                    |                              | X    |      | X                                      |     |     |     |                      | X               |
| 3                      | X  |                    |                    |                              | X    |      | X                                      |     |     |     | X                    |                 |
| 4                      | X  |                    |                    |                              | X    |      | X                                      |     |     |     |                      | X               |
| 5                      |  |                    | X                  |                              | X    |      | X                                      |     |     |     | X                    |                 |
| 6                      |  |                    | X                  |                              | X    |      | X                                      |     |     |     |                      | X               |
| Continued on next page |  |                    |                    |                              |      |      |  |     |     |     |                      |                 |

Table 3.3 – continued from previous page

| Run | Young's Modulus (GPa)<br>/ Poisson's Ratio |                    |                    | Density (kg/m <sub>3</sub> ) |      |      | Contact Type<br>(friction coefficient) |     |     |     | Acceleration<br>type |                 |
|-----|--|--------------------|--------------------|------------------------------|------|------|--|-----|-----|-----|----------------------|-----------------|
|     | 25.8140<br>/ 0.177                         | 21.9115<br>/ 0.171 | 17.0000<br>/ 0.165 | 2090                         | 1904 | 1800 | Tied                                   | 0.5 | 0.3 | 0.0 | Fixture<br>Surface   | Fixture<br>Body |
| 7   |  | X                  |                    |                              | X    |      |  | X   |     |     | X                    |                 |
| 8   |  | X                  |                    |                              | X    |      |  | X   |     |     |                      | X               |
| 9   |  | X                  |                    |                              | X    |      |  |     | X   |     | X                    |                 |
| 10  |  | X                  |                    |                              | X    |      |  |     | X   |     |                      | X               |
| 11  |  | X                  |                    |                              | X    |      |  |     |     | X   | X                    |                 |
| 12  |  | X                  |                    |                              | X    |      |  |     |     | X   |                      | X               |
| 13  |  | X                  |                    |                              |      | X    | X                                      |     |     |     | X                    |                 |
| 14  |  | X                  |                    |                              |      | X    | X                                      |     |     |     |                      | X               |
| 15  | X  |                    |                    |                              |      | X    | X                                      |     |     |     | X                    |                 |
| 16  | X  |                    |                    |                              |      | X    | X                                      |     |     |     |                      | X               |
| 17  |  |                    | X                  |                              |      | X    | X                                      |     |     |     | X                    |                 |
| 18  |  |                    | X                  |                              |      | X    | X                                      |     |     |     |                      | X               |
| 19  |  | X                  |                    |                              |      | X    |  | X   |     |     | X                    |                 |
| 20  |  | X                  |                    |                              |      | X    |  | X   |     |     |                      | X               |
| 21  |  | X                  |                    |                              |      | X    |  |     | X   |     | X                    |                 |
| 22  |  | X                  |                    |                              |      | X    |  |     | X   |     |                      | X               |
| 23  |  | X                  |                    |                              |      | X    |  |     |     | X   | X                    |                 |
| 24  |  | X                  |                    |                              |      | X    |  |     |     | X   |                      | X               |
| 25  |  | X                  |                    | X                            |      |      | X                                      |     |     |     | X                    |                 |
| 26  |  | X                  |                    | X                            |      |      | X                                      |     |     |     |                      | X               |
| 27  | X  |                    |                    | X                            |      |      | X                                      |     |     |     | X                    |                 |
| 28  | X  |                    |                    | X                            |      |      | X                                      |     |     |     |                      | X               |
| 29  |  |                    | X                  | X                            |      |      | X                                      |     |     |     | X                    |                 |
| 30  |  |                    | X                  | X                            |      |      | X                                      |     |     |     |                      | X               |
| 31  |  | X                  |                    | X                            |      |      |  | X   |     |     | X                    |                 |
| 32  |  | X                  |                    | X                            |      |      |  | X   |     |     |                      | X               |
| 33  |  | X                  |                    | X                            |      |      |  |     | X   |     | X                    |                 |
| 34  |  | X                  |                    | X                            |      |      |  |     | X   |     |                      | X               |
| 35  |  | X                  |                    | X                            |      |      |  |     |     | X   | X                    |                 |
| 36  |  | X                  |                    | X                            |      |      |  |     |     | X   |                      | X               |

For each run, a Lagrangian tracer was inserted inside the center-most element on the top surface of the circuit board to obtain the uniaxial, x-direction, strain results comparable to the strain gage data collected in the laboratory. However, the computational strain was collected at a slightly higher rate of every 380 ns (2.67 MHz) for a total of 1 millisecond. The dominant frequency response, as well as the peak strain amplitude were calculated using Fast Fourier Transforms (FFT) and compared to the strain data obtained in the



laboratory. All simulations were conducted in parallel over 8 cores on the local computer, or over 16 cores using the Air Force Institute of Technology (AFIT) Nordic Linux cluster, requiring four hours of wall time to complete each run.

Once the dynamic board response sensitivity study was completed and the strain oscillation frequency, and amplitude calculated by the computational model correlating to the respective acceleration profile closely matched the same experimentally measured parameters, appropriate boundary conditions to simulate stresses on the capacitor itself were obtained at the exact surface locations where the components were mounted. These acceleration profiles, obtained using the parametrized dynamic model of the PCB at the precise locations where the capacitors were soldered on the board, were used to apply realistic boundary conditions to the capacitor sub-model for the flexing board case. The next section describes the computational model designed to simulate and predict the electromechanical response of capacitors previously measured in the laboratory for both flexing board configuration A1, and for the non-flexing board configuration B.

### **3.5 Computational Model of Capacitor Electromechanical Response**

As mentioned earlier, the final objective of this study involved the development of the computational piezoelectric model of an MLCC for simulating the capacitance response to high-g drop impact. This objective was accomplished first, by structurally sub-modeling the capacitor in ALEGRA-EMMA using the same electrode layout design as obtained from SEM imagery using techniques described in Section 3.3. Then, the RC circuit with the identical charge/discharge pulse described in Section 3.2 was computationally simulated to ensure that components were electrically stressed in the same manner as during the experiments. Finally, the capacitor sub-model was mechanically stressed using the appropriate acceleration boundary conditions for both the flexing and non-flexing board cases. The goal of the implementation of methodologies in this section was to accurately predict the capacitance response measured in the laboratory using a

computational piezoelectric model with input parameters determined from a combination of literature review, experimental data and previously developed board dynamics model.

### 3.5.1 Capacitor Sub-model Development.

In order to create a structurally accurate model of the MLCC, dimensions of the electrodes and their positions within the dielectric material were measured using the SEM. The high voltage capacitor drop tests did not produce any electromechanical response during the impact due to the fact that components were not charged to high enough potential with the square wave pulse, which supplied only 0.33% of their rated voltage. Thus, only the low voltage capacitors that were charged through 80% of their rated voltage were modeled and investigated for their electromechanical response. The SEM image of the low voltage capacitor and the electrode layout structure of the device are shown in Figure 3.14.

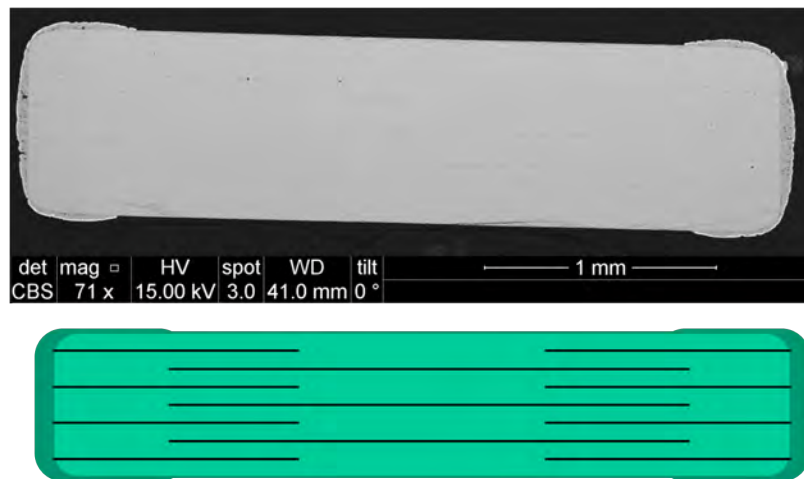


Figure 3.14: SEM Image of the 10 VDC XZ-Plane Cut Surface and Electrode Layout Schematic (not to scale)

In ALEGRA-EMMA, the dielectric material was modeled as a parallelepiped and the electrodes were represented by the designated surfaces of equal potential, called sidesets,

where volumes that make up the dielectric meet. Thus, the dielectric material was sectioned using blocks with dimensions that would allow for accurate size and layout assignment of the electrodes, as well as the overlap of the terminal and copper pad surfaces for applied boundary conditions. The assembled volumes representing the dielectric material, and the sidesets assigned to the electrodes, terminals and boundary conditions where mechanical stress is applied are shown in Figure 3.15 and Figure 3.16 respectively.

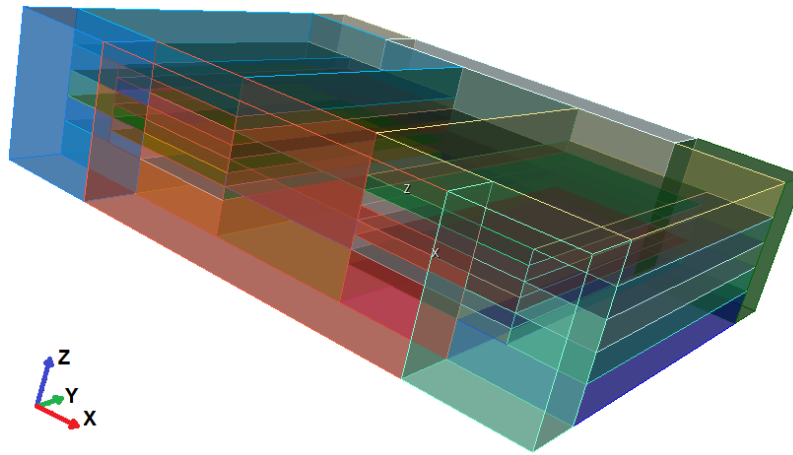


Figure 3.15: Low Voltage Capacitor Dielectric Volume Sections

The smallest and most critical dimension in the electrode structure, which is the distance in the z-direction between the floating, and the terminal-connected electrodes, was measured with the SEM to be  $70.84 \pm 0.5 \mu\text{m}$ . The required simulation time according to the experimental results needed to be no less than 2.5 milliseconds in order to fully capture the capacitance changes after the impact. However, in order to keep a reasonably stable time step that is not smaller than two nanoseconds, which would allow for the simulation to run long enough to capture the electromechanical response, the entire model was meshed using a grid containing elements no smaller than  $20 \mu\text{m}$  according to Equation (3.3). Thus,

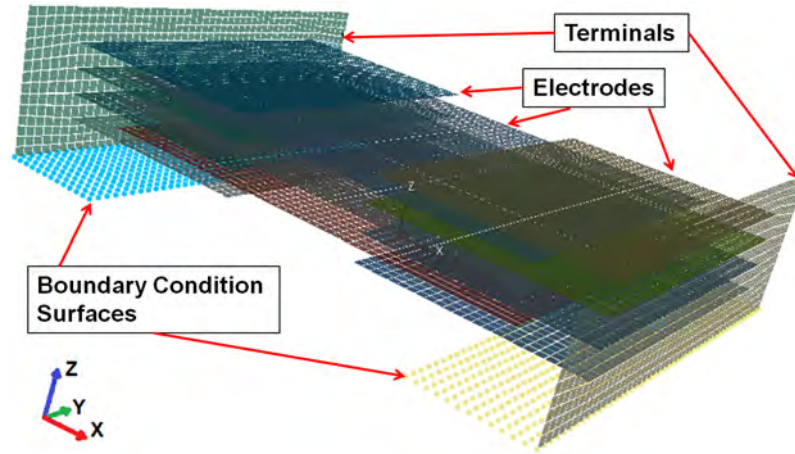


Figure 3.16: Electrodes, Terminals and Boundary Condition Surfaces

the dielectric parallelepiped was divided with volumes generated to within  $10\text{ }\mu\text{m}$  accuracy, which is an error of no more than 1.89% from the measured electrode layout dimensions.

The dielectric material was gridded using two similar types of meshes, but each having different element sizes, as seen in Table 3.4. The coarse mesh (C-mesh), shown in Figure 3.17, used  $50\text{ }\mu\text{m}$  hexagonal elements which spanned the critical dimension between connected and floating electrodes in a single element. The fine mesh (F-mesh), shown in Figure 3.18, used  $20\text{ }\mu\text{m}$  elements allowing for three elements to represent the critical distance. However, as will be discussed in the next chapter, the solution accuracy for the capacitance changes between the two different meshes was relatively small. Also, only two simulations would have been possible based on the 670,000 Central Processing Unit (CPU) hours on the Garnet High Performance Computer (HPC) that were provided for this work. Therefore, most simulations to investigate the electromechanical response of capacitors were conducted using the coarse mesh.

The genesis (.gen) file containing the mesh and all the sidesets of the material being modeled in ALEGRA-EMMA, was generated using CUBIT, just as in the case of the dynamic PCB response model. The size of the .gen file is important, because the output

(.exo) file size of ALEGRA for specified variables in the input (.inp) file is directly tied to the number of elements or nodes that represent field values. Thus, the larger the .gen file, the larger the output, necessitating huge amounts of memory, on the order of Tera-bites. Therefore, limitations with AFIT Linux network, which provided for no more than 250 GB of back-up space, was another reason to use the coarse mesh.

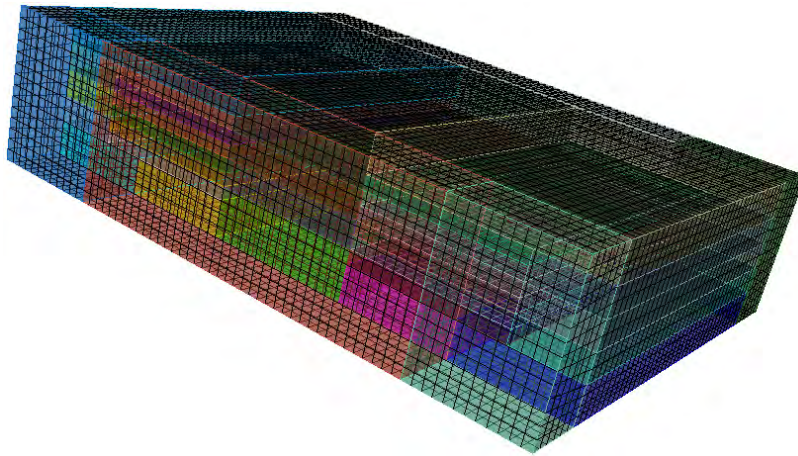


Figure 3.17: Coarse Mesh

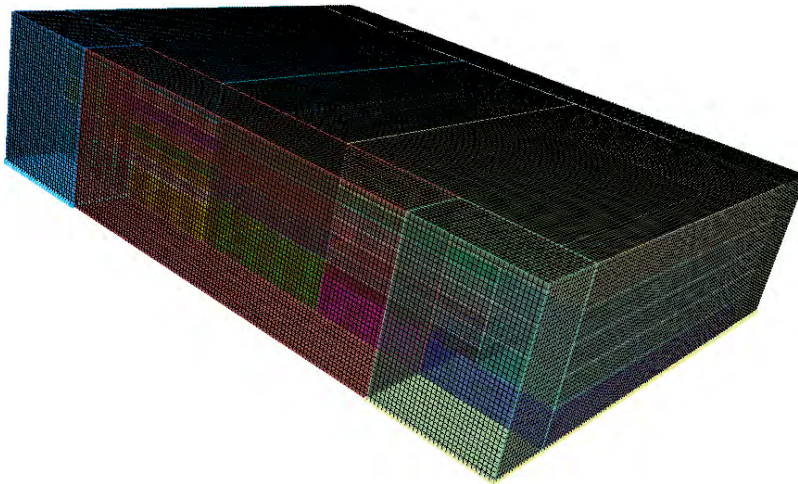


Figure 3.18: Fine Mesh

Table 3.4: The MLCC Mesh Parameters

|                      | <b>C Mesh</b>    | <b>F Mesh</b>    |
|----------------------|------------------|------------------|
| Number of elements   | 43,904           | 769,500          |
| Element size         | 50 $\mu\text{m}$ | 20 $\mu\text{m}$ |
| .gen file size       | 3.33 MB          | 50.36 MB         |
| Stable time step     | 4 ns             | 1.75 ns          |
| Total number of runs | 30               | 2                |

### 3.5.2 Computational RC Circuit Implementation.

Once an accurate MLCC model was created and appropriately meshed in CUBIT, it was inserted into the computational RC circuit, which accurately replicated the experimental set-up described in Section 3.2. The computational circuit consisted of a total of 15 circuit nodes, including 13 sidesets of the capacitor electrodes and terminals specified in CUBIT. The computational RC circuit also employed two elements, one representing the extremely small amount of inductance in the pulse transmission wire, and another imitating the 1 k $\Omega$  resistor in series with the MLCC model, as can be seen in Figure 3.19.

At any point in the simulation the voltage across the capacitor was obtained by calculating the potential difference between nodes 1 and 10. However, because node 1 was constantly grounded, only voltage at node 10 represented the potential difference across the capacitor. The square wave voltage input at node 15 simulated the charge/discharge pulse of +1 to +9 Volts at 50,000 Hz frequency, replicating the function generators in the laboratory to within a 10 nanosecond accuracy. The 3.21  $\mu\text{Henry}$  inductor simulated the inductance of the 20 feet of parallel wire separated by 2 mm, which represented appropriate inductance of the cable carrying the charge/discharge pulse in the experiment. Inductance of capacitors themselves used in this study becomes significant at frequencies over 4 MHz according

to the manufacturer, and thus was considered negligible during the dynamic capacitance measurements, making it unnecessary to replicate in the computational model.

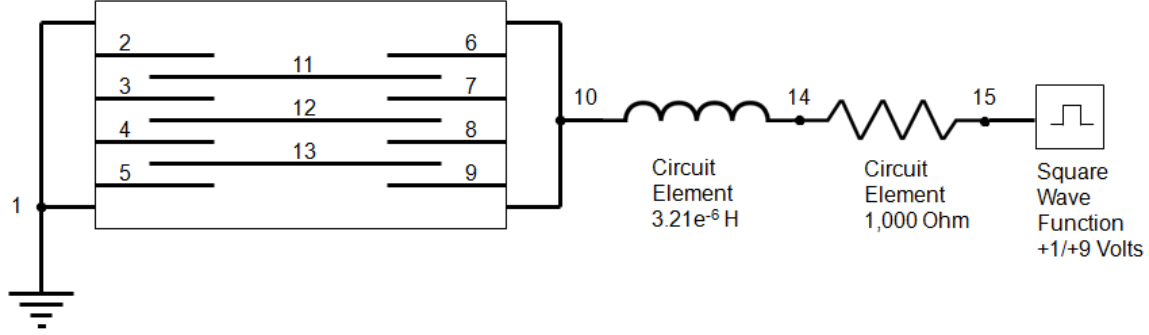


Figure 3.19: RC Circuit Model in ALEGRA-EMMA

However, a small amount of resistance within the electrodes and terminals,  $0.01834 \, \Omega$ , was calculated using equation  $R = (\rho l)/A$ , where resistivity of Nickel is given by  $\rho = 69.9 \, \text{n}\Omega \, \text{m}$ ,  $A$  is the approximate cross-sectional area of the electrodes and  $l$  is the length of the conductor. The relative and absolute error tolerances of the circuit solver to conduct the convergence test for divided difference of solution accuracy was set to within  $1\text{e-}5$ . Since the smallest input voltage value was 1 Volt, the solver error tolerances set to 5 orders of magnitude lower than the input into the model were sufficiently small for an accurate solution of the piezoelectric response of the capacitor under shock.

### 3.5.3 Input Parameters and Data Processing.

As mentioned earlier, piezoelectric material model was used for the dielectric in order to quantify the electromechanical response of the capacitor. In ferroelectric ceramics, due to planar isotropy imposed by the electric field when potential is applied, only certain elastic, piezoelectric and permittivity moduli components need to be specified to capture the material behavior under stress. In fact, Equation (3.4), Equation (3.5) and Equation (3.6) highlight the ten required elastic, piezoelectric and permittivity values

necessary to investigate electromechanical response of the material.

$$[C^g] = \begin{bmatrix} C_{11} & C_{12} & C_{13} & 0 & 0 & 0 \\ C_{12} & C_{11} & C_{13} & 0 & 0 & 0 \\ C_{13} & C_{13} & C_{33} & 0 & 0 & 0 \\ 0 & 0 & 0 & C_{44} & 0 & 0 \\ 0 & 0 & 0 & 0 & C_{44} & 0 \\ 0 & 0 & 0 & 0 & 0 & \frac{1}{2}(C_{11} - C_{12}) \end{bmatrix} \quad (3.4)$$

$$[e^g] = \begin{bmatrix} 0 & 0 & 0 & 0 & e_{15} & 0 \\ 0 & 0 & 0 & e_{15} & 0 & 0 \\ e_{31} & e_{31} & e_{33} & 0 & 0 & 0 \end{bmatrix} \quad (3.5)$$

$$[\mathcal{K}^g] = \begin{bmatrix} \epsilon_1 & 0 & 0 \\ 0 & \epsilon_1 & 0 \\ 0 & 0 & \epsilon_3 \end{bmatrix} \quad (3.6)$$

The nominal value for the elastic, piezoelectric and permittivity constants for Barium Titanate ceramics that were applied to the Piezoelectric model were obtained from literature and are outlined in Table 3.5 [11]. While elasticity and piezoelectric moduli were readily specified, the two permittivity constants first had to be calculated using the relationship between the coupling factor  $k$ , constant electric field compliance  $s$ , and the converse effect piezoelectric constant  $d$ , as seen in Equation (3.7) and Equation (3.8) below.

$$\epsilon_1 = \left( \frac{d_{15}}{k_{15}} \right)^2 / s_{44}^E \quad (3.7)$$

$$\epsilon_3 = \left( \frac{d_{31}}{k_{31}} \right)^2 / s_{11}^E \quad (3.8)$$



Table 3.5: Elastic, Piezoelectric and Permittivity Moduli Constants [11]

| Constant                     | Barium Titanate Ceramic Value |
|------------------------------|-------------------------------|
| $C_{11}$ (N/m <sup>2</sup> ) | $166 \times 10^9$             |
| $C_{12}$ ”                   | $76.6 \times 10^9$            |
| $C_{13}$ ”                   | $77.5 \times 10^9$            |
| $C_{33}$ ”                   | $162 \times 10^9$             |
| $C_{44}$ ”                   | $42.9 \times 10^9$            |
| $e_{15}$ (C/m <sup>2</sup> ) | 11.6                          |
| $e_{31}$ ”                   | -4.4                          |
| $e_{33}$ ”                   | 18.6                          |
| $\epsilon_1$ (F/m)           | $13.81 \times 10^{-9}$        |
| $\epsilon_3$ ”               | $16.81 \times 10^{-9}$        |

Ideally, experimental measurements of the above ten constants for the exact Barium Titanate based dielectric material used inside the capacitors that were stressed would be used for the computational model. However, while the procedures for obtaining permittivity, elasticity and piezoelectric moduli constants have been clearly outlined in the literature and have been published by the Institute of Electrical and Electronics Engineers (IEEE) [56], the technique used to investigate material properties of ferroelectric materials requires an elaborate experimental set-up, specialized laboratory equipment and specifically unique dimensions of the material specimen, none of which were available for this study. Thus, the values available in literature for the Barium Titanate ceramic, that were outlined in Table 3.5, were used to obtain piezoelectric response of the dielectric material, and only rudimentary parametric study was performed in order to validate computational model sensitivity to the varied moduli by significantly and systematically changing elastic, piezoelectric and permittivity constants' values, and exploring their effect on the solution.

Boundary conditions for the capacitor sub-model were specified by applying the acceleration profiles based on the board dynamics. In the case of a flexing PCB, A1 configuration, board dynamics simulations outlined in Section 3.4 were first conducted to obtain the x, y and z-direction acceleration profiles at the center of the surface of the pad/capacitor interfaces, and then applied to the entire capacitor sub-model surface, where the copper pad is in contact with the terminal through solder, as shown in Figure 3.16. However, in the case of the board that was mounted directly on the flat fixture surface, non-flexing B configuration, x and y-direction accelerations were negligible. Thus, the z-direction accelerometer profile measured during the drop was applied directly to the pad/capacitor terminal interface surface. In the non-flexing, B configuration, both filtered and non-filtered accelerometer data was used for boundary conditions. However, it was quickly determined, that using filtered or half-sine boundary conditions replicating the change in velocity experienced by the capacitor during the drop impact did not produce electromechanical effects that were observed during the experiment. Thus, for investigations of piezoelectric response, raw and unfiltered accelerometer data was used for all the boundary conditions of the non-flexing board configuration drops, and also as boundary condition in the board dynamics computations to obtain the triaxial surface acceleration profiles for the flexing board case.

Piezoelectric response simulations were ran for 4 milliseconds for the flexing board configuration in order to attempt to capture at least a few periods of board flexure after the impact and 2.5 milliseconds in the non-flexing board case, in order to capture the entire electromechanical response observed in the laboratory, while still attempting to conserve computational power allocated on Garnet HPC. The field variable plot was emitted every  $10\ \mu\text{s}$  and the electric field, potential, permittivity and pressure variables, along with voltages at each node, were written every  $1\ \mu\text{s}$  second. A total of 990 tracers were inserted into the dielectric region occupied by the electrodes to obtain quantitative data used later

to determine capacitance of the modeled MLCC. However, due to the overwhelmingly uniaxial board strain, at least in the flexing board case, pressure and permittivity changes in the y-direction were negligible requiring only three columns of tracers. Therefore, 30 rows in the x-direction, 3 columns in the y-direction and 11 levels of tracers in the z-direction, shown in Figure 3.20, were used to obtain the critical z-direction permittivity.

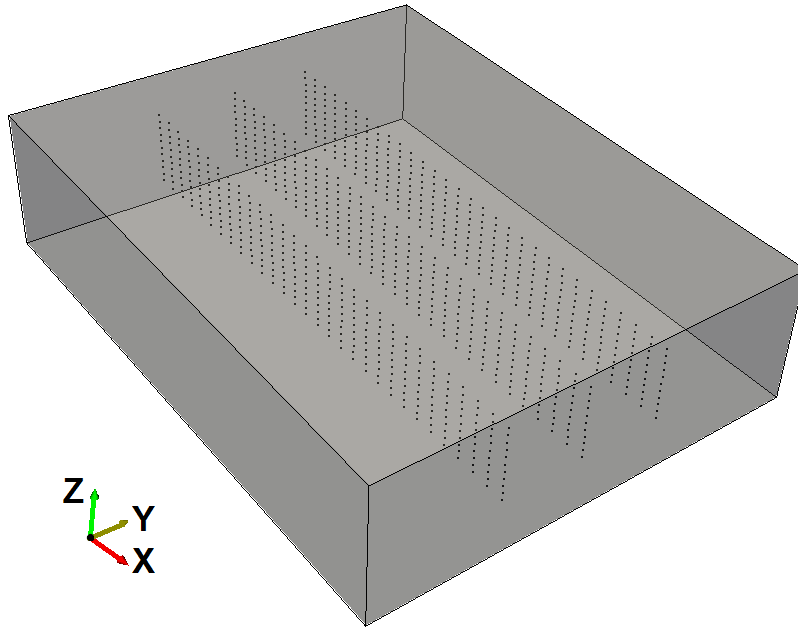


Figure 3.20: Layout of Tracers in the Capacitor

The permittivity changes during and after the shock were obtained from each tracer using hisread.py function of ALEGRA-EMMA. The computationally obtained permittivity data was processed in Matlab in order to calculate the change in capacitance of the device for both flexing and non-flexing board configurations, which in turn was plotted against the experimentally obtained data for comparison. From comparison between experimental capacitance measurements and computationally calculated electromechanical response, constitutive relationships for capacitance changes under dynamic high-g mechanical loads were developed.

### 3.6 Uncertainty Analysis

As with any value measured in the laboratory, an estimate of error must be supplied in order to determine if the equipment or numerical model used in the study provided enough resolution to capture the types of effects being investigated. One of the sources of error with the RC capacitance calculation technique, was due to the resolution of the voltage that was measured by the oscilloscope at high data rate. The accuracy of the voltage measurements obtained during the drop tower experiments was within  $\pm 0.1$  Volts, translating into capacitance calculation uncertainty of less than 0.5 pF. Based on the voltage error propagated through the least squares fit function in order to determine the capacitance value of the devices undergoing impact, the standard deviation of the RC measurement method was calculated to be 18.3 pF, which is less than one half of one percent of the nominal value for the 10 VDC capacitors and two percent for the 3,000 VDC components. The combined accuracy of less than 1% of the RC measurement technique was sufficient to detect the transient capacitance variations as a result of the impact shock.

Another source of error, was encountered during the static capacitance measurements. The impedance analyzer error was based on the frequency at which the capacitance was measured, and ranged in value between  $\pm 0.1$  pF at 1 MHz and  $\pm 100$  pF at 10 Hz. Similar frequency-based order of magnitude differences in error were present during the dissipation factor determination, which was conducted concurrently with the capacitance values using the impedance analyzer. However, because the impedance analyzer was utilized to measure static variations in capacitance of the mechanically failed components, the less than  $\pm 5$  pF accuracy of the impedance analyzer was sufficient enough starting at frequencies above 100 Hz.

As previously mentioned, the SEM measurements of the dimensions of the physical layout of the electrodes were within  $\pm 0.5$   $\mu\text{m}$ . Additionally, due to the finite element discretization, the simulated electrode layout error was increased to 20  $\mu\text{m}$  with the

coarse mesh, which translated to a 31% error based on the numerical RC measurement, where the computationally predicted capacitance of the device sub-model was 1,470 pF, instead of 2,200 pF measured in the laboratory. However, the uncertainty in the Barium Titanate dielectric permittivity values was easily capable of offsetting the physical layout discretization error. Therefore, because the focus of this study was to experimentally measure and numerically predict the piezoelectrically induced variations in capacitance, the same order of magnitude differences between the nominal value and the computationally calculated capacitance of the devices was acceptable. Furthermore, a grid convergence study was conducted for a single computational run with 20  $\mu\text{m}$  elements, which reduced the discretization error to within 10  $\mu\text{m}$ , significantly decreasing the discrepancy between the experimentally measured capacitance variations and the numerical calculations, as discussed in the next chapter.

Implementation of the methodology discussed in this chapter, illustrated in the flow chart in Figure 3.21, accomplishes all three objectives outlined in the literature review. First, dynamic board response of a PCB housing surface mounted components subjected to drop shocks on the order of 20,000 g is accurately simulated using a newly developed solid dynamics computational model validated by the experimentally obtained uniaxial surface strain oscillation frequency and amplitude data. Second, electromechanical capacitance response of ferroelectric dielectric capacitors is measured in the laboratory using the RC circuit technique designed to charge and discharge the MLCC, and electrode structure of the capacitors, as well as the base dielectric material of capacitors is verified with a scanning electron microscope. Finally, computational sub-model predicting the piezoelectric response to the conditions explored in dynamic board response investigations, as well as under non-flexing board conditions, is developed and validated against the experimentally obtained capacitance data.

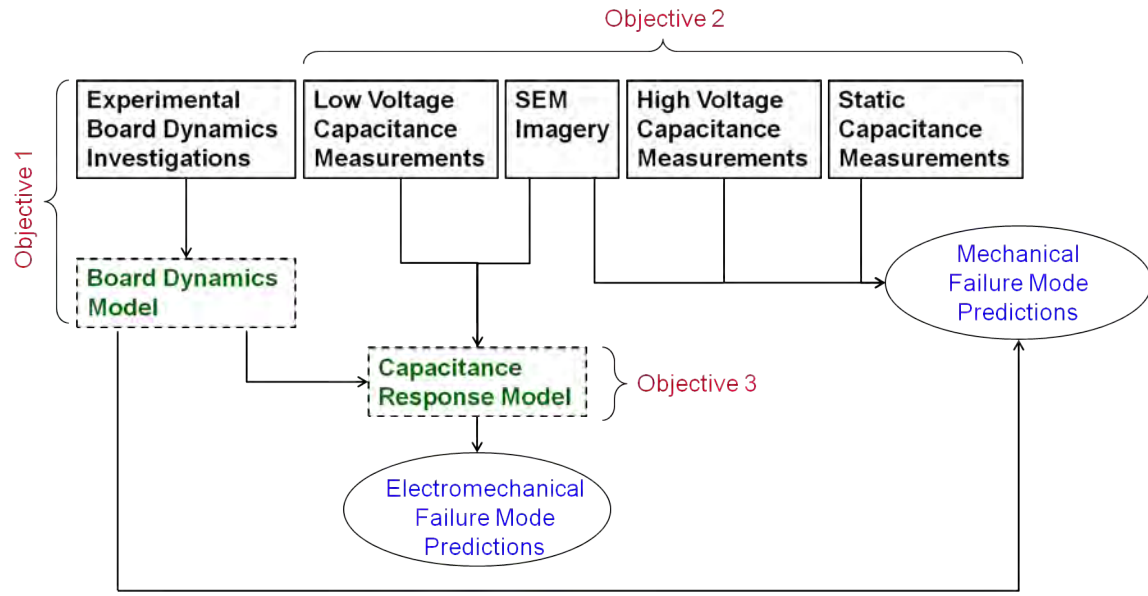


Figure 3.21: Methodology Flow Chart (solid boxes are experimentally obtained data, dashed boxes are computational models and ovals are research goals)

The end goal of executing the above techniques is to investigate both the mechanical and electromechanical modes of failure of circuitry utilizing ferroelectric dielectric capacitors exposed to high-g drop impacts. By developing computational models and constitutive relationships predicting electromechanical response of capacitors observed in the laboratory, and detecting mechanical modes of failure, component performance under harsh conditions may be predicted with greater degree of accuracy. From these predictions of piezoelectric response of ferroelectric capacitors under harsh mechanical stresses, circuitry design rules may later be modified to improve survivability of electronic packages and overall reliability of aerospace technology exposed to high-g impacts.

#### IV. Results and Analysis

The execution of the experimental and computational methodologies described in the previous chapter to accomplish objectives outlined in Chapter 2 resulted in three distinct phases of research. The first phase focused on developing the computational model, which accurately simulates dynamic surface strain response of a printed circuit board undergoing high-g drop tower tests. The first phase of this research was absolutely necessary, because very few studies exist in the literature that describe board dynamics under acceleration profiles an order of magnitude greater than in commercially relevant environments. If board oscillations post impact cannot be accurately predicted, calculating surface strain on the board at the locations where the capacitors are mounted and computationally predicting the exact boundary conditions to be applied to the ferroelectric dielectric sub-model would be extremely difficult. Strain gages would have to be applied at every pad/terminal interface surface, which would be impractical for different board trace layouts. Therefore, the first phase proves through a parametric study that using a simple linear elastic material computational model for the board accurately predicts strain oscillation frequency and amplitude at the center of the board when compared to the experimentally measured values. In essence, the first phase experimentally validates the computational dynamic surface strain response model, from which accurate acceleration profiles can be obtained and later applied as boundary conditions when calculating electromechanical response of the ferroelectric ceramic capacitors.

The efforts of the second phase in this research were focused on experimentally obtaining capacitance response of the capacitors mounted on the flexing PCB, the dynamics of which have been computationally modeled in phase one, and the non-flexing board, which was mounted directly on the surface of the stainless steel fixture. For the flexing board case, measuring capacitance during the high-g drop impact uncovered the

mechanical mode of failure resulting from an intermittent loss of contact and eventual complete failure during board oscillations, as well as the electromechanical increase of capacitance, both directly correlating to the board strain oscillations post-impact. However, no capacitors mechanically failed during the drop in the non-flexing board configuration, due to the inherently lower solder joint stresses than in the flexing board scenario, and only electromechanical failure response was observed in the laboratory. Also, in phase two of the research, mechanically failed components were recovered and imaged under the SEM to verify the flexural mode of failure in the flexing board case and also to verify that the dielectric material is based on the ferroelectric Barium Titanate ceramic chemical composition. Finally, static capacitance measurements proved that in the case of the floating electrode capacitors, partial loss of contact between the electrodes and the terminal leads to a proportional decrease in capacitance even if the component has not yet completely separated from the PCB.

As pointed out in Chapter 2, a fair amount of computational studies in the literature have been devoted to the mechanical failure mode of components in the electronics packages undergoing 3,000 g acceleration profiles. However, no research has been dedicated to the piezoelectric response of the ferroelectric ceramic dielectric materials inside capacitors undergoing high-g drop impact. Thus, the third, and final phase of this research is focused on computationally modeling the electromechanical response of the structurally accurate MLCC sub-model that uses a high permittivity Barium Titanate ceramic dielectric in a simple RC circuit, identical to the one that was used to measure capacitance of components undergoing realistic dynamic flexing and non-flexing high-g mechanical shocks in the laboratory. Under the flexing board conditions validated during phase one, the computationally calculated electromechanical response requires a correction in order to directly correlate to the board surface strain oscillations. However, in the non-flexing board scenario, due to fewer degrees of freedom and simpler board dynamics,



computational electromechanical response can be obtained directly from the magnitude of the change in permittivity constants during and after the shock using a simple constitutive relationship, developed as a result of this study.

#### **4.1 Phase I: PCB Dynamics Under High-g Drop Impact Stress**

Phase I was designed to create a computational model of board dynamic response under high-g impact, and through a parametric study, validate its predictions against the strain oscillations measured in the laboratory. However, before developing the computational PCB model, impact experiments had to be carried out to investigate the drop tower shock repeatability and predictability, in order to ensure acquisition of proper boundary conditions that were used to calculate the dynamic response of the board, as well as the capacitance changes of capacitors, under the high-g mechanical stress. Since the acceleration profile boundary conditions are highly critical in both the flexing and non-flexing board capacitance investigations, as they directly relate to the high-g mechanical stress, it is important to discuss some of the characteristics and limitations of the drop tower and post processing of the accelerometer data. Thus, the next subsection describes the correlation between drop height, total change in velocity, and acceleration profiles, since these parameters are very important when describing the quality of the shock impact.

##### ***4.1.1 Drop Tower Characterization and Data Processing Effects.***

As mentioned in Chapter 3, variations in peak acceleration, as well as in the shock profiles during the drop impact test series necessitated the use of accelerometer to measure exact impact conditions during every drop tower run. Thus, almost 100 accelerometer profiles were captured during the experimental research phases, ranging between 12 and 72 inches in drop height, from 2.2 to 12.8 m/s in total change in velocity and peak acceleration levels from 666 g to 23,961 g, as shown in Table 3.1 and Table 3.2. After the acceleration and strain data was acquired with the Precision Filters signal conditioner, it was processed in Labview and filtered in Matlab to reduce high frequency data anomalies.

Both accelerometer and strain gage data were processed using a low pass, 8<sup>th</sup> order polynomial, 3 dB frequency and 0.01 Pi radians/sample Butterworth filter. The effects of data processing and how filtered data compares with raw data during a particular 36–inch height drop, which is in the center of the drop tower operating envelope and used for the majority of the drop tower tests in this study, are displayed in Figure 4.1 and Figure 4.2.

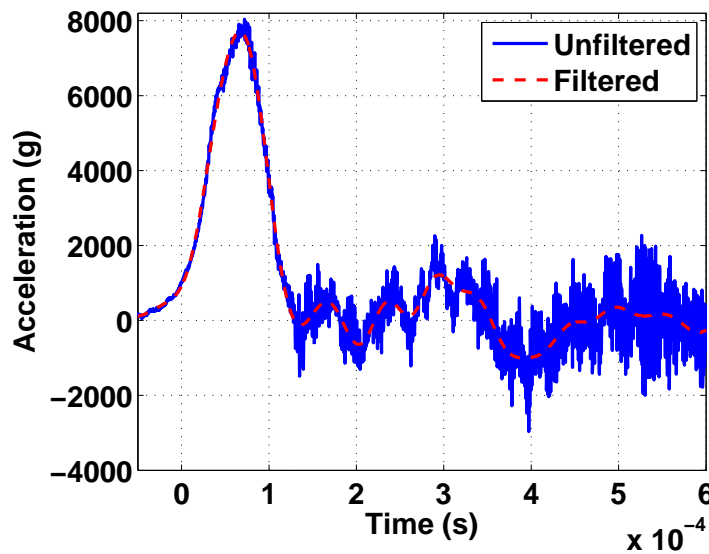


Figure 4.1: Filtering Effects on Accelerometer Data

As can be seen in Figure 4.2, the low pass filter effectively eliminates the strain gage data outliers without reducing the amplitude of the strain that was measured by the instrument during and post impact board oscillations. However, in the case of the accelerometer data, it was impossible to completely filter out the high-frequency response without significantly reducing the peak amplitude of the shock, or its post impact effects, as seen in Figure 4.1. Also, while filtering strain data reduced the outliers that are clearly unphysical, the accelerometer profile contains variations in data that could be explained by a combination of rigid body translations and high frequency vibrations of the stainless steel

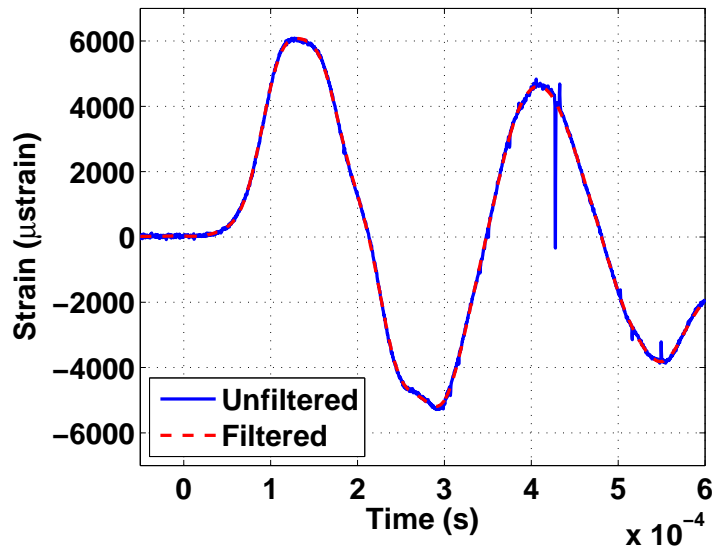


Figure 4.2: Filtering Effects on Strain Gage Data

material post impact. Thus, while experimentally gathered strain data was always filtered for comparison with computationally calculated board strain results, acceleration profiles, whether used for dynamic board response investigations in a computational parametric study, or for the computational capacitance response measurements, were not filtered, but applied directly as boundary conditions to the models in their raw, unfiltered form.

Another complicating characteristic of the accelerometer data gathered during drop tower experiments was the undesired effect of changes in felt programmer material properties with each run, resulting in a progressively impacted material response. When a new programmer material inserted between the seismic mass and the anvil is used during a drop, some of the energy of the shock is dissipated over time to produce a lower peak acceleration over a longer impact duration, which is called acceleration profile shaping. However, as the material becomes progressively more impacted with each drop, the same drop height impact results in a similar total change in velocity magnitude, but with sharper acceleration profile featuring a significantly increased peak acceleration and a shorter shock

duration. The effect of impacted felt programmer material was evidenced in the high voltage capacitor investigations over more than 60 drops, and, to a lesser degree, during the low voltage capacitor test series of 43 drops, as can be seen respectively in Figure 4.3 and Figure 4.4.

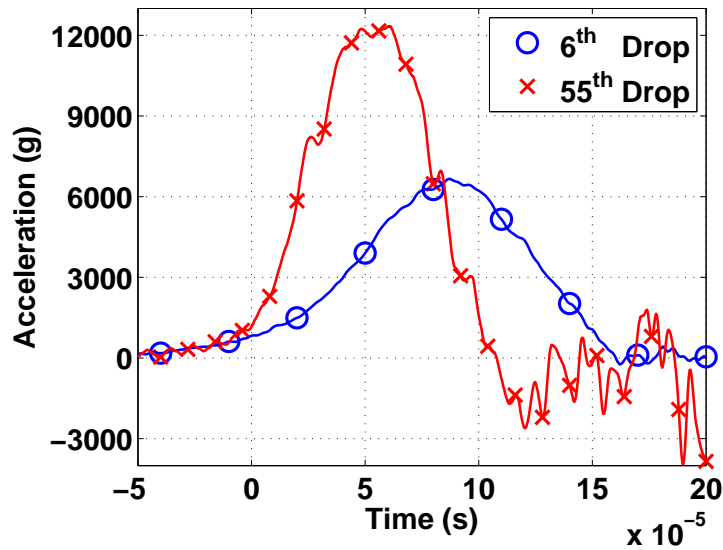


Figure 4.3: Impacted Programmer Effects During High Voltage Capacitor Tests

The acceleration profiles represented in Figure 4.3 and Figure 4.4 were collected during four separate 36-inch height drops over two separate test series using similar, but different 1/8 inch programmers. Over the course of 50 drops of the high voltage capacitors using the same felt programmer, the peak acceleration grew by half an order of magnitude (~85%) throughout the test series, from 6,666 g to 12,340 g, while the change in velocity, due to shorter impact duration, increased only by 20% from 6.20 m/s to 7.43 m/s, as seen in Figure 4.3. Similar effects of the impacted programmer felt for different drop heights are displayed in Table 4.1. While, the change in velocity during a drop from a particular height did not vary by more than 20%, making it seem appropriate on the surface to describe the

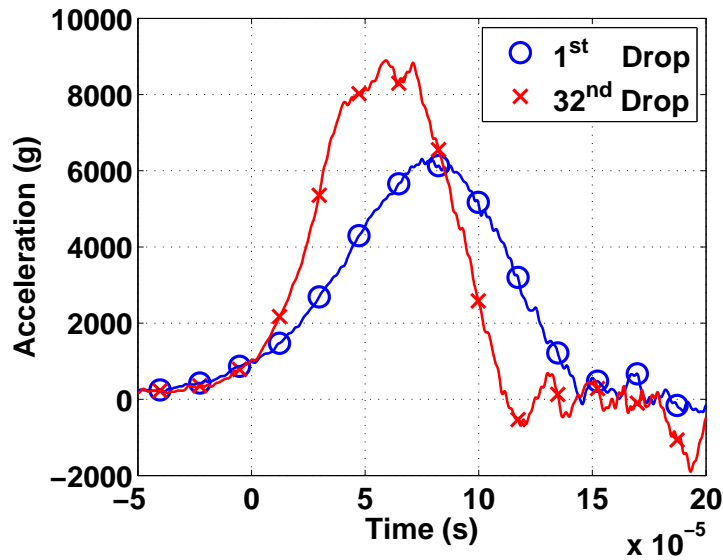


Figure 4.4: Impacted Programmer Effects During Low Voltage Capacitor Tests

mechanical stress with one value, just by itself, the  $\Delta V$  metric does not describe the entire shock event, making it necessary to provide the entire acceleration profile in order to fully apply the boundary conditions.

The change in acceleration profile during the low voltage capacitor drops was not as drastic over 32 runs, but the peak acceleration still changed by over 41% from 6,310 g to 8,897 g for a 36-inch drop, as seen in Figure 4.4. Such significant variations in the peak accelerations between drops from identical heights provided the most compelling reason for measuring the acceleration profile during every drop, necessitating the use of only one particular 36-inch height drop profile as a boundary condition for the dynamic board response parametric study, as opposed to a weighted average of acceleration profiles from multiple 36-inch runs. Even more important, as will become clear later in the chapter, is the application of the appropriate, unfiltered, individual acceleration profile data as a boundary condition when computationally calculating a particular capacitance response of devices mounted on both the flexing and non-flexing boards. Since each drop produces an

inherently unique set of mechanical stresses, as witnessed by the significantly different individual acceleration profiles, computing capacitance response during drop shocks in order to develop constitutive relationships between mechanical stress and changes in capacitance, requires a careful application of the prescribed boundary conditions for every different drop.

Table 4.1: Effects of Impacted Programmer on Acceleration Profile Over 50 Runs

| Drop Height<br>(in) | First Five<br>Drops      |                     | Last Five<br>Drops       |                     | Percent<br>Change        |                   |
|---------------------|--------------------------|---------------------|--------------------------|---------------------|--------------------------|-------------------|
|                     | Peak<br>Acceleration (g) | $\Delta V$<br>(m/s) | Peak<br>Acceleration (g) | $\Delta V$<br>(m/s) | Peak<br>Acceleration (%) | $\Delta V$<br>(%) |
| 12                  | 662                      | 3.93                | 3,217                    | 3.72                | 386                      | -5                |
| 18                  | 1,584                    | 4.52                | 5,526                    | 5.20                | 249                      | 15                |
| 24                  | 2,659                    | 5.77                | 7,940                    | 6.18                | 199                      | 7                 |
| 30                  | 4,386                    | 5.59                | 10,576                   | 6.00                | 141                      | 7                 |
| 36                  | 6,666                    | 6.20                | 12,340                   | 7.43                | 85                       | 20                |

Now that the importance of unique acceleration profiles applied as boundary conditions has been established, and limitations of accelerometer data generated by the drop tower have been addressed, it is possible to proceed with the computational parametric board dynamics study outlined in Section 3.4. Thus, the following subsection describes the sensitivity of the dynamic board response computational model to the variation in material parameters as compared to the experimentally obtained strain data at the center top surface of the PCB.

#### ***4.1.2 Computational PCB Model Performance.***

The experimental drop impact data selected for the computational parametric study of the dynamic board response was based on a 36-inch drop, which, as described in the previous subsection, resulted in a unique set of acceleration and strain profiles. The experimentally obtained dynamic board response generated a maximum surface tensile strain of 6,309  $\mu$ strains with a dominant strain oscillation frequency of approximately

4,375 Hz. Such strain response was a result of a shock with a total change in velocity,  $\Delta V = 6.74$  m/s, and a maximum peak acceleration of 15,754 g. The acceleration profile that was measured during the event was used as an initial boundary condition in the finite element model predicting the dynamic board surface strain oscillations by applying it directly to the model, and also by first integrating the change in velocity during the impact, and then applying the equivalent half-sine input as the initial acceleration profile function, both seen in Figure 4.5.

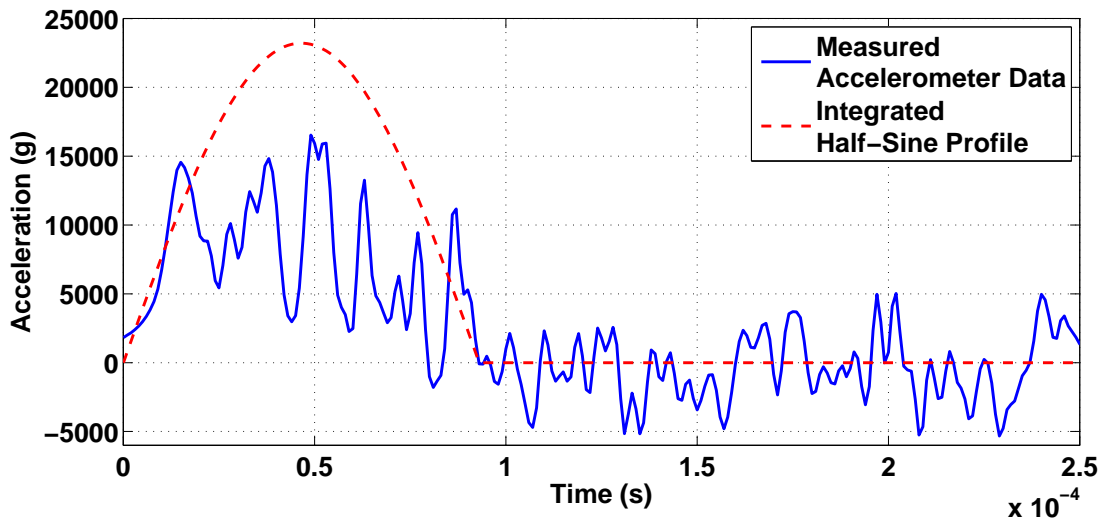


Figure 4.5: Acceleration Profiles Used for Dynamic PCB Response Study

Two different methods were used to apply boundary conditions to the finite element model. The first, a surface-driven method, applied the laboratory measured acceleration only to the nodes located on the surface of the fixture, to which the accelerometer was attached during the tests. The surface-driven method was used in all the odd-numbered runs in Table 3.3. The second, a body-driven method, applied the measured acceleration profile to the nodes in the entire fixture and is reflected in all the even-numbered runs. Both surface and body-driven methods employed raw accelerometer data as the boundary

condition for all the runs in Table 3.3, but, due to uniqueness of each acceleration profile representing specific mechanical stresses during each separate drop, as discussed in the previous subsection, only a single computation was conducted for comparison with the half-sine acceleration profile.

Both body and surface-driven methods produced a dominant frequency response close to the experimental results. However, compared to the body-driven method, surface-driven acceleration also generated medium frequency oscillations, on the order of 7,600 Hz in the strain response that were evident in the FFT plot, in Figure 4.6.

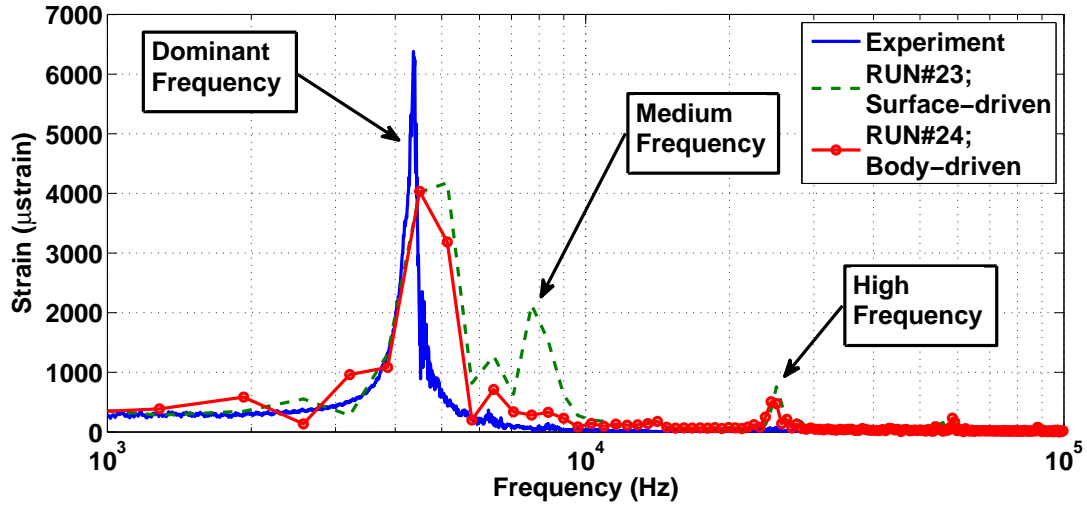


Figure 4.6: Surface vs. Body Driven Acceleration FFT;  $E = 21.9115 \text{ GPa}$ ,  $\rho = 1800 \text{ kg/m}^3$ , Frictionless Contact Type

The 4,375 Hz frequency represented the dominant strain oscillation frequency, while the medium frequency response between 7,000 and 8,000 KHz was due to a combination of the variations in the acceleration profile and the flexing of the fixture walls normal to the YZ plane. Therefore, the medium frequency response was more pronounced in the surface-driven boundary condition runs. The fact that the medium frequency response was partly



due to the fixture flexing was validated by the evidence that in every surface-driven run the top surface of the board initially experienced a significant amount of tension, as outlined by the red box in Figure 4.7.

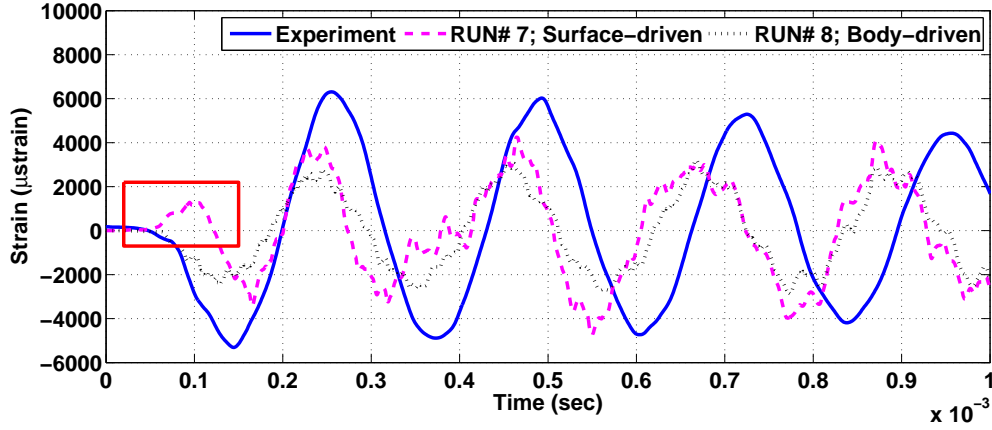


Figure 4.7: Surface-Driven vs. Body-Driven Acceleration Strain Responses;  $E = 21.9115 \text{ GPa}$ ,  $\rho = 1904 \text{ kg/m}^3$ , Contact Type  $\mu = 0.5$

The peak amplitude was higher for surface-driven runs than in the body-driven cases, which was the result of additional strain imposed on the board by the flexing fixture. Portions of high frequency strain response were likely due to significant variations in the acceleration profile and were much less pronounced in the cases where the acceleration profile was a half-sine wave. Some high frequency responses were also due to the oscillation of the clamp normal to the YZ plane, which was more evident when the friction coefficient was reduced.

Out of the four varied parameters in the run matrix, Young's modulus  $E$ , and density  $\rho$ , had the greatest effect on both the peak strain amplitude and on the dominant frequency response, regardless of the amount of friction or acceleration method. As would be expected, due to the fact that the same amount of energy was transferred to the more elastic material, with the decrease in Young's modulus, the peak strain significantly increased for

a given density, as seen in Figure 4.8. Also, due to the increased elasticity, decreasing the elastic modulus significantly reduced the dominant frequency.

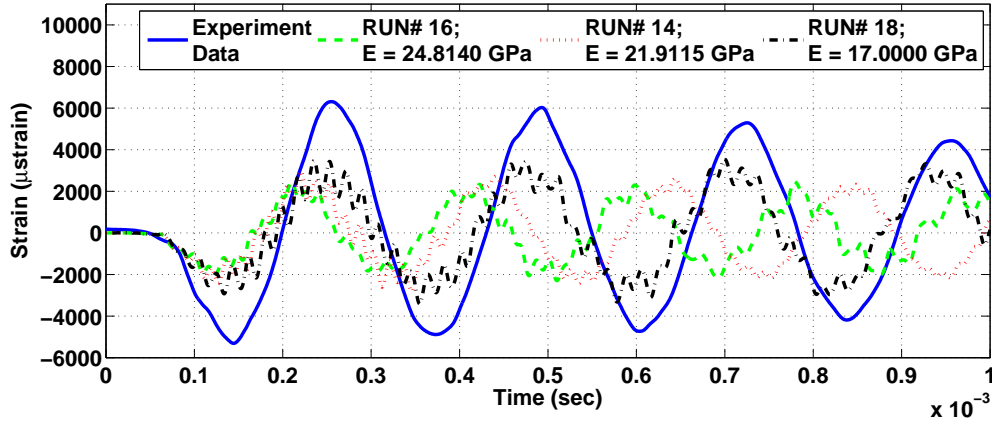


Figure 4.8: Effect of Young's Modulus on Strain Response;  $\rho = 1,800 \text{ kg/m}^3$ , Tied Contact Type, Body-Driven BC

Density also had a relatively pronounced effect on the dominant frequency of the strain response and on the peak strain amplitude. As density increased, the dominant frequency was slightly reduced, while the peak amplitude increased based on the almost 14% increase in board mass and thus kinetic energy, as can be seen in Figure 4.9.

Based on the relationship between stress and strain in the linear elastic model that did not exhibit dampening, it was reasonable to assume that over a small range of Young's modulus and density changes, a least squares fit could be applied to the change in maximum amplitude and dominant frequency response of the board with the corresponding changes in test parameters. Thus, in order to quantify the effects of varying Young's modulus and density on the strain dominant frequency and peak amplitude, relative change in each parameter was evaluated against the percent change in both strain frequency and amplitude, as shown in Figure 4.10 and Figure 4.11.

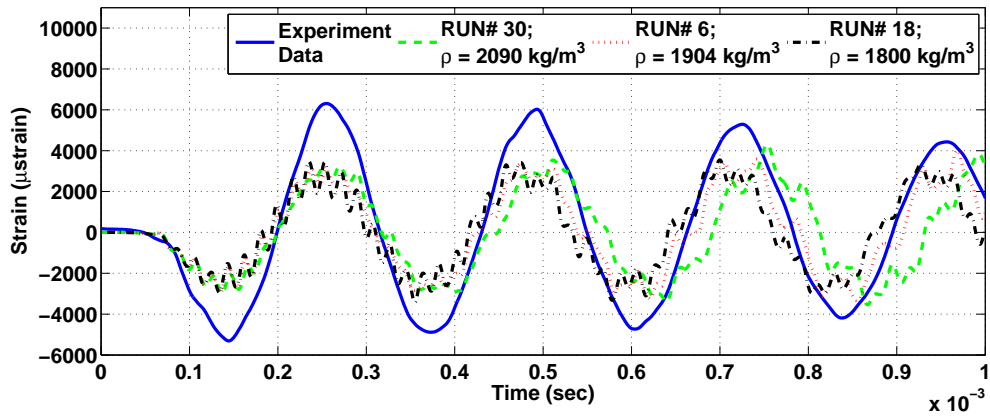


Figure 4.9: Effect of Density on Strain Response;  $E = 17.0000 \text{ GPa}$ , Tied Contact Type, Body-Driven BC

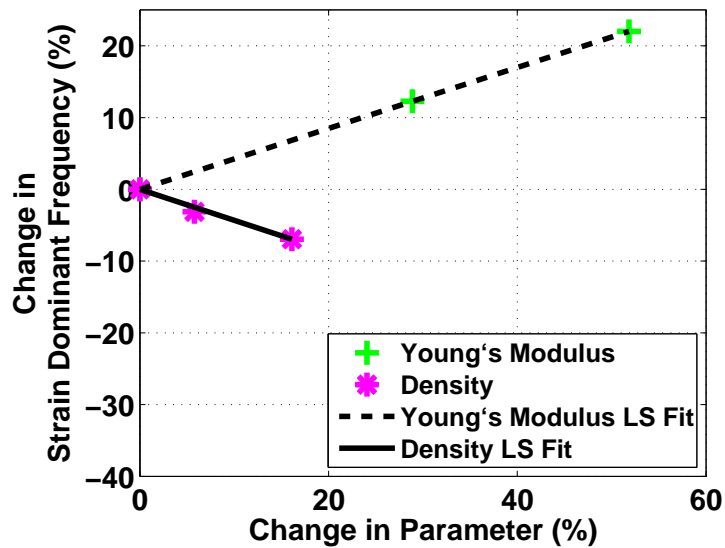


Figure 4.10: Linear Strain Dominant Frequency Sensitivity to Young's Modulus and Density

The relationships between the variations in assigned material properties and changes in both the dominant frequency and peak amplitudes were fairly linear. A 52% increase in

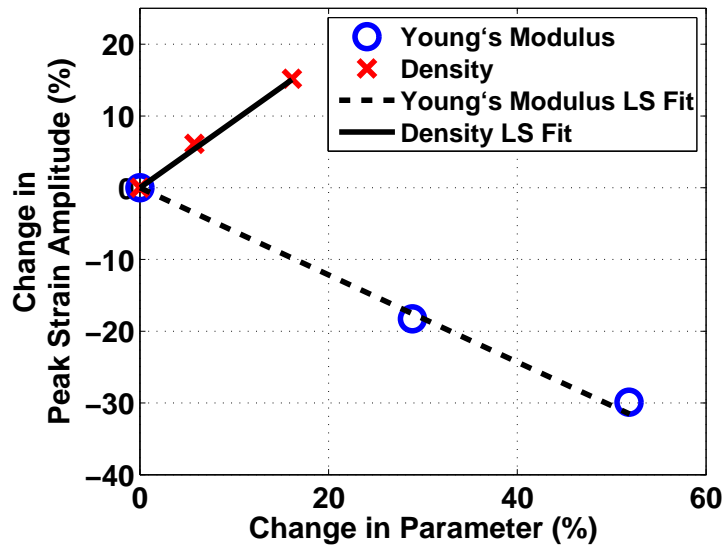


Figure 4.11: Linear Peak Strain Amplitude Sensitivity to Young's Modulus and Density

Young's modulus produced a nearly 32% reduction in maximum strain at the top surface of the board, while increasing the dominant frequency by over 22% from 4,214 Hz to 5,143 Hz. The effect of a density variation on the dynamic board response was also significant, especially for peak amplitude. A 16% increase in density produced a 15% increase in maximum strain at the top surface of the board, while reducing the dominant frequency by less than 7% from 4,859 Hz to 4,520 Hz.

The contact surfaces with varied friction coefficients as part of the run matrix, were designated as the contacts between the PCB and the fixture, on which the board rested, and between the PCB and the clamp, which held the board down during impact. The greatest effect of friction coefficient was observed between the two extremes, frictionless and tied contacts, and only with respect to the dominant frequency response, as seen in Figure 4.12. As mentioned earlier, some medium frequency oscillations, which were at least partly a result of reduced effect of clamp oscillations normal to the YZ plane, were greatly reduced for the frictionless contact. While tied and frictionless contact surface parameters affected

the board oscillation frequency after the impact, no significant effect was observed between the  $\mu = 0.5$ ,  $\mu = 0.3$  and frictionless friction coefficients at the PCB contacts on neither the strain amplitude, nor on the dominant frequency response.

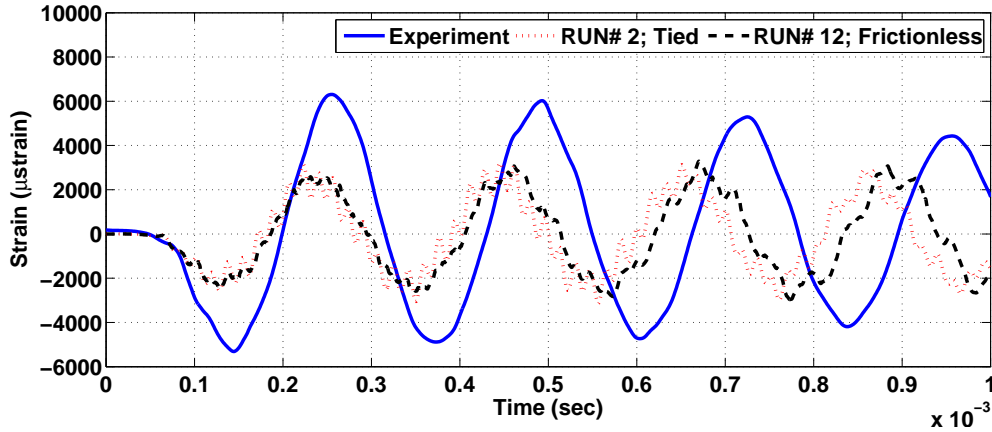


Figure 4.12: Tied vs. Frictionless Contact;  $E = 21.9115$  GPa,  $\rho = 1,904$  kg/m<sup>3</sup>, Body-Driven BC

The sensitivity analysis of the board strain response to the elastic modulus, density, contact type and experimentally derived boundary conditions using finite element model has confirmed a nearly exact dominant frequency match compared to the measured strain in the laboratory. However, the peak amplitude of the board strain has not yet been simulated as effectively as the frequency response. Decreasing the modulus of elasticity to increase the peak amplitude to the measured levels, while maintaining the same dominant frequency with the reduction in density, would require both parameters to reach unphysical levels. Since the acceleration profile would have the greatest effect on the maximum strain amplitude, and was constant for all the cases in the run matrix, a change in the acceleration profile, which was related to the accelerometer data, was attempted in order to increase the peak strain amplitude.

In an attempt to increase the peak strain amplitude response, a half-sine input method was used for one computational run. Due to the fact that body-driven acceleration profiles produced more representative strain responses with reduced medium frequency oscillations, the body-driven input method was used for the half-sine acceleration boundary condition calculation. Doubling the amount of change in velocity of the initial impact pulse to  $\Delta V = 13.48$  m/s over the same pulse duration of 0.1 milliseconds, thus increasing the peak acceleration to 22,760 g, shown in Figure 4.5, produced a near exact match to the measured maximum strain, as seen in Figure 4.13.

Applying the half-sine acceleration profile as the boundary condition to the linear elastic model resulted in a very close agreement between the computational dynamic board response and the measured strain in both amplitude and frequency. Also, the sensitivity of the strain amplitude and dominant frequency to the elasticity modulus, density, contact surface friction coefficient and boundary condition types (body or surface-driven), is the same under both the experimentally measured and the more academic, half-sine acceleration profiles. Additionally, even with the “clean” half-sine acceleration profile, high frequency oscillations were much smaller, but were still observable in both the computational predictions and laboratory measurements, as seen in the close-up of the time domain plot in Figure 4.14 and in the frequency domain plot in Figure 4.15. The presence of high frequency oscillations in both laboratory and computational model suggests that they were likely a result of a physical phenomenon, such as clamp movement normal to the YZ plane during impact as mentioned earlier, and thus dampened out quickly, especially when the contact surface coefficient between the PCB and steel was reduced. The fact that high frequency oscillations were most likely present due to the movement of the clamps normal to YZ plane could also help explain the reduction in high frequency oscillations with the increase in torque of the steel screws that held the clamps to the fixture.

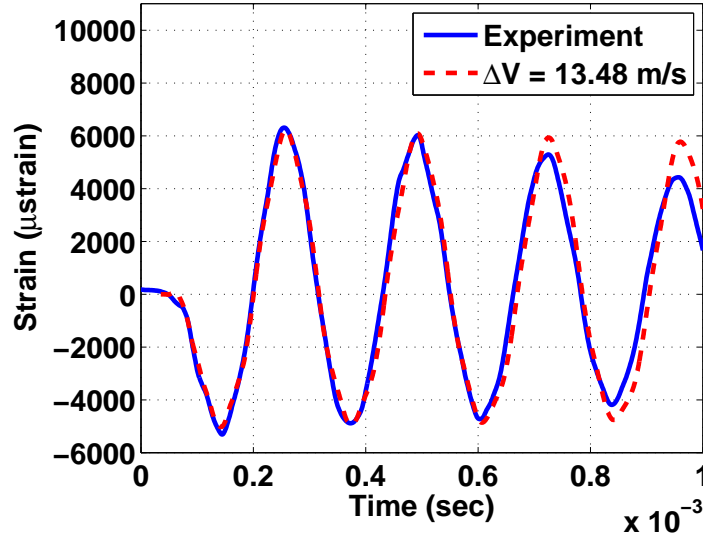


Figure 4.13: Strain Response to Half-Sine Acceleration Profile;  $E = 17.0000 \text{ GPa}$ ,  $\rho = 2,090 \text{ kg/m}^3$ , Tied Contact, Body-Driven BC

The only apparent limitation of the current computational model that predicts the dynamic board response to high-g impact mechanical stresses seemed to be the lack of dampening present in the linear elastic material model compared to the strain measured in the laboratory, as evidenced by the low peak strain amplitude decay rate shown seen in Figure 4.13. While low peak strain amplitude decay rate may be addressed by adding artificial viscosity to an Eulerian or Arbitrary Lagrangian-Eulerian (ALE) frames of reference, the current study was conducted in a purely Lagrangian frame of reference and no damping factors were available in the ALEGRA-EMMA code to simulate possible effects of friction losses or aerodynamic drag experienced in the laboratory. However, as long as the significant board dynamics parameters are accurately predicted, which has been proven in this section by closely correlating the computational strain oscillation amplitude and frequency at the top center of the PCB with the experimentally obtained strain gage data during unique high-g impact mechanical stresses, the computational board

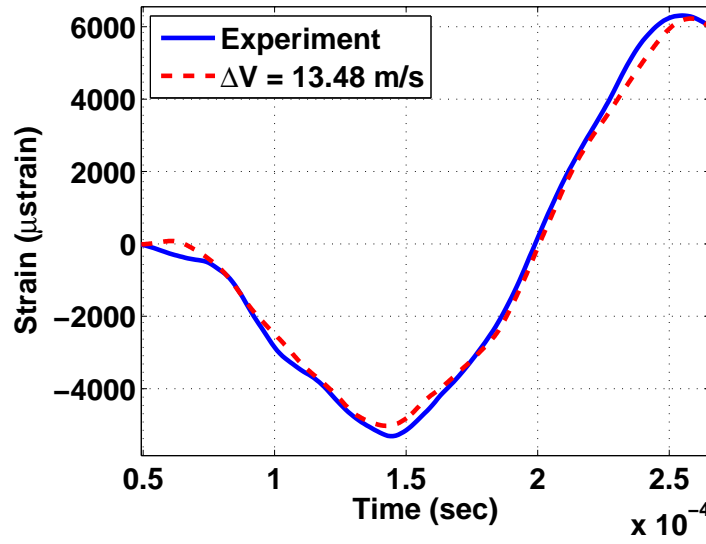


Figure 4.14: Close-up of Strain Response to Half-Sine Acceleration Profile;  
 $E = 17.0000 \text{ GPa}$ ,  $\rho = 2,090 \text{ kg/m}^3$ , Tied Contact, Body-Driven BC

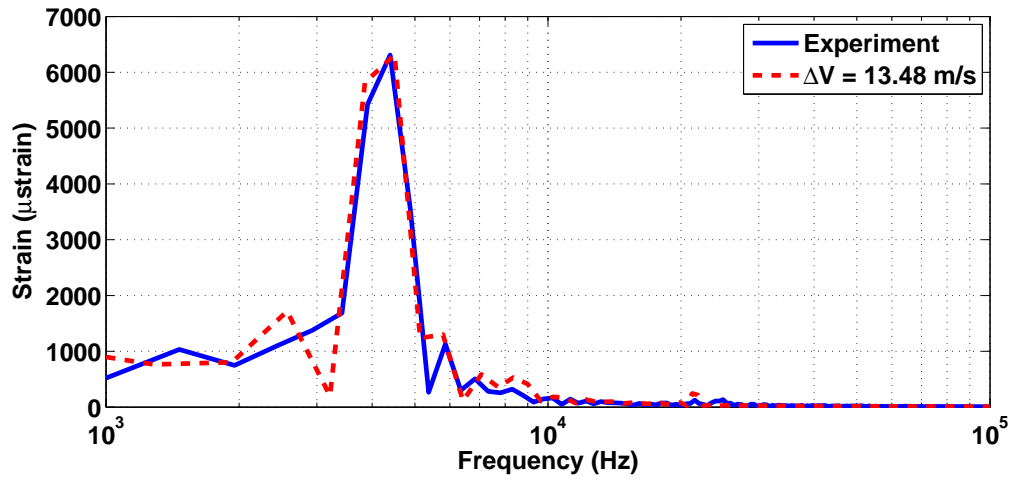


Figure 4.15: Half-sine Acceleration Profile Strain Response FFT;  $E = 17.0000 \text{ GPa}$ ,  
 $\rho = 2090 \text{ kg/m}^3$ , Tied Contact, Body-Driven BC



dynamics model developed here may be used for calculating the boundary conditions imposed on capacitors surface-mounted at different locations on the flexing boards. Unfortunately, while application of the half-sine integrated acceleration profile, or at least filtered accelerometer data might initially seem to be an ideal method to calculate the boundary conditions of stressed, surface-mounted components, the highly important post-impact acceleration waveforms that would not be otherwise captured using such methods, require the use of raw and unfiltered accelerometer data when obtaining mechanical stresses imposed on flexing board capacitors. Therefore, due to the importance of using accurate mechanical loads for boundary conditions when obtaining the piezoelectric response in the following sections, the high-g impact loads on the capacitors soldered to flexing and non-flexing boards were calculated based on the directly applied and unfiltered accelerometer data profiles.

As discussed in Chapter 2, studies describing dynamic printed circuit board response to drop impact acceleration profiles significantly greater than 3,000 g have been almost non-existent in literature. However, in order to predict electromechanical response of components such as capacitors mounted on the PCBs exposed to high-g mechanical stresses on the order of 20,000 g, an accurate board dynamics computational model predicting boundary conditions at different locations on the board surface first had to be developed. Thus, out of necessity for accurately calculating the conditions to which surface-mounted components are exposed, a computational PCB dynamics model of an ISOLA 370HR printed circuit board, exposed to high-g drop impacts an order of magnitude higher than those specified in the JEDEC standards, was successfully developed for the first time and validated against the experimentally obtained data. The successful computational model accurately simulating the dynamic board strain response, developed as a result of the computational parametric study described in this section, was used to calculate

acceleration profiles, which were later applied as boundary conditions when predicting the electromechanical response of capacitors mounted on the flexing boards.

## **4.2 Phase II: Capacitance Response and SEM Measurements**

The next phase of research was devoted to measuring capacitance changes due to high-g mechanical shocks of high and low voltage capacitors, with ferroelectric dielectric materials for their insulators, using the same drop tower employed to develop and validate the computational board dynamics model in Section 4.1. The experimental capacitance change results obtained during Phase II, were used to validate the computational piezoelectric model predicting the electromechanical response of the Barium Titanate to mechanical loads in Phase III. Also, during Phase II, MLCC electrode layout dimensions were measured and capacitor materials were identified using the Scanning Electron Microscope SEM with EDS capability. Combination of high voltage capacitor testing, as well as the SEM imagery of mechanically stressed specimens confirmed the mechanical mode of failure of capacitors surface-mounted on the flexing boards, while experimentally observed changes in capacitance of low voltage components, which were simultaneously electrically stressed during the drop, validated the presence of an electromechanical response predicted by the computational model that was developed in Phase III. While the main focus of the current research was on the piezoelectric response of ferroelectric ceramics under mechanical stress, it is still appropriate to address the mechanical failure modes observed during the impacts as is accomplished in the next subsection.

### ***4.2.1 Mechanical Mode of Failure.***

Possibly, the most important fact to note when describing the mechanical modes of failure of capacitors observed throughout the drop impact test series is that absolutely no complete, or even partial failures occurred in the non-flexing board configuration, but overwhelmingly, only flexural mode of failure was observed in the components that were mounted on the boards that were allowed to oscillate after the impact. Furthermore,

during the low voltage capacitor drop tests, where a total of 156 connections of 1210-size capacitors were tested in the flexing board configuration from heights generating peak accelerations ranging from 2,958 g to 18,487 g, 100% of mechanical failures were due to the flexural mode. The flexural failure mode, as discussed in Chapter 2, was where the dielectric material fractures near the terminal and often propagates the crack through a certain number of electrodes, and a portion of the terminals that contain solder, as shown in Figure 4.16.

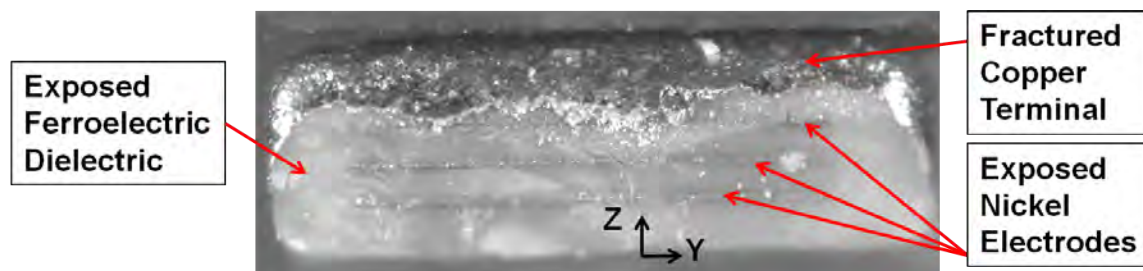


Figure 4.16: 1210-size Capacitor Flexural Mode of Failure

While every 1210-size capacitor survived all the 36-inch height drops, which resulted in a maximum strain of approximately 6,300  $\mu$ strains and peak acceleration of up to 8,356 g, out of 93 solder connections for the 1812-size, high voltage capacitors, failure rate was near 38% on the boards that were dropped from 36 inches. The vast majority of 1812-size component failures, approximately 91%, were also due to the flexural mode of failure, where during board oscillations, dielectric ceramic and the terminal metal were fractured. The remaining 9% of connection failures of the high voltage capacitors were due to pad cratering, but only after the opposing side of the component first separated via the flexural failure mode, as shown in Figure 4.17. Just as with the 1210-size capacitors, the larger, 1812-size components, exhibited no mechanical failures in the non-flexing board

configuration under multiple drops and harsher mechanical shocks on the order of almost 24,000 g.

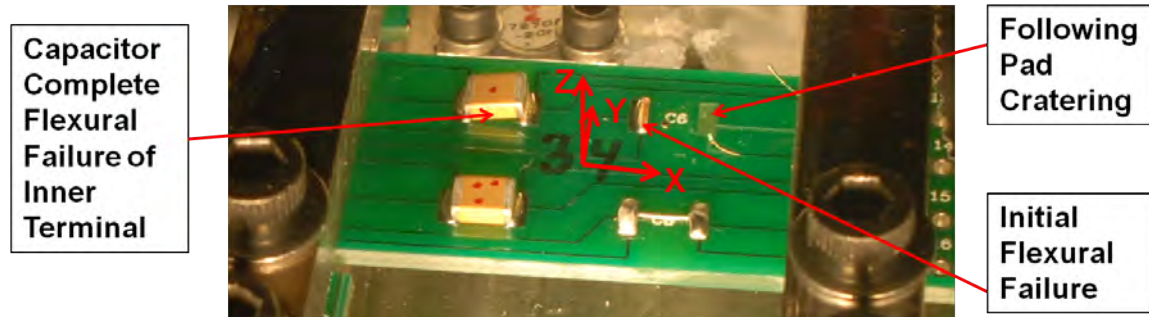


Figure 4.17: 1812-size Capacitor Flexural Modes of Failure

While high voltage capacitor connections began failing in the flexing board configurations starting from drop heights of 36 inches and the first observed failures of the smaller, low voltage capacitor connections began at 42-inch drop heights, because the focus of the study was on the electromechanical response of capacitors, not enough statistically significant experimental data was collected in order to establish a clear quantitative relationship between the component size, peak acceleration, strain or drop height, and mechanical failure rate. The only definitive correlation was observed between the drop configuration (flexing or non-flexing) and the mechanical mode of failure. Specifically, the relationship between the discrete changes in capacitance, indicative of partial contact loss of series capacitor electrodes, and printed circuit board oscillation frequency post impact was identified during the RC method capacitance measurements, and confirmed with the impedance analyzer data, SEM images and high speed video for both low and high voltage capacitor experiments.

When measuring the capacitance with the RC method described in Chapter 3, it is important to note that the total capacitance measured with this technique included additional capacitance of the wire carrying the charge/discharge pulse from the wave

generators. For the high voltage capacitors, capacitance of the wire was approximately 500 pF, and for the high voltage capacitor experiments, the value hovered around 600 pF. The exact wire capacitance value varied with every change in the circuit board, because it required cutting the leads by approximately half a centimeter every time the boards were replaced. However, because only changes in capacitance needed to be detected during the drop, the additional wire capacitance was not a factor, and only presented itself as a capacitor in parallel with the MLCC under test. Therefore, all the capacitance values measured with the dynamic RC method and presented in the following sections exhibit an additional 500 - 600 pF capacitance and a residual capacitance of the same value after complete separation of capacitors post impact.

In the case of the floating electrode capacitors, as discussed in Section 2.1.1, mechanical fracture of the dielectric results in a open, which effectively reduces capacitance of the device by a discrete value related to the fraction between electrodes with lost electrical contact with the terminal and the total number of electrodes in the capacitor. Both partial and complete flexural failure of the series capacitors were clearly observed during the experiments with the high voltage devices. For example, reviewing the high-speed video of a particular 36-inch drop of the flexing board during the high voltage capacitor measurements confirmed no visible mechanical failures or fractures of the RC monitored component on station C5 during the initial impact of the anvil, or while the board was oscillating immediately after the shock. However, capacitance measurements during the drop, uncovered discrete capacitance oscillations between the initial value of 1,000 pF and the final capacitance of 910 pF, directly coinciding in frequency with the board strain oscillations, as seen in Figure 4.18.

SEM imagery of certain high voltage capacitors, which were dropped in the flexing board configuration, but did not completely separate from the pad, revealed a separation of up to three electrodes from the terminal at the interface between the terminal and the

dielectric material, due to the crack that resulted from excessive stresses and strains during the impact, as seen in Figure 4.19. Thus, similar partial dielectric and electrode separations from the terminal, as shown in Figure 4.19, could explain the discrete capacitance changes observed in Figure 4.18, confirming the partial flexural mode of failure of the flexing board capacitors.

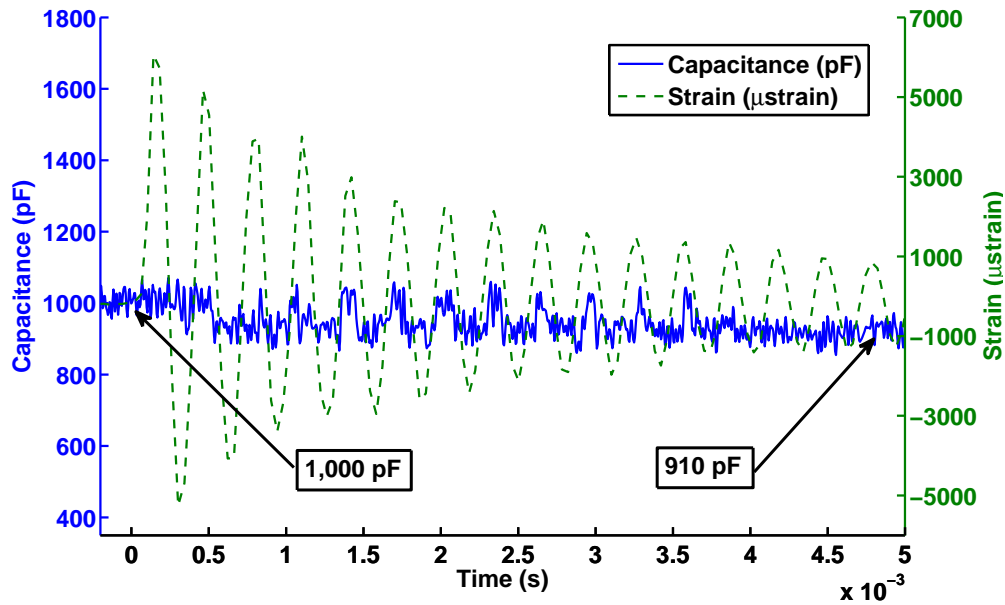


Figure 4.18: 1812-size Capacitor Discrete Capacitance Oscillations due to Flexural Mode of Failure Correlating in Frequency to Board Strain Oscillations

The high speed video reviewed during the subsequent 36-inch drop of the same capacitors, which were represented by the discrete capacitance oscillations in Figure 4.18, revealed an inner terminal separation from the copper pad, and then a last momentary contact as the board was flexing post impact, before a complete mechanical failure. Even more intriguing, is the fact that the RC measurement technique was able to detect an increase in capacitance to the pre-stressed value of 1,000 pF, as well as identify the exact time when the momentary contact due to board flexure occurred, before complete

mechanical failure of the device, as seen in Figure 4.20. SEM imagery of the failed capacitor, which was recovered after the drop and placed back near its location of mechanical failure, revealed a dielectric ceramic fracture that propagated completely through two electrodes and the terminal, as shown in Figure 4.21. Finally, the impedance analyzer capacitance measurements of stressed components, which were either dismantled from the board or recovered post impact according to procedures outlined in Section 3.2.3, also confirmed the discrete capacitance nature of the failed series capacitors, as seen in Figure 4.22, when the terminal is partly separated from the dielectric material, and subsequently, from the electrodes, as previously shown in Figure 4.16.

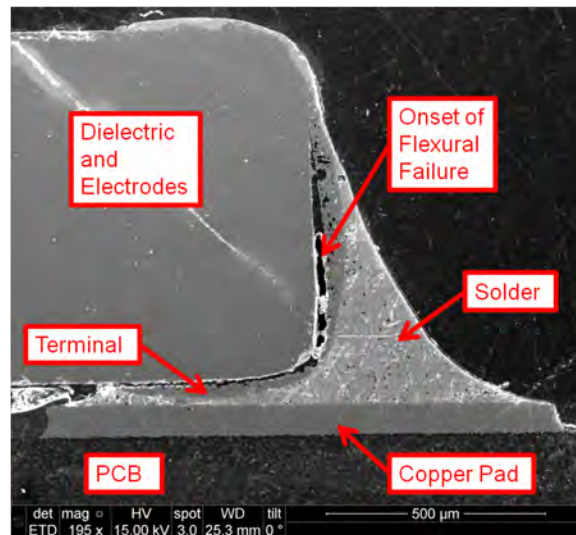


Figure 4.19: Fracture Propagation due to Flexural Stresses Resulting in Partial Separation of Electrodes From the Terminal

The low voltage capacitor experiments also exhibited flexural mode of failure, as shown in Figure 4.23, but just as with the larger, 1812 size capacitors, 1210 size devices also failed mechanically only in flexing board configurations. While smaller capacitors failed during the drops with slightly higher peak accelerations, discrete, oscillatory capacitance

changes occurred at the same frequency as the board strain oscillations, pointing to the fact that failure mechanisms in both high and low voltage capacitors were similar. However, the slight increase in capacitance before discrete oscillations observed in Figure 4.23, was due to the electromechanical response of the simultaneously electrically stressed dielectric material, as opposed to reestablished contact between separated electrodes and terminals.

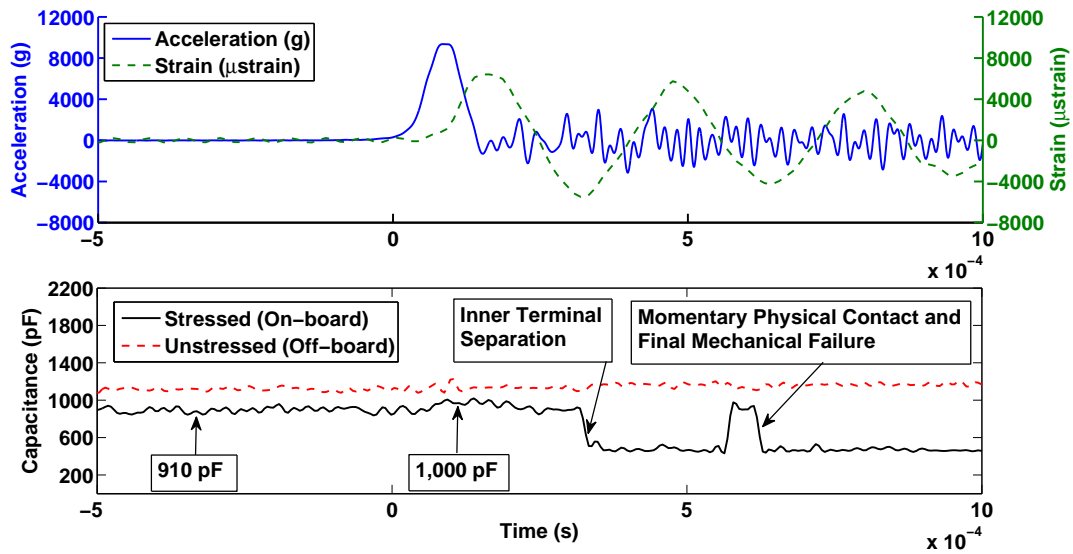


Figure 4.20: Capacitance Increase due to Recontact with Electrodes, Intermittent Contact of Capacitor with the Pad and Final Separation from the Flexing Board of 1812 Capacitor after 36-inch Drop

Oscillations and intermittent contacts displayed in Figure 4.23 and Figure 4.20 point to the fact that the mechanical failure modes of capacitors exposed to high-g drop shocks follow closely the stages of component failure illustrated by Luan in Figure 2.13 and Figure 2.14, and described in Section 2.4 [40]. However, it is only for the first time that



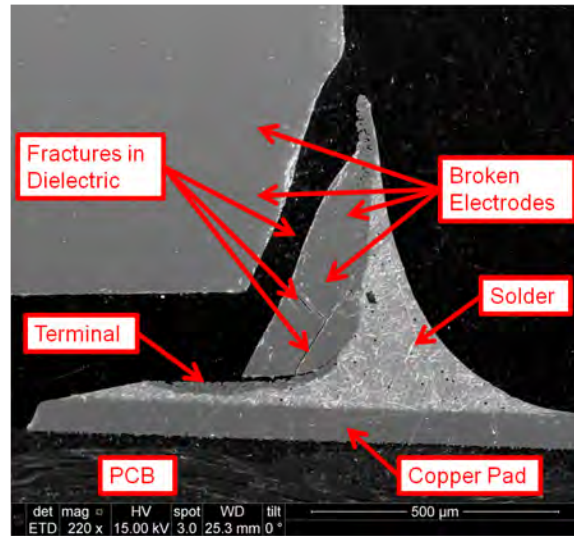


Figure 4.21: Dielectric Fracture Propagation Due to Flexural Stresses Resulting in Complete Flexural Mechanical Failure

the correlation between discrete capacitance and flexing board strain oscillations has been confirmed anywhere in literature for capacitors exposed to high-g impacts on the order of 10,000 g and greater. Furthermore, unlike resistor failure, which is binary and based on either total electrical contact or separation, series MLCC can exhibit partial loss of capacitance based on the number of electrodes in contact with the terminal.

A clear correlation between board oscillation frequency post impact and discrete capacitance measurements due to intermittent electrode separation from the terminals, points to the fact that the mechanical, flexural mode of failure, is still extremely important when predicting reliability of surface-mounted electronics. Also, the fact that no capacitors in the non-flexing board configuration even partially failed during the drops, points to the conclusion that the mechanical mode of failure is much more closely related to the strain and strain rates generated from the oscillations of the PCB, rather than to the maximum acceleration, or even the total change in velocity to which the test articles were exposed. Hence, if board flexure can be prevented during high-g impacts, flexural mode of

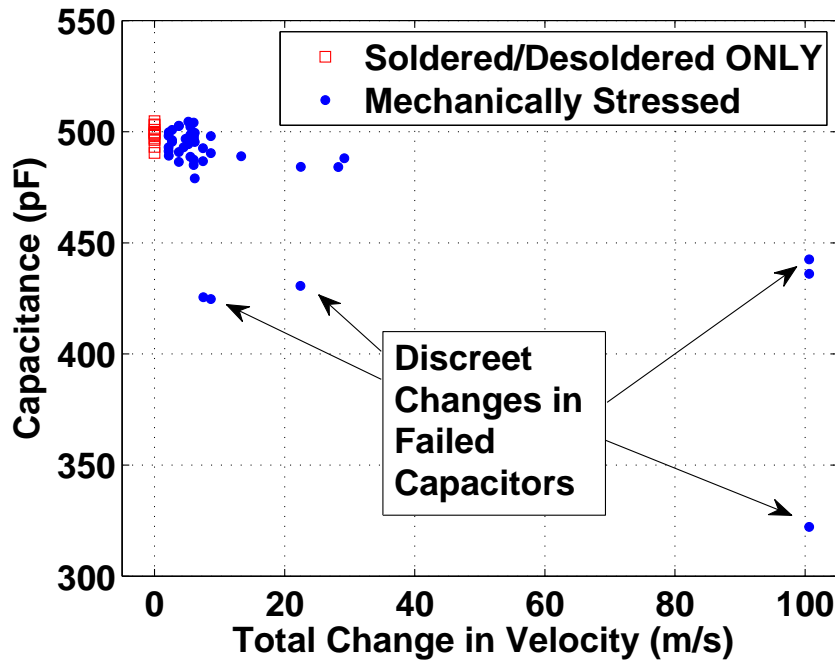


Figure 4.22: Discrete Changes in Capacitance of Mechanically Failed Devices Measured Using Impedance Analyzer at 100 KHz

mechanical failure could possibly be delayed by at least a 94% increase in peak acceleration from 11,670 g to 22,594 g, as tested in the laboratory for low voltage capacitors. Even though higher peak accelerations for the non-flexing board configurations may be possible, they were not tested due to the limitations with the drop tower, and because, as mentioned earlier, the focus of research was on the electromechanical response predictions.

#### 4.2.2 Experimentally Measured Electromechanical Response.

While it may be possible to prevent mechanical failure and keep the components physically intact during the shock by applying techniques that prevent or reduce board flexure, a significant electromechanical response of ferroelectric ceramic capacitors may still be evoked during drop impacts. In fact, observable piezoelectric response of ferroelectric series multi-layer capacitors was detected using the RC method during non-

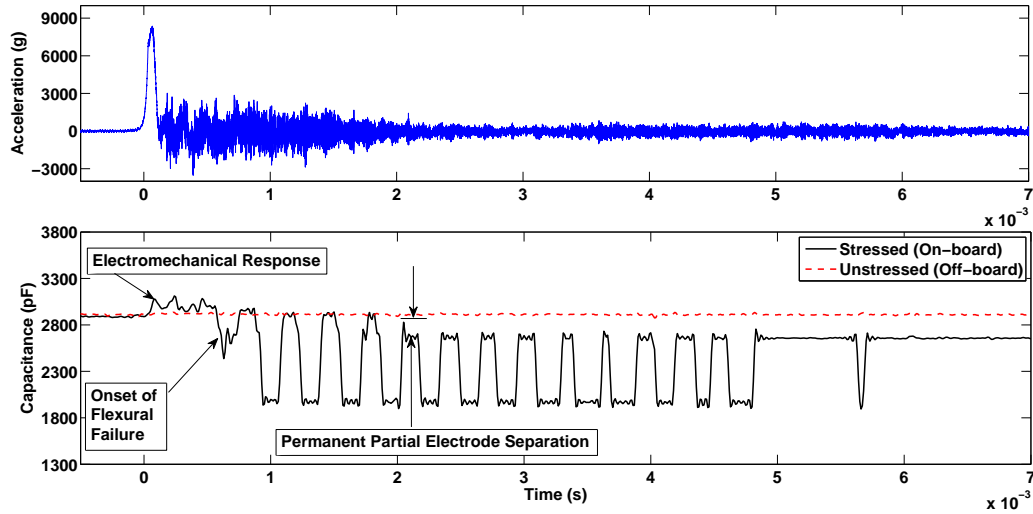


Figure 4.23: Capacitance Increase due to Electromechanical Response and Intermittent Contact of Electrodes with the Terminal of Flexing Board 1210 Capacitor After 36-inch Drop

flexing board configuration impacts with maximum accelerations as low as 3,000 g. Thus, the electromechanical response of capacitors, which was observed in the laboratory is discussed in this subsection.

The important point to realize is that the electromechanical response can be evoked with mechanical stress only if the capacitor being shocked is simultaneously electrically charged. Even if the dielectric material of the capacitor is ferroelectric, piezoelectric properties will be evident only when enough potential is applied between the electrodes, and the randomly polarized domains of the ferroelectric ceramic are aligned under the influence of the electric field. Due to the  $9 V_{rms}$  limit of the oscilloscope used to measure the potential across the capacitors during the impact, as well as the 10 V limit of the function generators, which were used to create the charge/discharge pulse, high voltage capacitors were electrically charged through less than 0.3% of their 3,000 VDC rating. Not surprisingly, throughout the 60 total drops of high voltage capacitors, which were

confirmed to have Barium Titanate-based ceramic dielectric, none of the devices exhibited a measurable piezoelectric response to the mechanical shock stresses in either flexing or non-flexing board configurations with maximum acceleration peaks of up to 23,961 g. However, during low voltage (10 VDC) capacitor tests, which simultaneously exercised devices through 80% of their rated voltage with the +1/+9 Volt square pulse, a significant electromechanical response of capacitors was measured with the RC technique in the laboratory. Therefore, when discussing the electromechanical response of capacitors for the remainder of this chapter, which explains both experimental and computational results of the current research, it is addressed only in the context of the tested low voltage capacitors. Furthermore, only low voltage, 1210-size capacitors, were computationally modeled, and only their piezoelectric response to drop impact was validated with the capacitance variation data obtained during the drop tower experiments.

The electrode layout of the low voltage, 1210-size capacitors, has already been illustrated in Figure 3.14 and the dimensions of the inner structure of the MLCC were measured using the SEM imagery of the bisected devices. Also, analysis of the energy dispersive spectroscopy, seen in Figure 4.24, showed that the dielectric material for the floating electrode multi-layer ceramic capacitors was clearly based on Barium Titanate ( $\text{BaTiO}_3$ ). The  $L \alpha$  energy of 4.465 keV for Barium was close to the  $K \alpha$  energy of 4.510 keV for Titanium. However, based on the energy counts when using the 15 keV energy beam, and the fact that for every Titanium atom there were approximately 6 Oxygen and 8 Barium atoms, proved that the composition of the dielectric ceramic inside the capacitors was based primarily on the Perovskite structure of the Barium Titanate material. Similar analysis of the capacitors identified Nickel metal for electrode material and Copper for the capacitor terminals. Finally, in addition to capacitor material characterization, solder was identified to be the 37% Lead and 63% Tin compound, mounting PCB pads

were determined to consists primarily of Copper, and the printed circuit board itself was confirmed to have been constructed primarily from Silica Carbide fibers.

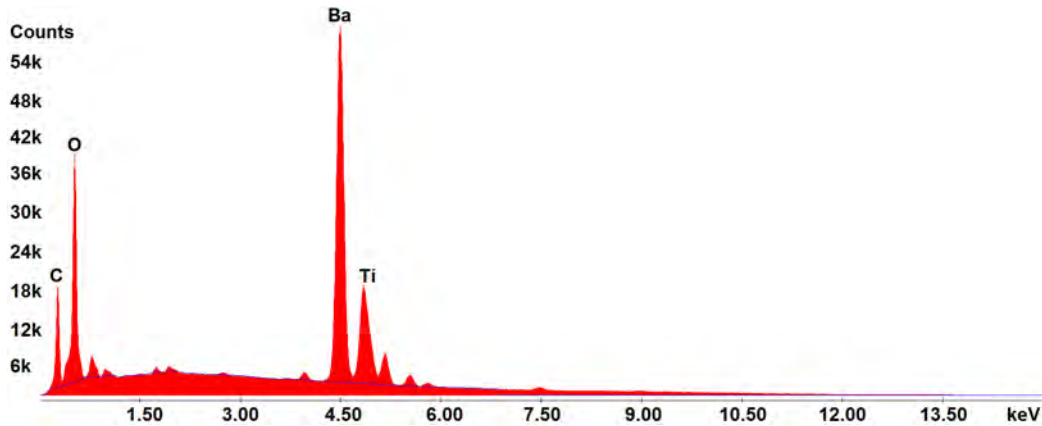


Figure 4.24: SEM Analysis of the Dielectric Material

Now that the dielectric material has been confirmed to consist of the ferroelectric Barium Titanate, electromechanical response of the capacitors could be attributed definitively to the piezoelectric effects during the shock, as long the devices are simultaneously electrically stressed. Using the RC method, capacitance variations induced by the mechanical stress were detected during the drop experiments in the flexing board configurations of low voltage capacitors, as seen in Figure 4.25. The acceleration profiles, board strain responses and capacitance measurements displayed in Figure 4.25 were based on four separate impacts, each conducted using a different circuit board in the A1, flexing configuration. Therefore, capacitance, which was measured during the impact, was conducted on separate, previously un-shocked capacitors. Board strain for each of the drops in Figure 4.25 was based on the strain responses of the PCB drops from exactly the same respective drop heights, but measured 9 drops earlier.

There are a few findings regarding the change in capacitance of mechanically stressed devices mounted on flexing board, displayed in Figure 4.25, that are worthy of mention.

First, not every drop shock generated a significant electromechanical response that was measurable using the RC method in the flexing board configuration. For example, the 18-inch drop, which generated an acceleration profile with a peak of 2,958 g and maximum strain of 2,061  $\mu$ strains, evoked no measurable change in capacitance. However, when the electromechanical response was detected, piezoelectric effects always resulted in an increase in capacitance, but not in a linear fashion. For example, increasing the mechanical stress from 4,831 g peak acceleration during the 24-inch drop to 8,356 g during the 36-inch height impact, resulted in a transitory maximum increase in capacitance of 203 pF (9.2% based on the nominal value of 2,200 pF) and 222 pF (10.1%) during each respective shock, behaving more like a step function, rather than a linear relationship. Also, although not easily identifiable, capacitance changes followed an oscillatory, cyclical increases, that closely matched the board strain oscillations in frequency, pointing to the fact that such variations were a result of a piezoelectric effect. At least until the onset of the flexural failure displayed in Figure 4.23, the electromechanical response during the 30-inch and 36-inch drops was oscillatory in frequency and positive in magnitude, as will be more clearly evident when comparing results in Figure 4.25 with the predictions of the computational model in the next section. While the absence of capacitance increase during the 18-inch drop can be explained by the coincidental discharge pulse timing at the exact moment of the impact, effectively nulling the piezoelectric response by aligning the discharged state of the capacitor with the instant the mechanical stress was applied, the non-linear relationship between peak acceleration and change in capacitance of devices in the flexing board configuration, suggests a more complex set of mechanisms affecting the magnitude of the electromechanical response that will have to be addressed later in the chapter, when comparing computational model behavior to the experimentally obtained data.

The non-flexing, B configuration of the board, produced a more linear relationship between the peak acceleration and capacitance change of ferroelectric dielectric capacitors.

As can be seen in Figure 4.26, the lower the initial impact and the lower the secondary vibration effects, the proportionally smaller the capacitance change in magnitude, which is starkly different from flexing board configuration drops. Another difference between the varying board configuration drops was the higher piezoelectric sensitivity of the flexing board capacitors, possibly due to the additional degrees of freedom induced during the board flexure. For example, a 30-inch drop of the flexing board configuration produced a 221 pF (10.0%) increase in capacitance, while a similar 30-inch drop of the non-flexing board resulted only in a 36 pF (1.6%) change.

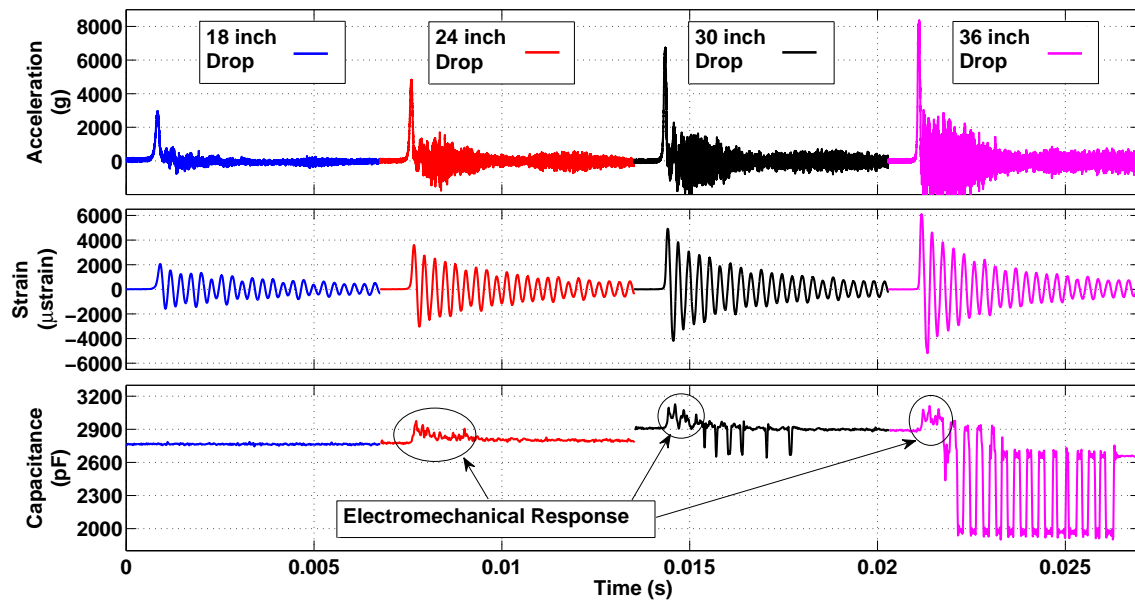


Figure 4.25: Electromechanical Response of Capacitors Mounted on the Flexing Boards

However, there were similarities in capacitance responses between different board configuration capacitors. One similarity was the fact that the capacitance response waveform was directly related to the acceleration profile at the locations where the components were soldered. For example, the board strain during the impact of the flexing boards produced oscillatory mechanical stresses at the copper pads, generating an

oscillatory capacitance response described earlier and illustrated in Figure 4.25. While the acceleration profiles of the non-flexing board capacitors were completely different, and featured non-oscillatory initial impact effects and post shock vibrations, they still generated capacitance changes that were closely related to the mechanical stresses to which the capacitors were exposed, thus underscoring the need for accurate acceleration profiles when predicting the electromechanical response.

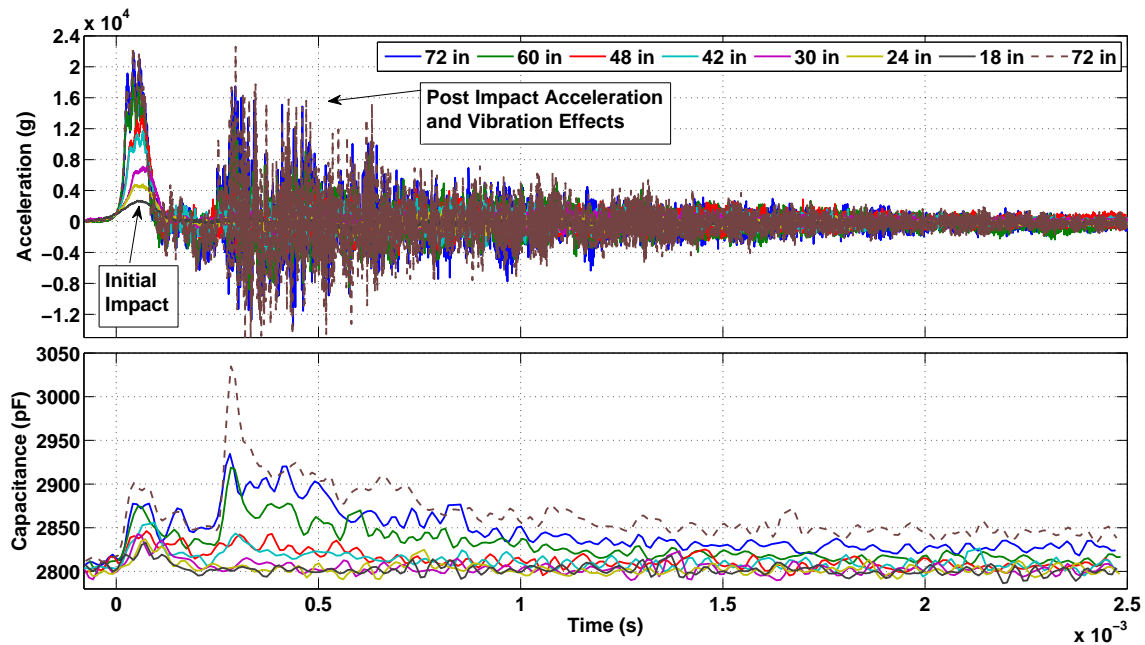


Figure 4.26: Electromechanical Response of Capacitors Mounted on the Non-Flexing Boards

Also, just as in the case of the flexing boards, some of the non-flexing board configuration impacts did not produce any measurable electromechanical response. For example, out of the ten total times that the same exact board, and thus capacitors, were dropped sequentially from heights ranging from 72 to 12 inches, only seven impacts produced a piezoelectric effect, evidenced by the increase in capacitance proportional



to acceleration and displayed by the first seven data series plots using solid lines in Figure 4.26. Drop tests from 66, 54 and 36 inches did not evoke a measurable capacitance response, and thus, were not plotted. Just as in the case of the flexing board configurations, the lack of observable electromechanical response was most likely due to the discharge pulse at the time of the initial impact, preventing alignment of the randomly polarized domains, and thus, nullifying the piezoelectric effects.

The last, single, 72-inch drop represented by the dashed line was conducted using a new board with previously unstressed capacitors. The two 72-inch drops displayed in Figure 4.26 were identical, but interestingly enough, produced different acceleration profiles, as well as capacitance responses. The difference in acceleration profiles may be explained by the impacted felt programmer material, addressed in Section 4.1, but the fact that both drops evoked significantly different capacitance responses points to the need to use accurate, unfiltered accelerometer data as the input boundary conditions for the computational models.

Another reason for using raw, unprocessed accelerometer data for boundary conditions when predicting electromechanical response, was the relative sensitivity of the capacitance to the initial and post impact accelerations. For example, during the 72-inch drop in the non-flexing board configuration, the initial impact peak acceleration was very close to the post impact vibrations detected by the accelerometer, but, as can be seen in Figure 4.27, the magnitude of the capacitance response to the post impact accelerations was significantly greater than to the initial impact, despite the fact that the duration of the high-g stresses during the shock was larger, resulting in the bulk of the change in velocity. However, when the post impact acceleration vibrations were significantly lower, 2,516 g, and less than half of the initial impact peak acceleration of 7,177 g, as observed during the 30-inch drop, the primary capacitance increase was due to the initial shock. The sensitivity of the capacitance to jerk, which is a time derivative of acceleration closely relating to pressure

inside the material, was another indication that electromechanical response was a result of a piezoelectric effect, and that the precise, and unprocessed boundary conditions must be used in the computational model that predicts changes in capacitance of ferroelectric dielectric capacitors under mechanical loads.

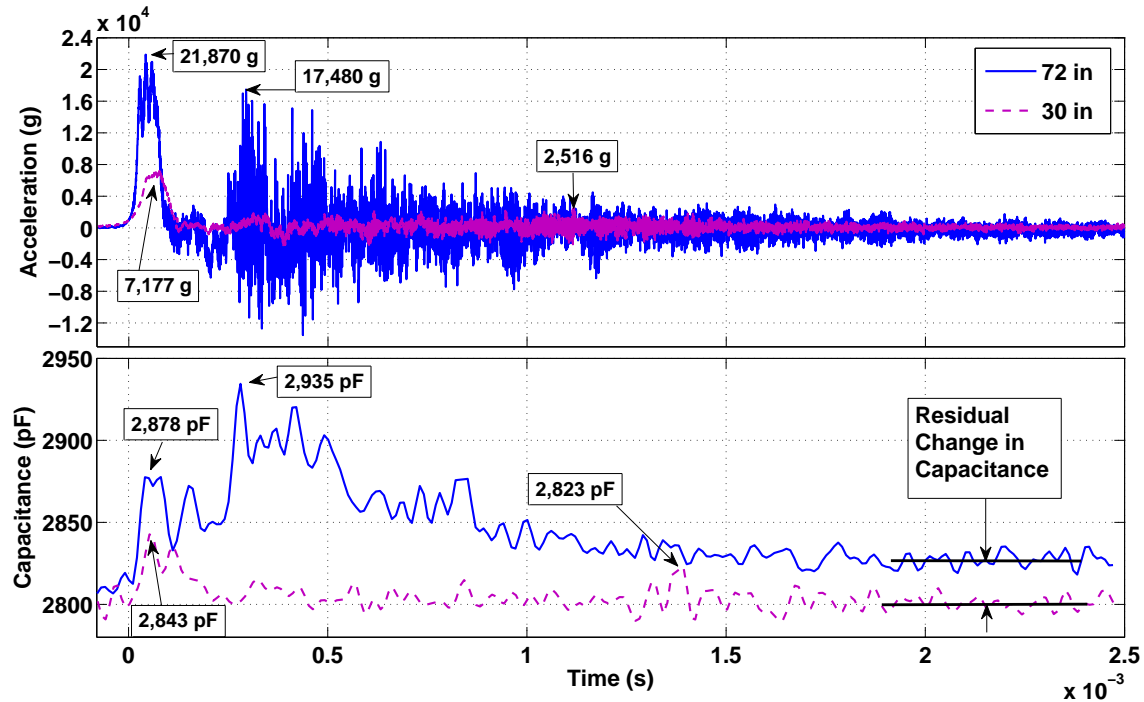


Figure 4.27: Electromechanical Response of 72-inch vs. 30-inch Height Drop Capacitors Mounted on the Non-Flexing Board

The last intriguing result of analysis of the experimentally gathered data shown in Figure 4.27 was the residual increase in capacitance during high drop heights, which did not decrease within milliseconds of the main impact. For example, 72-inch and 60-inch drops, which generated relatively high amplitude post impact vibrations, exhibited an approximately 1.4% (30 +/-0.5 pF) increase in capacitance even after the vast majority of the vibrations have significantly subsided within 2.5 milliseconds. The capacitance did eventually decrease to its original value of 2,800 pF, as evidenced by the pre-shocked

calculations of capacitance for the same exact device, which was dropped in the previous test run, but the oscilloscope could not detect the decrease in capacitance after the event due to the 10 millisecond time limit on the data acquisition duration at the high data rates required by the RC technique. While the exact reason for the long capacitance recovery times is unknown, the residual increase in capacitance was more pronounced in higher drop height experiments, which generated higher peak changes in capacitance, and thus, were probably related to longer charge dissipation duration, most likely exacerbated by the concurrent post impact vibrations.

During Phase II of research, experimental procedures outlined in Chapter 3 uncovered mechanical modes of failure of capacitors and gathered capacitance data, which was later used to validate the electromechanical response predicted by the computational model of the MLCC. The partial and complete flexural modes of failure observed during the drop of both low and high voltage capacitors in the flexing board configuration, point to the fact that the mechanical separation of surface mounted components is much more closely related to the strain and strain rates of the flexing PCB surface, than to the magnitude of the peak acceleration during high g drop impacts. Dynamic RC capacitance measurement method, SEM imagery of failed components and static impedance analyzer measurements were all crucial in determining the exact mechanical failure mechanisms. The fact that no mechanical failures were observed during multiple non-flexing board configuration shocks of up to 24,000 g, while every single surface mounted capacitor connection failed during board oscillations from drops generating 8,000 to 15,000 g in the flexing board configuration regardless of the size of the device, makes a strong case for using techniques such as potting, which attempt to increase the reliability of electronics packaging, and reduce board oscillations and flexure. However, preventing board flexure through the use of support structures or potting, addresses only part of the electronics reliability issues.

Observed electromechanical response of ferroelectric dielectric capacitors produced capacitance increases of up to 10% of the nominal value during the impact regardless of board dynamics. While the electromechanical response always seemed to increase the capacitance of the devices, such instabilities, particularly when the capacitors are simultaneously being electrically stressed, can lead to an excess amount of charge, which might later damage other circuitry components. Furthermore, while it is apparent that the electromechanical increase in capacitance is very closely related to both magnitude and waveform of the applied mechanical loads, the complex piezoelectric effect evoked during the shock, as evident from various loading conditions and post impact residual capacitance changes, requires the use of computational models to help predict electromechanical behavior and address the electrical reliability of devices in order to increase their reliability and the overall survivability of electronics. Thus, the efforts of Phase III in this research were focused on creating and validating a computational model of the MLCC that predicts electromechanical response of capacitors to a unique set of mechanical loads present during the high-g drop impacts, based on the previously gathered and analyzed experimental data.

#### **4.3 Phase III: Computational Electromechanical Response Model**

The main goal of Phase III of research was to create an accurate, experimentally validated, computational model predicting the electromechanical response of ferroelectric dielectric ceramic multi-layered capacitors and to develop quantitative, constitutive relationships between the mechanical stress and the capacitance value of the component. While the mechanical mode of failure discussed in the previous section is important in terms of component reliability, the focus of this research was primarily on modeling electromechanical response of devices. Thus, the piezoelectric model that was chosen for simulating the material properties of the ferroelectric ceramic under mechanical stress was optimized for calculating variables pertinent to the electromechanical response, such as permittivity of Barium Titanate, as opposed to modeling the mechanical break up of the

components. In fact, ALEGRA-EMMA did not have the necessary tools, such as CZM or XFEM to accurately predict crack initiation and propagation through the material.

Since the focus of the current study was on calculating the piezoelectric response of ferroelectric ceramics, only the drop tests that produced observable variations in capacitance in the laboratory were computationally modeled. The only experimental data to which the comparison of the computational capacitor sub-model results could be made, were the three flexing board drops displayed in Figure 4.25 and the eight non-flexing board configuration impacts in Figure 4.26, discussed in Section 4.2. Therefore, computational runs of low voltage capacitor sub-model that was developed and mechanically stressed using boundary conditions measured directly by the accelerometer during each individual test, are identified in a matrix in Table 4.2.

Table 4.2: Computational Run Matrix to Calculate Electromechanical Response of Low Voltage Capacitors (“Drop #” Below Corresponds to Experimental “Test #” in Table 3.2)

| <b>Drop #</b>      | <b>17</b>  | <b>18</b> | <b>19</b> | <b>20</b>      | <b>22</b> | <b>24</b> | <b>25</b> | <b>27</b> | <b>28</b> | <b>29</b> | <b>31</b> |
|--------------------|------------|-----------|-----------|----------------|-----------|-----------|-----------|-----------|-----------|-----------|-----------|
| Drop Height (in)   | 24         | 30        | 36        | 72             | 60        | 48        | 42        | 30        | 24        | 18        | 72        |
| Peak Accel. (g)    | 4,831      | 6,744     | 8,356     | 21,874         | 18,487    | 13,702    | 11,670    | 7,177     | 4,833     | 2,698     | 22,594    |
| Mesh Type (C or F) | C          | C         | C         | C              | C, F      | C         | C         | C         | C         | C         | C         |
| PCB Config.        | A, Flexing |           |           | B, Non-flexing |           |           |           |           |           |           |           |
| Sim. Time (s)      | 0.004      |           |           | 0.0025         |           |           |           |           |           |           |           |

As discussed in Section 2.1 and shown in Equation (2.7), the only parameters that significantly affected capacitance of the device, assuming a constant number of electrodes in the MLCC, are the area of the overlapping electrodes, distance between the opposing charge plates and the permittivity of the dielectric in the direction normal to the electrode

material. Therefore, any significant change in capacitance, such as the 10% increase in value observed after the drop impact in the laboratory could only be explained by the combination of the variation of the overlapping electrode area  $A$ , dielectric thickness  $d$ , and permittivity  $\epsilon = \epsilon_0 K$ , where  $K$  is the dielectric constant. For the three flexing board configuration drops, the measured accelerometer data for each event was first applied as input to the board dynamic model developed in Section 4.1 and the acceleration profiles in the  $x$ ,  $y$  and  $z$  directions, calculated at the surface locations where the capacitors were soldered, were later applied to the capacitor sub-model to calculate the changes in ferroelectric material permittivity. In the eight cases of the capacitors mounted on the non-flexing boards, because the drop acceleration profile was measured on the same fixture surface to which the board was affixed, experimentally gathered accelerometer data was applied directly to the sub-model at the interface of the solder and the terminal as the input boundary condition only in the vertical,  $z$ -direction. Because the non-flexing board mechanical stress conditions were simpler and more accurately, and realistically represented the loads to which the capacitors were exposed compared to the flexing board scenarios, computational sub-model results of capacitance response of the devices mounted on the B configuration boards are first addressed in the following subsection.

#### ***4.3.1 Non-flexing Board Capacitor Response.***

From previous discussion, as long as the internal structure of the device remains intact during the impact, there are only three parameters affecting capacitance of the multi-layer ceramic capacitors - overlapping area  $A$ , and distance  $d$ , between the electrodes, and permittivity  $\epsilon$ , of the dielectric material. Because computational capacitor sub-model was developed in the Lagrangian frame of reference, the changes in  $A$  and  $d$ , which were represented by the amount the material tracers located at the opposing corners of the MLCC model shifted in the corresponding directions, accurately indicated the extent to which the material deformed during the impact. The amount of maximum material deformation, in

turn, signified any possible change in capacitance due to the linear variations in calculated overlapping electrode area and distance between plates.

Unfortunately, the amount of deformation predicted by the computational model could not represent the 10% change in capacitance during the shock that was observed in the laboratory. For example, during a non-flexing board configuration drop from a 72-inch height, generating an almost 22,000 g peak acceleration, tracers on the opposite sides of the capacitor shifted a total of  $7.02\text{ }\mu\text{m}$  closer to each other, introducing an increase in the overlapping electrode area  $A$ , by slightly over 0.0003%. Due to the linear relationship between the overlapping electrode area and capacitance  $C$ , the 0.0003% increase in overlapping area between electrodes would result in the same amount of increase in capacitance. Therefore, the more than four orders of magnitude difference between the computationally predicted and experimentally measured variations in capacitance, indicated that the mechanical shock-induced deformation of the dielectric could not explain the changes in capacitance observed in the laboratory. Also, the computationally calculated compression of the dielectric during the same 72-inch height drop, resulted in the tracers converging by only  $0.67\text{ }\mu\text{m}$ , reducing the distance between plates by less than 0.0001% and eliminating the possibility that the changes in capacitance were caused by the structural deformation of the ceramic after the shock. Furthermore, if the deformation of the dielectric could explain the significant increase in capacitance observed in the laboratory, the change in capacitance value would be evident even during the high voltage capacitor experiments and during every drop, especially for the same non-flexing board tests of low voltage devices from the 66-inch, 54-inch and 36-inch heights. However, because the capacitance response from drop to drop was intermittent, despite the similarity of the mechanical loads for each board configuration, suggests that structural deformations of the capacitors were not the cause of the capacitance increase during the impact, but were more than likely a result of the timing of the alignment of randomly polarized domains when capacitors

were charged at the time of shock, as discussed in Section 4.2 [11]. Finally, ceramic deformations calculated by the numerical sub-model were near the  $1e-5$  absolute error of the ALEGRA-EMMA solver, where it is possible that the predicted increase in the overlapping area and decreased distance between overlapping electrodes was mainly due to the numerical model limitations.

With the physical changes in dimension of the dielectric material eliminated as the cause for the capacitance increase observed in the laboratory during the impact, the only last possible explanation for capacitance increase was due to the piezoelectric effect of the mechanical stress produced by the drop impact on the permittivity of the dielectric ceramic [20, 27]. Therefore, in order to predict the electromechanical response of capacitance observed during the experiments, the focus of the computational sub-model of the capacitor exposed to mechanical loads was on calculating the shock-induced variations in permittivity in the z-direction.

The importance of using unique, raw and unprocessed accelerometer profiles for boundary conditions was previously discussed in Section 4.1 and Section 4.2. In the non-flexing board case, using specific single drop acceleration profiles was even more important than employing filtered or even half-sine wave profiles in order to accurately calculate the capacitance response based on the changes in permittivity. For example, as seen in Figure 4.28, by capturing only the initial impact shock profile, the electromechanical response due to the post impact acceleration vibrations completely disappeared and even the waveform of the capacitance response to mechanical load significantly diverged from the experimental results. Therefore, in order to seize the uniqueness of each individual drop acceleration profile and, in turn, capacitance variations based on the said boundary conditions, all the computational runs of the MLCC sub-model in Table 4.2 were conducted with the unprocessed accelerometer data as an initial input for the non-flexing, as well as flexing board configurations.



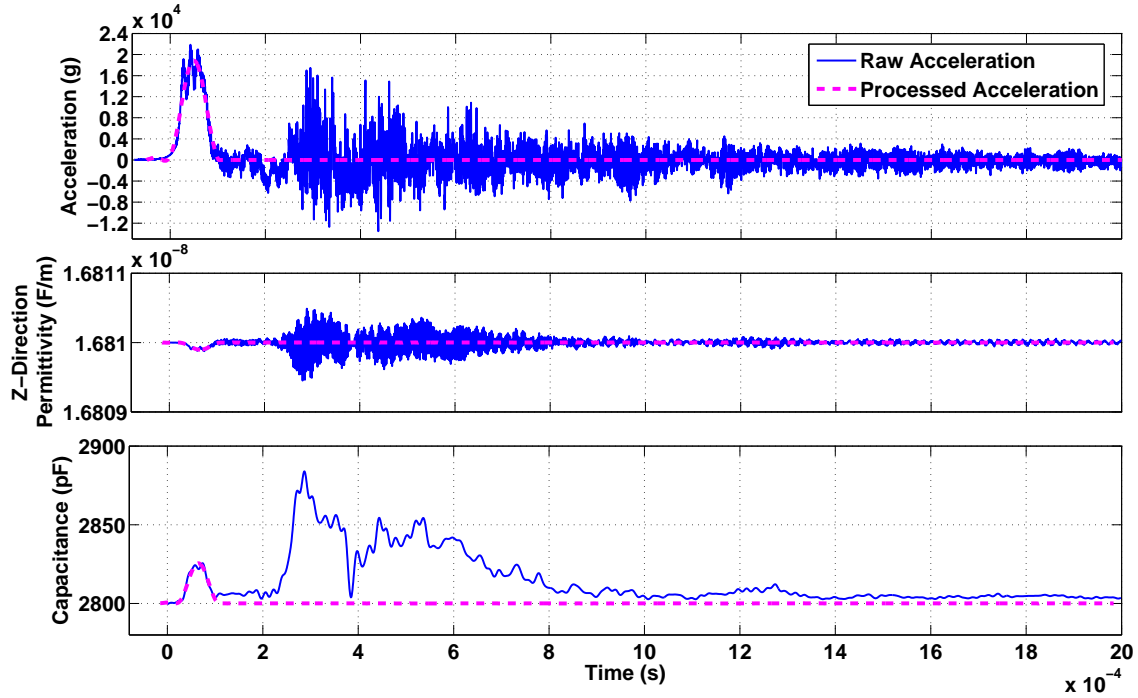


Figure 4.28: Effect of Processed Acceleration Profile as Boundary Condition on Computationally Obtained Permittivity and Capacitance Values for a 72-inch, Non-flexing Board Drop

While using raw and unfiltered accelerometer data for boundary conditions in the MLCC sub-model captured the post impact acceleration and vibration effects more precisely than the filtered boundary conditions, the calculated permittivity response to the mechanical shock still produced values approximately three orders in magnitude lower than necessary to obtain the 5.9% capacitance variations for a single 72-inch drop test observed in the laboratory, as seen in Figure 4.29. Furthermore, as seen in Figure 4.29, calculated z-direction permittivity exhibited both increases and decreases from its nominal value of 16.81 nF/m after the initial impact, correlating much closer in shape to the acceleration profile, rather than the experimentally obtained capacitance increase. The fact that the capacitance calculations based on the computational sub-model results for permittivity

changes applied directly to Equation (2.7) exhibited a piezoelectric response, but were three orders of magnitude lower than the capacitance increase observed during the experiments, necessitated the development of a new constitutive relationship that accurately described the electromechanical response based on the acceleration boundary conditions applied to the newly developed capacitor sub-model.

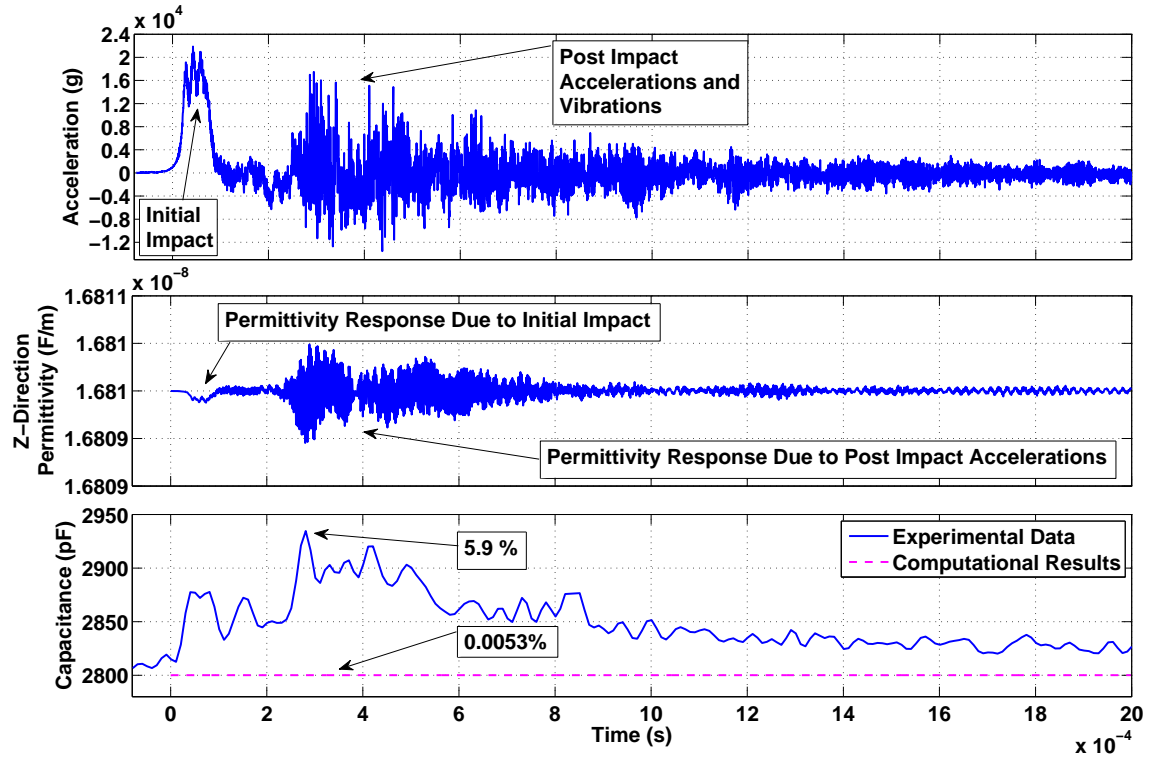


Figure 4.29: Capacitance Response Based on Direct Calculation of the Permittivity Results in 3 Order of Magnitude Difference Between Experimental Data and Computational Predictions

As discussed in Section 2.3, according to the Landau-Ginsberg model for the behavior of ferroelectric material, free energy was calculated using the magnitude of the gradient of the polarization vector. The LG theories, suggesting that the electromechanical response is likely tied to the magnitude of the polarization, imply that permittivity response,

and thus capacitance variations under mechanical stress, can be calculated by applying the magnitude of the computationally obtained permittivity change. However, because permittivity  $\epsilon$ , of the dielectric in Equation (2.7) is related to the permittivity of free space  $\epsilon_0$ , and the relative dielectric constant  $K$ , the magnitude of the piezoelectrically induced permittivity variations computed by the sub-model was first added to the permittivity of vacuum and then multiplied by the dielectric constant to obtain the final value. The procedure for calculating the capacitance response to mechanical stress employed the concept of the capacitor volumetric efficiency to predict the electromechanical response of components shocked with the drop tower.

First, the volumetric efficiency,  $E_{vol}$ , of the capacitors with nominal capacitance of 2,200 pF was calculated by dividing the capacitance by the starting permittivity in the z-direction,  $\epsilon_z$ . Then, the magnitude of averaged tracer permittivity changes,  $|\Delta\epsilon_{avg}|$ , was multiplied by the dielectric constant,  $K$ , and added to the initial value,  $\epsilon_z$ . Capacitance was finally calculated by multiplying the previously calculated volumetric efficiency by the newly calculated permittivity, as shown in Equation (4.1) below.

$$C = \left( \epsilon_z + K|\Delta\epsilon_{avg}| \right) E_{vol} = \left( \epsilon_0 + |\Delta\epsilon_{avg}| \right) K \frac{A}{d} \quad (4.1)$$

Using the newly developed constitutive relationship in Equation (4.1) and the unprocessed acceleration profiles as the boundary conditions for applying mechanical stress, computational capacitance responses for all the non-flexing board configuration drops were calculated and the results presented in Figure 4.30. Comparing the capacitance changes under shock between the experimentally measured and computationally obtained values, the waveforms of the electromechanical response matched very closely. For example, not only did the model predict greater increases in capacitance during post impact vibrations for higher drops, such as the 72-inch heights, but the relative magnitude of the capacitance response, both drop to drop, as well as between initial and post impact acceleration effects for any single impact, was proportional to jerk, as shown in Figure 4.31.

Such close waveform proportionality reinforced the theory that the capacitance changes were due to piezoelectric effects of ferroelectric dielectric during the impact, and that the increase in capacitance was due to the electromechanical response of the ceramic, as opposed to the mechanical or structural breakdown of the material.

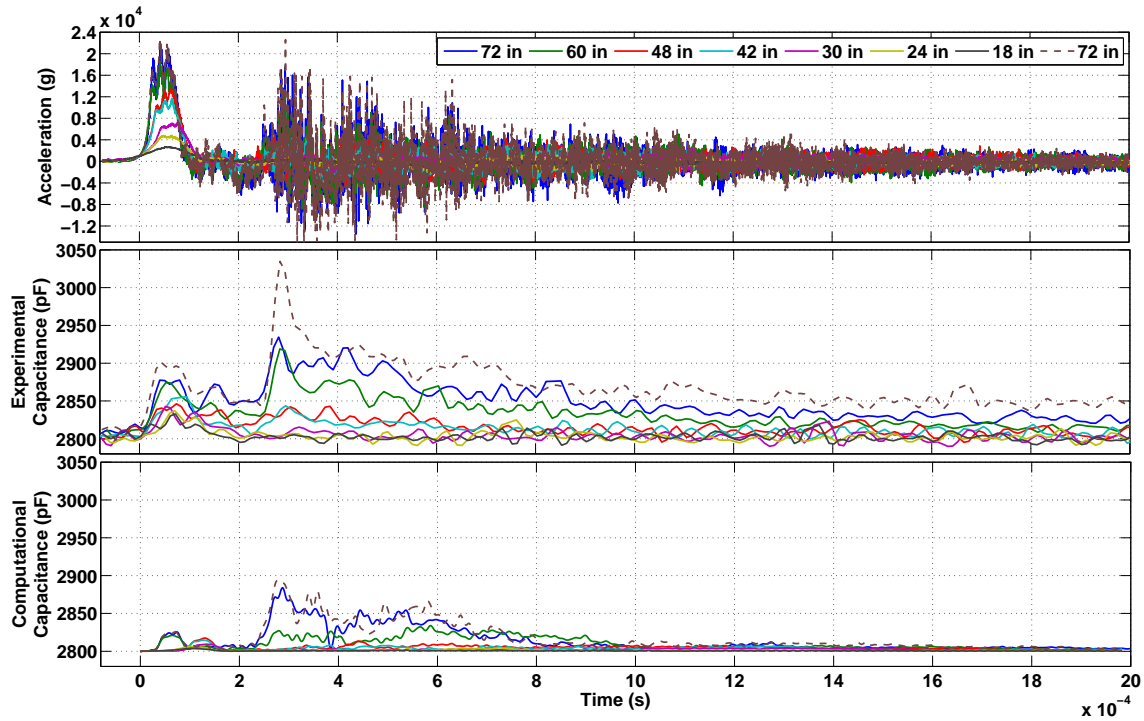


Figure 4.30: Experimental vs. Computational Capacitance Response for All 8 Non-flexing Board Drops

While experimentally measured and computationally obtained capacitance changes were within the same order of magnitude, despite varying by as much as 400%, the difference between computationally calculated and experimentally measured values was within 2% of the nominal capacitance of the MLCC. The discrepancy between sub-model predictions and laboratory data could be reduced by refining the mesh and also by lowering the elasticity modulus constants. Unfortunately, refining the mesh from  $50\text{ }\mu\text{m}$  to  $20\text{ }\mu\text{m}$

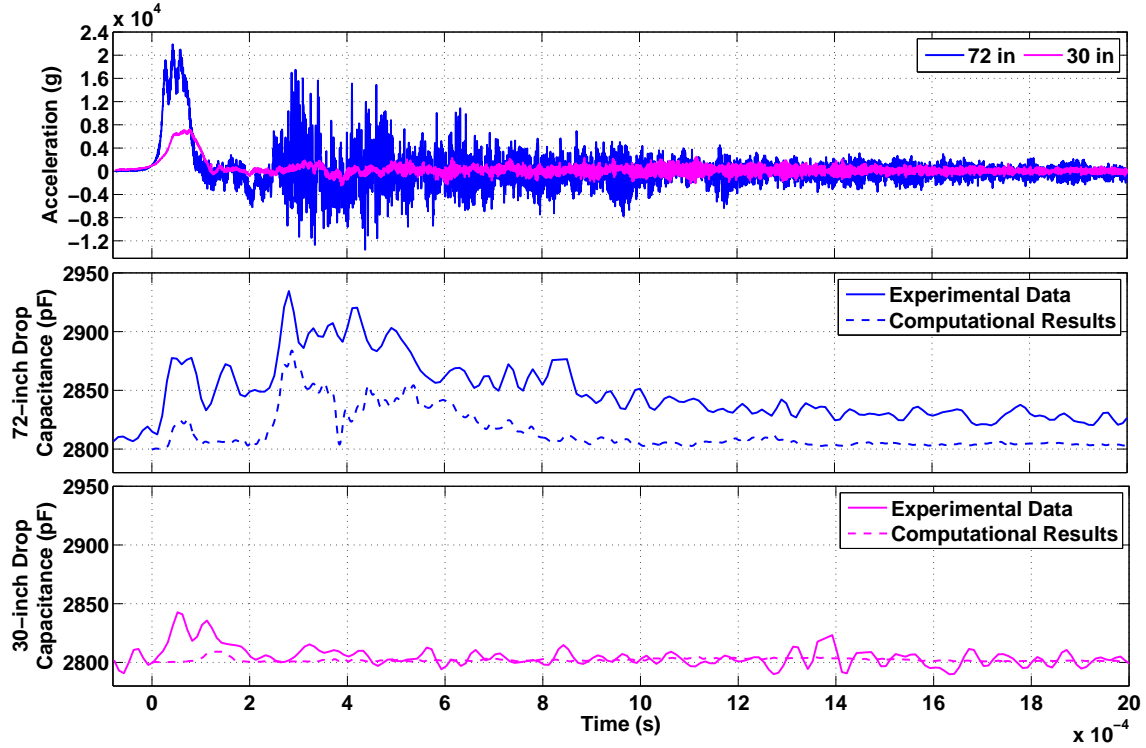


Figure 4.31: Experimental vs. Computational Capacitance Waveform Comparison

element size, would decrease the time step necessary for the stability of the finite element computation to such a small value (1.74 nanoseconds), that it would allow only two drops to be simulated, based on the total 670,000-hour allocation for this research on the HPC. Despite the small time step and the large number of hours required to conduct fine mesh runs, purely for convergence study purposes, a single run in the non-flexing board configuration was carried out. Also, as discussed at the end of Section 3.5, the values for the elastic modulus constants were selected from literature for Barium Titanate ceramic, which was not necessarily the exact same material used in the capacitors under test. In fact, the capacitor manufacturer specified a single direction Young's modulus for the X7R Barium Titanate-based ceramic used for the MLCC to be as low as 105 GPa, compared to the 166 GPa used in the computations. In order to test the sensitivity of the sub-model

capacitance calculations to the variations in Young's modulus and mesh element size,  $C_{11}$  and  $C_{33}$  constants were reduced by 30 GPa, from 166 GPa and 162 GPa, to 136 GPa and 132 GPa respectively, with simulations conducted with 50  $\mu\text{m}$ , and 20  $\mu\text{m}$  elements for slightly over a millisecond duration. As expected, and shown in Figure 4.32, with both the decrease in elastic modulus and the refinement of the mesh, the capacitance response predicted by the sub-model converged to the experimentally measured values, validating the electromechanical response model and the newly developed constitutive relationship between the capacitance, and the mechanical stress-induced changes in permittivity for ferroelectric ceramic capacitors mounted on the non-flexing boards.

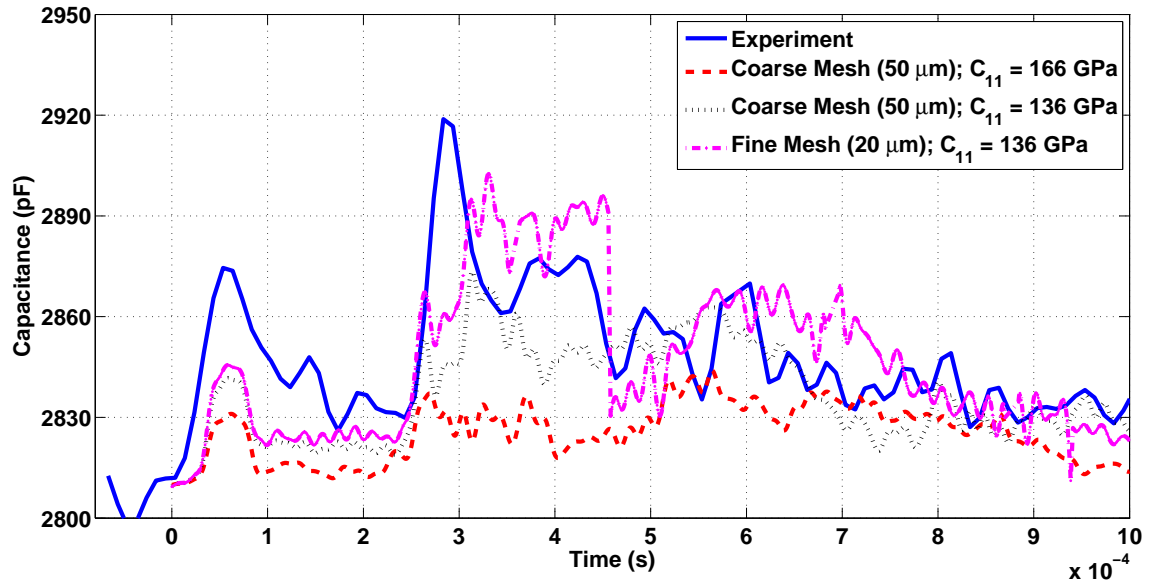


Figure 4.32: Effect of Reducing Elastic Modulus Constants and Refining the Mesh; 60–inch, 18,487 g Impact

Closer agreement between computational and experimental data than shown in Figure 4.32, was not reasonable, due to the fact that the acceleration profiles applied as boundary conditions to the capacitor sub-model, despite being unprocessed, were not

measured at the same exact surface on which capacitors were mounted, with the PCB material in between. Also, piezoelectric and permittivity moduli constants were selected from literature, and, as mentioned earlier, did not necessarily represent the material properties of the ferroelectric dielectric used inside capacitors under test. Despite these inconsistencies between the sub-model and the experiments, for the first time in literature, the electromechanical response of ferroelectric ceramic capacitors subjected to high-g drop impacts was relatively accurately predicted based on the newly developed constitutive relationship between capacitance and the change in permittivity induced by the mechanical stress. However, with slight modifications, the developed constitutive relationship was also applicable to the non-flexing board configurations, despite the additional degrees of freedom generated by the flexure of the ferroelectric, as discussed in the next subsection.

#### ***4.3.2 Flexing Board Capacitor Response.***

When calculating the capacitance response of the devices dropped in the flexing board configuration, the same capacitor sub-model was used, as during the non-flexing board investigations. The only difference between the computations, were the acceleration profiles that were applied as boundary conditions. During the non-flexing board experiments, the board did not flex and no significant amount of strain in the x or y direction was imposed on the top surface of the PCB, where the components were mounted. Thus, only vertical drop shock acceleration profile was applied to the non-flexing board cases. However, in the flexing board scenarios, with the top surface strained at up to 6,000  $\mu$ strains in the x-direction, board dynamics produced additional degrees of freedom, which contributed significant accelerations in the x and y directions. Therefore, as mentioned earlier, board dynamics model developed in Section 4.1 was first used to determine the acceleration profiles at the locations where the capacitors were mounted, and then applied to the capacitor sub-model to calculate the changes in permittivity, from which capacitance was calculated.

While the additional degrees of freedom in the flexing board cases created different dynamics, the stiff ceramic dielectric material still did not produce structural deformations to explain the more than 10% increases in capacitance. Just as in the non-flexing board scenarios, flexing board deformation could only account for changes in the overlapping electrode area and thickness that resulted in computational capacitance response four orders of magnitude lower than observed in the laboratory. Therefore, the assumption that changes in capacitance were due to the electromechanical response of ferroelectric ceramic under stress, was still valid for the flexing board case.

Also, just as in the case of the non-flexing board, the flexing board capacitor electromechanical response matched closely in waveform to the applied triaxial acceleration profiles, which in turn translated into primarily x-direction strain after the dominant z-direction acceleration. As can be seen in Figure 4.33, at least until components begin to mechanically fail and separate from the board, capacitance changes, both measured during the experiment in the laboratory and predicted by the computational model are cyclical in nature, corresponding in frequency to the x-direction strain of the top PCB surface.

However, in order to accurately predict the magnitude of the capacitance response in the flexing board scenario, due to the additional degrees of freedom and stronger electromechanical response, the constitutive relationship for calculating capacitance changes based on mechanical stress-induced permittivity variations in Equation (4.1), had to be modified. The magnitude of the model-calculated change in permittivity  $|\Delta\epsilon_{avg}|$ , was divided by ten in order to obtain the updated constitutive relationship between the computationally calculated changes in permittivity and the capacitance response to the mechanical drop shock for the flexing board cases, as can be seen in Equation (4.2).

$$C = \left( \epsilon_z + 1/10K|\Delta\epsilon_{avg}| \right) E_{vol} = \left( \epsilon_0 + 1/10|\Delta\epsilon_{avg}| \right) K \frac{A}{d} \quad (4.2)$$

The exact interaction between the polarized domains under mechanical stress conditions indicative of capacitors mounted to the flexing board, which caused the sub-



model to overestimate the electromechanical response was unknown. However, the fact that in the flexing board cases, where more complex boundary conditions were applied to the material and capacitance changes of 10% were observed in the laboratory even from a 36-inch drop, while only a 6% capacitance increase was detected in the non-flexing board scenario under a 72-inch impact, confirmed the sensitive nature of the ferroelectric material to the precise loading conditions.

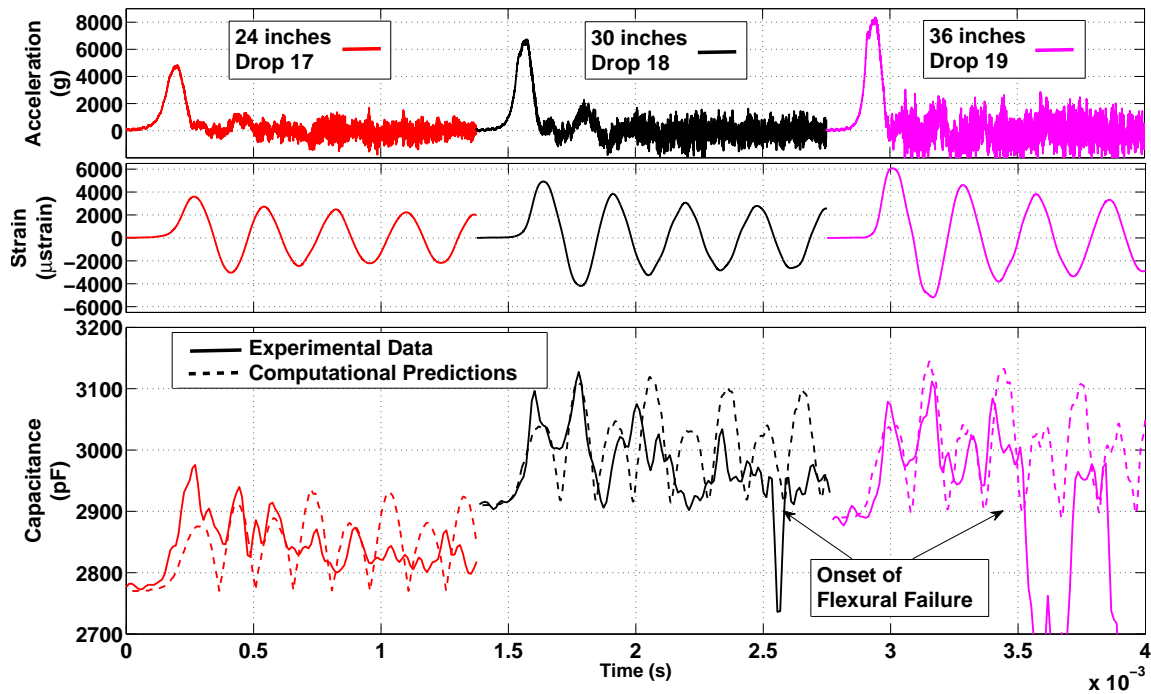


Figure 4.33: Experimental vs. Computational Capacitance Response for All 3 Flexing Board Drops

One of the possible explanations for flexing board capacitance response discrepancy between the experimental data and the computational predictions, rests with the accuracy of the boundary conditions applied to the ferroelectric ceramic model. From the non-flexing board cases, it has already been established that piezoelectric response of ferroelectric ceramic is directly tied to the acceleration profile and, in particular, to the jerk. However,

in order to accurately transmit complex shock profiles collected at the surface of the fixture and propagate their effects to the board dynamics, from which exact surface accelerations can be determined and applied precisely as boundary conditions to the sub-model, a more accurate board dynamics model than the one developed in Section 4.1 must be created. The fact that the board dynamics model underestimates strain in nearly every case, indicates that it overestimates the modulus of elasticity, making the board appear stiffer. The net effect of the stiffer board, is the increased magnitude of the acceleration profiles calculated at the location of mounted capacitors, resulting in the higher electromechanical response predictions. While the extent to which computationally stiffer board increases the predicted capacitance response is unknown, reducing the modulus of elasticity of the board to the point where its computationally obtained strain response matches experimentally measured strain, could easily reduce the acceleration magnitude of boundary conditions at the capacitor locations to the levels that generate more comparable capacitance variations to the experimental data. The combination of the accurately predicted electromechanical response of the flexing board in frequency, corresponding to the board surface strain oscillations, and the relatively accurate capacitance magnitude increase compared to the experimental data, validated the capacitor sub-model and its predictions of change in permittivity due to piezoelectric effects.

As mentioned at the beginning of this chapter, the three distinct phases of the current research produced several results and contributions related to the survivability of electronics exposed to high-g impact stresses. First, a computational dynamics model was developed using isotropic, linear elastic material model to predict board strain oscillations post impact. Based on the parametric computational study of the effects of varying parameters, such as density and Young's modulus, on the frequency and magnitude of board strain oscillations generated by the 15,754 g peak acceleration impacts, computational surface strain predictions of the ISOLA 370HR boards were accurately predicted, and

compared to the experimental data. Board strain oscillation frequency was predicted to within 2.3% of the measured data and using the unfiltered acceleration profiles, magnitude of the peak strain oscillations was simulated to within 45% of the strain gage measurements at the top center of the PCB. While similar analysis has been previously performed and available in open literature for the FR4 circuit board material at drop impacts with peak accelerations on the order of 3,000 - 4,000 g, it is only for the first time that the input-g method has been applied to computationally predict board dynamics under shock impacts an order of magnitude greater than those specified in the JEDEC standards. However, the main outcome of the development of the dynamic board response computational model was the calculation of the triaxial flexing board acceleration profiles at the pads where the capacitors were soldered, in order to provide accurate boundary conditions for the capacitance response sub-model.

Next, using the RC measurement technique, transient capacitance response during the shock of ferroelectric MLCC was measured for the first time. Near real-time monitoring of the capacitance identified the flexural mode of mechanical failure for surface-mounted capacitors exhibiting the same three stages of failure previously described in Chapter 2. However, with the addition of the impedance analyzer and SEM analysis of the mechanically failed components, both complete and partial multi-layer ceramic capacitor failure was tied to the strain and strain rate, with capacitance varying based on the fraction of electrodes still in contact with the terminal during post impact board oscillations. While the boards were allowed to flex, initial mechanical component separation mechanism of the surface-mounted devices was always based on the flexural mode of failure, which began at strains as low as 5,000  $\mu$ strains, depending on the size of the failed components. Even though the physical dimensions of the capacitors seemed to marginally affect the maximum peak acceleration, which components could withstand, the greatest impact on the mechanical mode of failure was the amount the board was allowed to flex after the drop

shock. In fact, while all the components in the flexing board configuration began to fail at 11,670 g, non-flexing board configurations did not produce any mechanical separations of capacitors with drop shocks up to 22,594 g tested in the laboratory. While mechanical failure seemed to be avoidable, the electromechanical response, which generated significant piezoelectrically-induced capacitance increases of up to 10%, unfortunately, could not be averted with simple board oscillation reduction techniques.

Thus, finally, a computational sub-model of the MLCC was developed, and the piezoelectric effects on permittivity calculated in the computations were able to predict the capacitance increase observed in the laboratory for both the flexing and non-flexing board scenarios. For the first time, the variations in permittivity calculated by the computational sub-model could be used to predict the capacitance changes of devices undergoing mechanical drop shock to within the same order of magnitude by developing a simple constitutive relationship shown in Equation (4.1), which is particularly critical in high voltage capacitor applications. As long as the capacitors were electrically charged during the impact, aligning the randomly polarized domains, up to a 10% increase in capacitance was observed for the devices mounted on the flexing boards exposed to approximately 15,000 g peak accelerations, while up to a 6% increase in capacitance was measured during the non-flexing board drops despite the near 24,000 g peak accelerations encountered in the laboratory. The 6-10% increase in capacitance is significant enough when designing a circuit to require a quantification of the effect that can be correlated to specific mechanical stress conditions in which the components will operate. The experimentally measured changes in capacitance due to the piezoelectric effect for both flexing and non-flexing boards, as well as the partial and complete discrete changes in capacitance coinciding in frequency with board oscillations due to the flexural mode of failure, which were described in the current chapter and summarized in the previous two paragraphs, are illustrated in Figure 4.34.

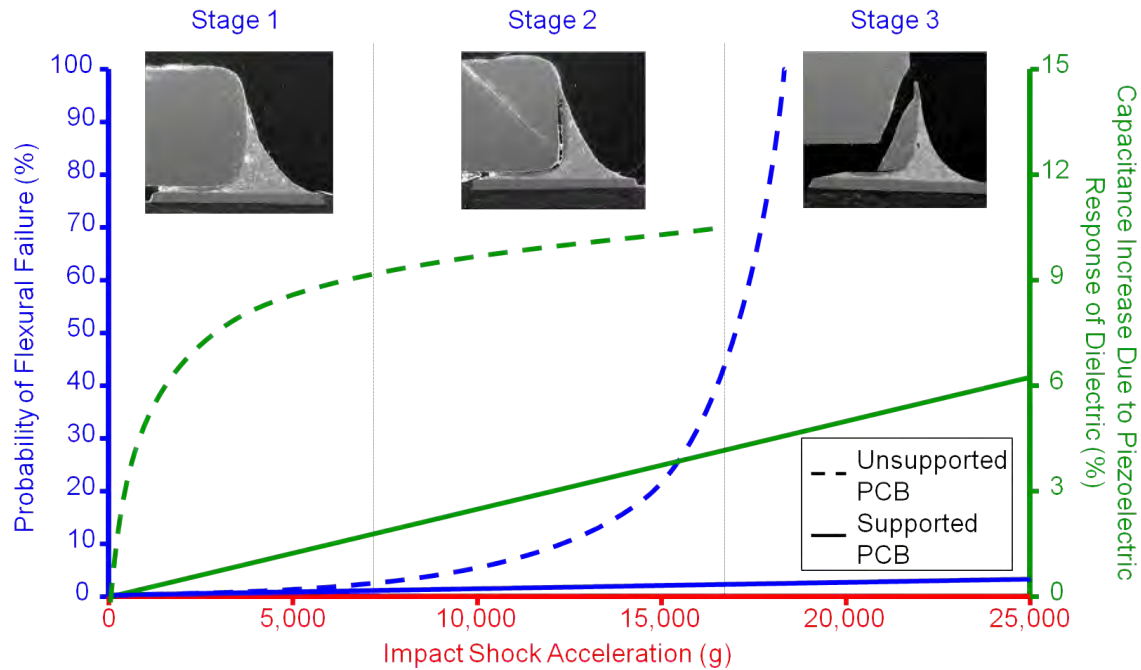


Figure 4.34: Approximation of Mechanical Failure Probability and Electromechanical Response of Flexing and Non-flexing Boards

While additional degrees of freedom for the flexing board capacitors resulted in greater capacitance response, as illustrated in Figure 4.30 and Figure 4.33, the fact that the capacitance increase of ferroelectric ceramic dielectrics exposed to mechanical stress was due to the piezoelectric response was evidenced by the fact that the capacitance waveform closely related to the stress-induced changes in permittivity predicted by the computational model and validated by the experimental measurements. However, although it might be possible to reduce the possibility of a mechanical failure, lower the electromechanical response and stabilize the performance of the devices by preventing board flexure during high-g impact, as seen in Figure 4.34, significant increases in capacitance must still be addressed when attempting to predict component reliability and electronics survivability of ferroelectric dielectric capacitors exposed to peak accelerations above JEDEC specified standards. Therefore, the newly established constitutive relationship based on the

developed computational model for calculating permittivity variations and capacitance increases of devices in response to a high-g mechanical drop impact is a significant contribution to the science of electronics survivability.

## V. Conclusions

The aerospace industry is constantly striving to develop technology that is capable of operating in different environments, thereby exposing electronics to progressively harsher mechanical stress conditions. Additionally, the desired weight savings, which are a byproduct of miniature electronics, continually drive requirements for smaller electrical components. In turn, in order to accommodate the industry request for physically smaller devices, while maintaining functionality of the electrical components, use of exotic dielectric materials inside electronic packages has quickly proliferated. Particularly, smaller capacitors requiring higher voltage and greater capacitance ratings have started to employ high dielectric constant materials, such as ceramics based on Barium Titanate. However, the same ferroelectric properties of exotic ceramics that desirably increase the material's dielectric constant, also make the material piezoelectric in nature. Unfortunately, the reliability of ferroelectric multi-layered ceramic capacitors has been seldom investigated under the harsh mechanical stress conditions, to which ferroelectric components are increasingly exposed.

The system level testing of components utilizing such materials, and even the standards to test the capacitors exposed to the newly explored conditions, make the development of survivable electronics technology cost prohibitive and time consuming. Not only are the devices untested at the system level due to the lack of standards for high mechanical load conditions above 3,000 g, but even raw material properties, such as orthotropic elastic modulus, piezoelectric constants and permittivity moduli require elaborate experimental equipment and measurement procedures. The requirement for specialized laboratory equipment and specific dimensions of the material sample is perhaps why the manufacturers that already use ferroelectric ceramics in their capacitors have only recently began investigating properties of the bulk ferroelectric materials, making

the determination of the exact electromechanical properties of the ferroelectric dielectric ceramics based on Barium Titanate very sparse. The piezoelectric resonators and raw dielectric materials were not available for this research in the dimensions necessary to measure the electromechanical properties of the ceramic used in the MLCC. Therefore, the focus of this study was on developing an experimentally validated computational sub-model of a multi-layered capacitor and a constitutive relationship between the model-predicted permittivity and the change in capacitance of the device under mechanical stresses an order of magnitude greater than even those specified in the current JEDEC standards for board level component survivability testing.

In order to develop and validate the finite element analysis sub-model and the constitutive relationship between the mechanical stress-induced permittivity variations and the increases in capacitance, the sub-model was employed under flexing board configurations, which represent most of the commercial packaging configurations, as well as in the non-flexing board scenarios, which are indicative of high-g impact survivable technology and military applications. In the non-flexing board cases, accelerometer data measured during the impact was applied directly to the capacitor sub-model for mechanical stress boundary conditions. However, for the flexing board configuration, triaxial acceleration profiles at the locations where the components were soldered, were first calculated by the newly developed numerical board dynamics model and later applied as boundary conditions to the capacitor sub-model.

The first computational model developed using ALEGRA-EMMA predicted board dynamics and calculated the triaxial acceleration boundary conditions imposed on the surface mounted capacitors in the flexing board configuration. The board dynamics model was also validated with experimental surface strain measurements and also, by conducting a computational parametric sensitivity study. Board strain oscillation frequency was predicted by the numerical model to within 2.3% of the experimental measurements and the



peak strain amplitude was precisely calculated using the half-sine wave acceleration profile. Despite the fact that an accurate acceleration waveform is required to predict MLCC electromechanical response, for the first time in the open literature, the current research confirmed the relatively unknown ISOLA 370HR material properties and employed the computational board dynamics model to drop impacts an order of magnitude greater than those specified in the JEDEC standards, and explored by the commercial industry. The newly developed computational PCB dynamics model, which accurately predicted board strain response in both frequency and amplitude, proved that a simple linear elastic material model inside the ALEGRA-EMMA finite element code can be used to output acceleration profiles to which components are exposed anywhere on the surface, even during the high-g drop impacts, greater than 3,000 g. Such a simple computational board dynamics model can be easily employed to accurately quantify mechanical stresses to which surface mounted components are exposed, and subsequently applied as boundary conditions to the device sub-models, when predicting capacitor electromechanical response.

In order to experimentally validate electromechanical response of numerical capacitor sub-models, both mechanical mode of failure and electromechanical capacitance response of capacitors were detected using the RC measurement technique. While the capacitance measurement method used during this study was not new, for the first time, the technique was applied to measuring transient capacitance changes of components exposed to high-g impacts on the order of 15,000 - 24,000 g. Despite the fact that even after multiple impacts as high as 24,000 g no components partially or completely failed in the non-flexing board configurations, when flexing board capacitors began to separate at drop shocks as low as approximately 12,000 g, confirmed that the overwhelmingly flexural mode of mechanical failure was related to the strain and the strain rates to which the solder interconnects were exposed. The RC technique, impedance analyzer and SEM imagery analysis were all adequate to detect the partial discrete variations in capacitance related to the fraction of the

number of separated electrodes from the terminal. However, the RC method was also able to correlate the discrete changes in capacitance to the board flexure oscillation frequency and detect the three stages of mechanical component failure, previously described in the literature for resistors and circuit boards exposed to less than 4,000 g impacts. Thus, the RC dynamic measurement technique proved to be a suitable and accurate capacitance measurement method for monitoring discrete capacitance changes of surface mounted components, as well as detecting the precise time of intermittent and complete flexural modes of mechanical failure, especially during high-g impacts.

While mechanical mode of failure was clearly observable, the main focus of this research was on predicting the electromechanical response of capacitors that use ferroelectric ceramics for the dielectric. The energy dispersive spectroscopy confirmed the Barium Titanate material as the basis for the dielectric inside the capacitors under test, making it reasonable to attempt to predict the piezoelectric response of capacitors and to observe changes in capacitance of devices under mechanical shock. Both flexing and non-flexing board capacitors exhibited the electromechanical response in the laboratory, which validated the developed sub-model predictions and constitutive relationship calculations of capacitance variations based on the precise mechanical stress waveform. In both cases, computationally obtained changes in capacitance correlated closely to the time derivative of the acceleration profiles, to which the capacitors were exposed during the drop. Capacitance was easily calculated using the new constitutive relationship by adding the magnitude of the permittivity variation that was predicted by the sub-model to the permittivity of free space, and then multiplying the sum by the original dielectric constant and the volumetric efficiency factor. While the waveform of the capacitance increase was accurately predicted, and clearly related to the shape of the acceleration profile, magnitude of the computational capacitance predictions was less accurate, but still within 2% of the nominal capacitance of the devices under shock. Therefore, in order to calculate the

electromechanical response and quantify the changes in capacitance of surface mounted devices, a combination of the newly developed capacitor sub-model and the modified constitutive relationship for the capacitance of the MLCC, with the addition of the numerically obtained changes in permittivity, can now be employed to make reliability predictions of electronic packages exposed to harsh mechanical stresses.

Reducing the degrees of freedom of the applied mechanical stress by restricting the board flexure, as was the case in the non-flexing board configurations, also reduced the electromechanical response by up to 81% during impact on the order of 7,000 g. Such stark reduction in capacitance response predicted by the sub-model and observed in the laboratory captures the complex interactions between the randomly polarized and directionally aligned domains of the ferroelectric materials in the presence of an electric field during the impact. In fact, it was only when the capacitors were charged at the exact moment of impact, coinciding with the alignment of the polarized domains, that the ferroelectric ceramic devices exhibited any piezoelectric response. While it may seem attractive to prevent the board flexure after impact in order to reduce the possibility of flexural failure and to lower the electromechanical response of the ferroelectric dielectric MLCC, even with the non-flexing configurations, where the board was fixed directly to the steel fixture, up to a 6% increase in capacitance was evident during the impact with peak acceleration on the order of 24,000 g. Thus, even if the board is prevented from flexing post impact, the greater the shock to which the capacitors are exposed, the greater the change in capacitance that must be contended with for electronic packages exposed to harsh mechanical stress environments. Such capacitance changes induced by the mechanical stresses will have to be addressed by the circuit board designers before the COTS electronics packages and components can be used in high-g impact applications with any degree of reliability.

Based on the validated board dynamics model, newly applied capacitance measurement technique, novel capacitor sub-model and modified capacitance constitutive relationship, which were a direct outcome of the current research, several conclusions can be drawn. First, it has been proven that printed circuit board dynamics can now be computationally modeled with good accuracy using relatively simple linear elastic material models in ALEGRA-EMMA finite element code. Second, the triaxial acceleration profiles harvested during such simulations may be employed as mechanical stress boundary conditions and applied to the component sub-models of capacitors located anywhere on the board surface during high-g impact greater than 3,000 g. Next, the RC measurement technique, which can detect device capacitance variations during a high-g impact, was accurate enough even at relatively high data rates and may be employed to obtain capacitance readings in highly dynamic environments. Also, the newly developed multi-layer ceramic capacitor computational sub-model in ALEGRA-EMMA, which calculates permittivity changes based on the piezoelectric response of the ferroelectric dielectric can be applied to modify the constitutive relationship to accurately predict capacitance variations of the devices exposed to high-g impact. Finally, from the experimental and computational efforts during this research, it is clear that the electromechanical response of COTS capacitors with ferroelectric dielectrics, and not just mechanical failure of the component interconnects, must be addressed when exposing such devices to high-g environments, regardless of the flexing or non-flexing board configurations. The development of the computational MLCC sub-model and the modified constitutive relationship between the piezoelectrically induced permittivity changes and capacitance variations, as computationally calculated and experimentally validated in the laboratory with the dynamic RC method during the current research, is the first step in developing more reliable and survivable electronics packages for high-g mechanical stress environments.

However, the current study is not without its limitations, and a more refined sub-model that can predict piezoelectric response of ferroelectric ceramics should be developed, among other recommendations for future work. The first area for improvement is in determining the exact elastic, piezoelectric and permittivity constants for the precise material used during the drop tests. Since the unique material specimens and laboratory equipment were not available to measure the material moduli, published Barium Titanate ceramic properties were used for this study, despite certain elastic moduli constants varying by as much as 20% from the manufacturer specified values. Second, especially for the flexing board cases, a more accurate, orthotropic board model needs to be used, in order to more precisely calculate the dynamic board response, which has a direct effect on the boundary conditions and the mechanical stresses applied to the computational capacitor sub-model. Neither the orthotropic material finite element model, nor the orthotropic material properties were available for such analysis, necessitating the use of the less representative linear isotropic model, resulting in numerical capacitance response predictions an order of magnitude higher than observed in the laboratory. Next, from the experimental perspective, at least a three to four times higher data rate oscilloscope would be preferred to measure the voltage across the capacitor. By increasing the data rate, charge/discharge pulse frequency could be increased, reducing the error of the least squares fit in half when measuring capacitance, or proportionally increasing the total time the capacitor under shock can be monitored. Finally, with the availability of a more robust finite element code, a comprehensive computational model could be used in order to capture the mechanical failure mechanisms, as well as the piezoelectric response of the ferroelectric ceramic capacitors, in order to predict potential fracture initiation and propagation, while at the same time calculating capacitance variations of such devices. Such computational model would necessitate an extensive grid convergence study in order to select proper mesh elements for various electronic package components

to predict both material and electromechanical failures. The grid convergence study would require capacitance measurements experimentally gathered at very high data in order to determine not only the magnitude of capacitance variation, but also the exact time when the interactions between flexural mode of failure and capacitance changes would become significant enough to impact electromechanical response. Therefore, in order to create such a comprehensive computational model, the elements would need to be so small, that the model would be virtually mesh independent and converge asymptotically to a particular capacitance value, exponentially increasing the requirement for computational power.

Despite the above mentioned recommendations, in addition to the requirement for the more accurate layout of the physical MLCC model, which would further increase the need for greater high performance computing power, the first investigation into the electromechanical response of capacitors was fairly successful. As a result of this research, the newly developed capacitor sub-model and constitutive relationship can now be used to predict the piezoelectric response of ferroelectric ceramics under mechanical stress with reasonable accuracy. However, for both commercially relevant board dynamics, as well as for PCBs designed for high-g impact survivability, it is clear that even if the mechanical failure can be averted through the use of potting and structural supports, during drop shocks on the order of 3,000 g and higher, electronics packaging designers will have to address the capacitance variations, if ferroelectric ceramics are employed in the circuit. By accounting for the piezoelectric response of ferroelectric ceramics under high-g mechanical stress, the aerospace industry can move toward the more reliable and survivable electronics, which find exploitation in increasingly harsher operational environments.

## Bibliography

- [1] JEDEC Standard JESD22. B111. *Board level drop test method of components for handheld electronic products*, 2003.
- [2] JEDEC Standard. JESD22–B110. *Subassembly mechanical shock*, 2001.
- [3] IPC/JEDEC Standard. IPC/JEDEC–9703. *Mechanical Shock Test Guidelines for Solder Joint Reliability*, March 2009.
- [4] Jennifer L. Jordan, Clive R. Siviour, Jason R. Foley, and Eric N. Brown. Compressive properties of extruded polytetrafluoroethylene. *Polymer*, 48(14):4184–4195, 2007.
- [5] Jennifer L. Jordan, Jason R. Foley, and Clive R. Siviour. Mechanical properties of epon 826/dea epoxy. *Mechanics of Time-Dependent Materials*, 12(3):249–272, 2008.
- [6] Ryan D. Lowe, Jacob C. Dodson, Jason R. Foley, Christopher S. Mougeotte, David W. Geissler, and Jennifer A. Cordes. Constitutive response of electronics materials. In *Challenges In Mechanics of Time-Dependent Materials and Processes in Conventional and Multifunctional Materials, Volume 2*, pages 57–74. Springer, 2014.
- [7] P.A. Taylor. CTH reference manual: The Steinberg-Guinan-Lund viscoplastic model. *Sandia National Laboratories Report SAND92-0716*, 1992.
- [8] Bradley W. White, Harry Keo Springer, Jennifer L. Jordan, Jonathan E. Spowart, and Naresh N. Thadhani. Mesoscale simulations of particle reinforced epoxy-based composites. Technical report, DTIC Document, 2012.
- [9] M. Elices, G.V. Guinea, J. Gomez, and J. Planas. The cohesive zone model: advantages, limitations and challenges. *Engineering fracture mechanics*, 69(2):137–163, 2002.
- [10] Nicolas Moës and Ted Belytschko. Extended finite element method for cohesive crack growth. *Engineering fracture mechanics*, 69(7):813–833, 2002.
- [11] Bernard Jaffe, William R. Cook Jr., and Hans Jaffe. *Piezoelectric ceramics*, volume 3. Academic Press Inc., 1971.
- [12] Larry L. Altgilbers, Jason Baird, Bruce L. Freeman, Christopher S. Lynch, and Sergey I. Shkuratov. *Explosive Pulsed Power*. World Scientific, 2011.
- [13] R.E. Setchell, B.A. Tuttle, and J.A. Voigt. Microstructural effects on the shock response of PZT 95/5. In *Shock Compression of Condensed Matter-2003: Proceedings of the Conference of the American Physical Society Topical Group on Shock Compression of Condensed Matter*, pages 180–186. American Institute of Physics, 2004.

- [14] Robert E. Setchell. Shock wave compression of the ferroelectric ceramic  $\text{Pb}_{0.99}(\text{Zr}_{0.95}\text{Ti}_{0.05})_{0.98}\text{Nb}_{0.02}\text{O}_3$ : Hugoniot states and constitutive mechanical properties. *Journal of applied physics*, 94(1):573–588, 2003.
- [15] Robert E. Setchell. Shock wave compression of the ferroelectric ceramic  $\text{Pb}_{0.99}(\text{Zr}_{0.95}\text{Ti}_{0.05})_{0.98}\text{Nb}_{0.02}\text{O}_3$ : depoling currents. *Journal of applied physics*, 97(1):013507, 2004.
- [16] Robert E. Setchell. Shock wave compression of the ferroelectric ceramic  $\text{Pb}_{0.99}(\text{Zr}_{0.95}\text{Ti}_{0.05})_{0.98}\text{Nb}_{0.02}\text{O}_3$ : Microstructural effects. *Journal of Applied Physics*, 101(5):053525, 2007.
- [17] Chao-Nan Xu, Morito Akiyama, Kazuhiro Nonaka, and Tadahiko Watanabe. Electrical power generation characteristics of PZT piezoelectric ceramics. *Ultrasonics, Ferroelectrics, and Frequency Control, IEEE Transactions on*, 45(4):1065–1070, 1998.
- [18] Chok Keawboonchuay and Thomas G. Engel. Electrical power generation characteristics of piezoelectric generator under quasi-static and dynamic stress conditions. *Ultrasonics, Ferroelectrics, and Frequency Control, IEEE Transactions on*, 50(10):1377–1382, 2003.
- [19] Abhijit Pramanick, Anderson D. Prewitt, Jennifer S. Forrester, and Jacob L. Jones. Domains, domain walls and defects in perovskite ferroelectric oxides: A review of present understanding and recent contributions. *Critical Reviews in Solid State and Materials Sciences*, 37(4):243–275, 2012.
- [20] Attay Kovetz. *Electromagnetic theory*. Oxford University Press Oxford, 2000.
- [21] Stephen T. Montgomery and Patrick F. Chavez. Basic equations and solution method for the calculation of the transient electromechanical response of dielectric devices. *NASA STI/Recon Technical Report N*, 87:15436, 1986.
- [22] ALEGRA-EMMA webpage. <http://www.cs.sandia.gov/ALEGRA/Alegra.EMMA.html>. Updated: 2010-09-07.
- [23] Solomon Levinson. Multiple electrode series capacitor, December 6 1983. US Patent 4,419,713.
- [24] Manfred Kahn. Multilayer ceramic capacitors-materials and manufacture. *AVX Technical Information Series*, 1981.
- [25] Bill Sloka. Flex crack mitigation. 2008.
- [26] Paul A. Tipler. *Physics for Scientists and Engineers: Vol. 2: Electricity and Magnetism, Light*. W.H. Freeman/Worth New York, 1999.
- [27] Anthony J. Moulson and John M. Herbert. *Electroceramics: materials, properties, applications*. John Wiley & Sons, 2003.



- [28] Killian Driscoll. *Understanding quartz technology in early prehistoric Ireland*, volume 10889. Killian Driscoll, 2010.
- [29] Jacques Curie and Pierre Curie. Development by pressure of polar electricity in hemihedral crystals with inclined faces. *Bull. soc. min. de France*, 3:90, 1880.
- [30] Paul M. Moubarak, Pinhas Ben-Tzvi, and Mona Elwakkad Zaghloul. A self-calibrating mathematical model for the direct piezoelectric effect of a new MEMS tilt sensor. *Sensors Journal, IEEE*, 12(5):1033–1042, 2012.
- [31] Ling Dai, Fuchang Lin, Zhifang Zhu, and Jin Li. Analysis of ferroelectric characteristics and HV pulse experiments on X7R ceramic capacitors. In *Electrical Insulation and Dielectric Phenomena, 2004. CEIDP'04. 2004 Annual Report Conference on*, pages 97–100. IEEE, 2004.
- [32] Premi Chandra and Peter B. Littlewood. A Landau primer for ferroelectrics. In *Physics of Ferroelectrics*, pages 69–116. Springer, 2007.
- [33] Ulrich Böttger. Dielectric properties of polar oxides. *Polar oxides: properties, characterization and imaging*, 2005.
- [34] Malcolm E. Lines and Alastair M. Glass. *Principles and applications of ferroelectrics and related materials*. Oxford University Press, 1977.
- [35] Ying-Long Wang, Xing-Yuan Wang, Li-Zhi Chu, Ze-Chao Deng, Wei-Hua Liang, Bao-Ting Liu, Guang-Sheng Fu, N. Wongdamnern, T. Sareein, and R. Yimnirun. Simulation of hysteresis loops for polycrystalline ferroelectrics by an extensive Landau-type model. *Physics Letters A*, 373(46):4282–4286, 2009.
- [36] Dal-Hyun Do, Paul G. Evans, Eric D. Isaacs, Dong Min Kim, Chang Beom Eom, and Eric M. Dufresne. Structural visualization of polarization fatigue in epitaxial ferroelectric oxide devices. *Nature materials*, 3(6):365–369, 2004.
- [37] IPC/JEDEC Standard. IPC/JEDEC–9702. *Monotonic Bend Characterization of Board-Level Interconnects*, June 2004.
- [38] JEDEC Standard JESD22. B110b. *Mechanical Shock - Component and Subassembly*, July 2013.
- [39] Siva P.V. Nadimpalli and Jan K. Spelt. Prediction of pad cratering fracture at the copper pad–printed circuit board interface. *Microelectronics Reliability*, 52(7):1454–1463, 2012.
- [40] Jing-En Luan, Tong Yan Tee, Eric Pek, Chwee Teck Lim, Zhaowei Zhong, and Jiang Zhou. Advanced numerical and experimental techniques for analysis of dynamic responses and solder joint reliability during drop impact. *Components and Packaging Technologies, IEEE Transactions on*, 29(3):449–456, 2006.

- [41] Pradeep Lall, Ryan Lowe, and Kai Goebel. Prognostic health monitoring for a micro-coil spring interconnect subjected to drop impacts. In *Prognostics and Health Management (PHM), 2013 IEEE Conference on*, pages 1–11. IEEE, 2013.
- [42] Tong Yan Tee, Jing-en Luan, Eric Pek, Chwee Teck Lim, and Zhaowei Zhong. Novel numerical and experimental analysis of dynamic responses under board level drop test. In *Thermal and Mechanical Simulation and Experiments in Microelectronics and Microsystems, 2004. EuroSimE 2004. Proceedings of the 5th International Conference on*, pages 133–140. IEEE, 2004.
- [43] R.A. Amy, G.S. Aglietti, and Guy Richardson. Board-level vibration failure criteria for printed circuit assemblies: an experimental approach. *Electronics Packaging Manufacturing, IEEE Transactions on*, 33(4):303–311, 2010.
- [44] Hongtao Ma and Tae-Kyu Lee. Effects of board design variations on the reliability of lead-free solder joints. *Components, Packaging and Manufacturing Technology, IEEE Transactions on*, 3(1):71–78, 2013.
- [45] Akash Agrawal, Tim Levo, James Pitarresi, and Brian Roggeman. Board level energy correlation and interconnect reliability modeling under drop impact. In *Electronic Components and Technology Conference, 2009. ECTC 2009. 59th*, pages 1694–1702. IEEE, 2009.
- [46] Mohammadreza Keimasi, Michael H. Azarian, and Michael G. Pecht. Flex cracking of multilayer ceramic capacitors assembled with Pb-free and Tin–Lead solders. *Device and Materials Reliability, IEEE Transactions on*, 8(1):182–192, 2008.
- [47] John D. Prymak and Jim Bergenthal. Capacitance monitoring while flex testing. *Components, Packaging, and Manufacturing Technology, Part A, IEEE Transactions on*, 18(1):180–186, 1995.
- [48] Mollie C. Drumm. Computational simulation of explosively generated pulsed power devices. Technical report, DTIC Document, 2013.
- [49] J. Chen, Peter and T. Montgomery, Stephen. Boundary effects on the normal-mode responses of linear transversely isotropic piezoelectric materials. *Journal of applied physics*, 49(2):900–904, 1978.
- [50] William M. Scherzinger and Daniel C. Hammerand. Library of advanced materials for engineering–LAME. 2007.
- [51] John A. Mitchell and Tim J. Fuller. Nonlinear kinematics for piezoelectricity in ALEGRA-EMMA. 2013.
- [52] Rudolf Bechmann. Elastic, piezoelectric, and dielectric constants of polarized Barium Titanate ceramics and some applications of the piezoelectric equations. *The Journal of the Acoustical Society of America*, 28(3):347–350, 1956.

- [53] Ichiro Ueda and Seiji Ikegami. Piezoelectric properties of modified Pbtio, ceramics. *Piezoelectricity*, (5):175, 1992.
- [54] AVX surface mount ceramic capacitor products. <http://avx.com/docs/masterpubs/Surface%20Mount%2014.4.pdf>. Version 14.9.
- [55] High performance ISOLA 370HR data sheet. <http://www.isola-group.com/wp-content/uploads/2014/04/370HR-Laminate-and-Prepreg-Data-Sheet-Isola.pdf>. Updated: April 2014.
- [56] H. Jaffe, D. Berlincourt, T. Kinsley, T.M. Lambert, D. Schwartz, E.A. Gerber, and I.E. Fair. IRE standards on piezoelectric crystals: measurements of piezoelectric ceramics. *Proc. IRE*, 49:1161–1169, 1961.

| <b>REPORT DOCUMENTATION PAGE</b>  |                             |                                       |                                   |  | <i>Form Approved</i><br><b>OMB No. 0704-0188</b>   |  |
|---|-----------------------------|---------------------------------------|-----------------------------------|--|--|--|
| The public reporting burden for this collection of information is estimated to average 1 hour per response, including the time for reviewing instructions, searching existing data sources, gathering and maintaining the data needed, and completing and reviewing the collection of information. Send comments regarding this burden estimate or any other aspect of this collection of information, including suggestions for reducing this burden to Department of Defense, Washington Headquarters Services, Directorate for Information Operations and Reports (0704-0188), 1215 Jefferson Davis Highway, Suite 1204, Arlington, VA 22202-4302. Respondents should be aware that notwithstanding any other provision of law, no person shall be subject to any penalty for failing to comply with a collection of information if it does not display a currently valid OMB control number. <b>PLEASE DO NOT RETURN YOUR FORM TO THE ABOVE ADDRESS.</b>  |                             |                                       |                                   |  |  |  |
| <b>1. REPORT DATE</b> (DD-MM-YYYY)<br>17-09-2015  |                             | <b>2. REPORT TYPE</b><br>Dissertation |                                   | <b>3. DATES COVERED</b> (From — To)<br>Oct 2012-Sep 2015   |  |  |
| <b>4. TITLE AND SUBTITLE</b><br><br>Piezoelectric Response of Ferroelectric Ceramics<br>Under Mechanical Stress   |                             |                                       |                                   | <b>5a. CONTRACT NUMBER</b><br><br><b>5b. GRANT NUMBER</b><br><br><b>5c. PROGRAM ELEMENT NUMBER</b> |  |  |
| <b>6. AUTHOR(S)</b><br><br>Kaplan, Sergey M., Major, USAF   |                             |                                       |                                   | <b>5d. PROJECT NUMBER</b><br><br><b>5e. TASK NUMBER</b><br><br><b>5f. WORK UNIT NUMBER</b>         |  |  |
| <b>7. PERFORMING ORGANIZATION NAME(S) AND ADDRESS(ES)</b><br>Air Force Institute of Technology<br>Graduate School of Engineering and Management (AFIT/EN)<br>2950 Hobson Way<br>Wright-Patterson AFB, OH 45433-7765   |                             |                                       |                                   | <b>8. PERFORMING ORGANIZATION REPORT NUMBER</b><br><br>AFIT-ENY-DS-15-S-064                        |  |  |
| <b>9. SPONSORING / MONITORING AGENCY NAME(S) AND ADDRESS(ES)</b><br>Air Force Research Laboratory, Munitions Directorate, Fuzes Branch<br>Dr. Jason R. Foley<br>306 W. Eglin Blvd., Bldg 432<br>Eglin AFB, FL 32542-5430<br>(850) 883-0584; jason.foley.1@us.af.mil   |                             |                                       |                                   | <b>10. SPONSOR/MONITOR'S ACRONYM(S)</b><br><br>AFRL/RWMF   |  |  |
|   |                             |                                       |                                   | <b>11. SPONSOR/MONITOR'S REPORT NUMBER(S)</b>  |  |  |
| <b>12. DISTRIBUTION / AVAILABILITY STATEMENT</b><br>Distribution Statement A:<br>Approved for Public Release; Distribution Unlimited  |                             |                                       |                                   |  |  |  |
| <b>13. SUPPLEMENTARY NOTES</b><br>This work is declared a work of the U.S. Government and is not subject to copyright protection in the United States.  |                             |                                       |                                   |  |  |  |
| <b>14. ABSTRACT</b><br>Manufacturers are constantly developing increasingly miniature, ferroelectric multi-layer ceramic capacitors, survivable under progressively harsher mechanical stresses. However, the piezoelectric response of the bulk Barium Titanate-based dielectric in such capacitors has not yet been addressed for shocks above 3,000 g. Thus, the current research developed a finite element capacitor model and modified an established constitutive relationship to calculate the capacitive response under high-g drop impact. Scanning electron microscope and impedance analyzer data confirmed the flexural mode of mechanical failure, while the newly applied RC capacitance measurement technique detected discreet partial and complete electrode separation from the terminal, corresponding to the board oscillation frequency. The experiments detected an up to 10% increase in capacitance during 24,000 g shocks, while the numerical model predicted the electromechanical response to within 2% of the nominal capacitance value, closely matching in waveform to the experimental data. When the flexural failures were completely prevented and the capacitance response was reduced by 81% with completely restricted board flexure, the electromechanical response was still detectable during drop impacts generating 3,000 g peak accelerations. While preventing board oscillations may reduce mechanical failure probability, unaddressed piezoelectric response of ferroelectric capacitors may still cause significant intermittent reliability issues above commercially relevant conditions. |                             |                                       |                                   |  |  |  |
| <b>15. SUBJECT TERMS</b><br>ferroelectric, high-g, impact, capacitance, electromechanical   |                             |                                       |                                   |  |  |  |
| <b>16. SECURITY CLASSIFICATION OF:</b>  |                             |                                       | <b>17. LIMITATION OF ABSTRACT</b> |  | <b>18. NUMBER OF PAGES</b><br><br>180  |  |
| <b>a. REPORT</b><br><br>U   | <b>b. ABSTRACT</b><br><br>U | <b>c. THIS PAGE</b><br><br>U          | UU                                |  | <b>19a. NAME OF RESPONSIBLE PERSON</b><br>Dr. Robert B. Greendyke (ENY)                          |  |
|   |                             |                                       |                                   |  | <b>19b. TELEPHONE NUMBER</b> (include area code)<br>(937)255-3636x4567 Robert.Greendyke@afit.edu |  |